Formation of Compact Stellar Clusters by High-Redshift Galaxy Outflows

by

William James Gray

A Dissertation Presented in Partial Fulfillment
of the Requirements for the Degree
Doctor of Philosophy

Approved April 2012 by the
Graduate Supervisory Committee:

Evan Scannapieco, Chair
Sumner Starrfield
Patrick Young
Rogier Windhorst
Francis Timmes

ARIZONA STATE UNIVERSITY

May 2012

ABSTRACT

Using high-resolution three-dimensional adaptive mesh refinement simulations I study the interaction between primordial minihalo, a clump of baryonic and dark matter with a virial temperature below the atomic cooling limit, and a galaxy outflow. In Chapter 2 I concentrate on the formation of molecular coolants and their effect on the evolution of the minihalo gas. Molecular coolants are important since they allow gas to cool below 10^4 K. Therefore, I implement a primordial chemistry and cooling network that tracks the evolution and cooling from these species. I show that the shock from the galaxy outflow produces an abundance of coolants in the primordial gas which allows the gas to cool to below 10^4 K. I also show that this interaction produces compact stellar clusters that are ejected from their parent dark matter halos.

In Chapter 3 I look at the turbulent mixing of metals that occur between the minihalo and outflow. To do this, I develop a sub-grid model for turbulence that reproduces three primary fluid instabilities. I find that the metals from the outflow are well mixed throughout the minihalo gas. In addition, the metal abundance found roughly corresponds to the observed abundances in halo globular clusters.

In Chapter 4, I conduct a suite of simulations that follow this interaction over a wide range of parameters. In almost all cases, the shocked minihalos form molecules and cool rapidly to become compact, chemically homogenous stellar clusters. Furthermore, I show that the unique properties of these clusters make them a prime observational target for study with the next generation of telescopes.

Given the unique properties of these clusters there are reasons to suspect that their low-redshift counterparts are halo globular clusters. I outline this comparison in Chapter 5 and give my conclusions in Chapter 6.

Finally, I summarize my current work in Chapter 7 and future extensions in Chapter 8.

By the end, I hope to convince you that the interaction between a galaxy outflow and a primordial minihalo provides a formation pathway for present day halo globular clusters.

DEDICATION

This Dissertation is dedicated to my wife, Carly, for her constant love and support while I completed my graduate work.

ACKNOWLEDGEMENTS

There are several people that should be acknowledged for their help, support, and assistance throughout my time at Arizona State University and as a part of the School of Earth and Space Exploration (SESE).

First of all, I would like to express my gratitude to my advisor, Dr. Evan Scannapieco for his guidance, patience, and financial support throughout this process. To Dr. Frank Timmes for much appreciated discussions on nuclear/chemical networks and associated linear algebra solvers. I would like to thank the faculty on both my comprehensive exam and dissertation committees, Dr. Allen McNamara, Dr. Evan Scannapieco, Dr. Sumner Starrfield, Dr. Frank Timmes, Dr. Rogier Windhorst, and Dr. Patrick Young. In addition, I would like to thank other SESE staff members who have helped me through the years, Dr. Rolf Jensen, Dr. Paul Scowen, Dr. Themis Athanassiadou, Dr. Melissa Morris, and former SESE executive assistant Del Schrag. Finally, I would like to thank Scott Smas for all his help in coordinating with Dr. Rogier Windhorst on my letters of recommendation and scheduling meetings.

I would also like to acknowledge other SESE and Physics graduate students for their support and friendship. Those who I have taken classes with and worked closely with: Simon Porter, Micheal Rutkowski, Michael Pagano, Emily McLinden, Jon Oiler, Nahks Tr'Ehnl, Teresa Ashcraft, Angel Fuentes, Brian Gleim, Wendy Hawley, Michael Lesniak III, Kaz Tamura, Carola Ellinger, Hwiyun Kim, and Katie Kaleida. In particular, I would like to thank my office mates, Dr. Cody Raskin and Mark Richardson.

The simulations performed as part of this dissertation executed using the Saguaro supercomputer which is a part of the ASU Advanced Computing Center. Without this resource, much of the work presented here would not have been done in such a timely manner. In particular, I want to thank the director

of the high performance computing center, Dr. Frank Timmes.

Finally, I acknowledge all the love and support I have received from my family. In particular, my parents, Dr. Lawrence and Margaret Gray, my brother and sister-in-law, future-Drs. Lawrence and Karina Gray, my sister and brother-in-law, Stephanie and Nick Stark, and my In-laws, Gus and Peggy Mohr. I owe a debt of gratitude to my extended family that live in Arizona that made the initial transition to Tempe easier, Uncle Bill and Aunt Phyliss Dodds, Uncle Bob and Aunt Muriel Kremb, Uncle Mike and Aunt Mary Palmer, and my maternal Grandparents Robert and Hildreth Dodds. I would also like to acknowledge my paternal grandparents who passed away during my time in graduate school, my Grandmother Virgina Gray who passed away September 24th, 2007 and my Grandfather Lawrence Gray who passed away November 9th, 2010.

Finally, I owe a large debt of gratitude to my wife Carly for her love and support while I pursue my degree.

TABLE OF CONTENTS

LIST OF TABLES

LIST OF FIGURES

Chapter 1

Introduction

A generic prediction of the cold dark matter model of cosmology is a large high-redshift population of gravitationally-bound clouds that are unable to form stars. Because atomic H and He line cooling is only effective at temperatures above 10^4 K, clouds of gas and dark matter with virial temperatures below this threshold must radiate energy through dust and molecular line emission. While the levels of H_2 left over from recombination are sufficient to cool gas in the earliest structures (*e.g.* Abel *et al.* 2002; Bromm *et al.* 2002), the resulting 11.20 - 13.6 eV background emission from the stars in these objects (*e.g.* Haiman *et al.* 1997; Ciardi *et al.* 2000; Sokasian *et al.* 2004; O'Shea & Norman 2007) is likely to have quickly dissociated these trace levels of primordial molecules (Galli & Palla 1998). And although an early X-ray background could have provided enough free electrons to promote H_2 formation, the relative strength between these two backgrounds is uncertain, and it is unlikely that the background was strong enough to balance ultraviolet (UV) photodissociation. Even if there were some trace amount of H_2 in these clouds, it is likely to be in such a small abundance as to not impact their structure (Whalen *et al.* 2008a; Ahn *et al.* 2009). At such high-redshifts, cooling is restricted to atomic hydrogen line cooling and, if the gas is highly ionized, bremsstrahlung radiation. However, at temperature below 10^4 K, neither is efficient since the gas is both neutral and atomic.

This creates a large population of low mass halos in the early universe with very interesting properties. First, they are composed of only elements formed during the Big Bang, which corresponds to 76% hydrogen, 24% helium, 0.01% deuterium, and trace amounts of lithium and beryllium by mass. Secondly, inefficient cooling sets an upper limit to the mass of each halo. The

10^4 K virial temperature roughly corresponds to the upper mass limits between 10^4 and $10^{7.5}$ $M_\odot$. These minihalos remain largely sterile until acted upon by some outside influence so as to catalyze coolant formation. There are two such possible mechanisms, ionization fronts and shock fronts.

In the case of ionization fronts, such as would occur during the epoch of reionization, high-energy photons emitted from galaxies or quasars interact with the neutral atomic minihalo gas. Bond, Szalay & Silk (1988) originally discussed how the resulting photoionization would expel the gas contained in a minihalo by suddenly heating it to $T \approx 10^4$ K, as would be the case in the optically-thin limit. On the other hand, Cen (2001), used simple analytic estimates to argue that ionization fronts would cause non-equilibrium H_2 formation and the collapse of the gas inside the gravitational potential. However, Barkana & Loeb (1999) studied minihalo evaporation using static models of uniformly illuminated spherical clouds, accounting for optical depth and self-shielding effects, and showed that the cosmic UV background boiled most of the gas out of these objects. Later, Haiman, Abel, & Madau (2001) carried out three-dimensional (3D) hydrodynamic simulations assuming the minihalo gas was spontaneously heated to 10^4 K, also finding quick disruption. Finally, full radiation-hydrodynamical simulations of ionization front-minihalo interactions were carried out in Iliev *et al.* (2005) and Shapiro *et al.* (2004; see also Shapiro, Raga & Mellema 1997; 1998). These demonstrated that intergalactic ionization fronts decelerated when they encountered the dense, neutral gas inside minihaloes and were thereby transformed into D-type fronts, preceded by shocks that completely photoevaporated the minihalo gas.

A second and more promising avenue for coolant formation is the interaction between galactic outflows and minihaloes. These galaxy-scale winds,

which are driven by core-collapse supernova and winds from massive stars, are commonly observed around dwarf and massive starbursting galaxies at both low and high redshifts (*e.g.* Lehnert & Heckman 1996; Franx *et al.* 1997; Pettini *et al.* 1998; Martin 1999; 1998; Heckman *et al.* 2000; Veilleux *et al.* 2005; Rupke *et al.* 2005), and a variety of theoretical arguments suggest that these galaxies represent only the tail end of a larger population of smaller "pre-galactic", starbursts that formed before reionization (Scannapieco, Ferrara & Madau 2002; Thacker, Scannapieco, & Davis 2002).

Furthermore, the interstellar gas swept up in a starburst-driven wind can effectively trap the ionizing photons behind it (Fujita *et al.* 2003), meaning that at high redshifts, many intergalactic regions may have been impacted by outflows well before they were ionized. With the technological advancement of telescopes and spectrographs even earlier redshifts can be studied. Recent spectroscopic observations of a $z \approx 6$ quasi stellar object (QSO) show the presence of strongly ionized carbon originating from a $z \sim 5.7$ Lyman-α emitter (Diaz *et al.* 2011). Such $\approx 100 - 300$ km/s shocks can cause intense cooling through two mechanisms: (i) the mixing of metals with ionization potentials below 13.6 eV (Dalgarno & McCray 1972), which allow for atomic line cooling even at temperatures below 10^4 K; and (ii) the formation of H_2 and HD by nonequilibrium processes (Mac Low & Shull 1986; Shapiro & Kang 1987; Kang *et al.* 1990; Ferrara 1998; Uehara & Inutsuka 2000), which allow for molecular line cooling associated vibrational and rotational transitions (Palla & Zinnecker 1988). In fact, Scannapieco *et al.* (2004) showed that these effects were so large that shock interactions could induce intense bursts of cooling and collapse in previously "sterile" minihalo gas. Using simple analytic models, they found that the most likely result was the formation of compact clusters of coeval stars,

although they also emphasized the importance of multidimensional numerical studies to confirm this result.

With the inclusion of metals into the outflow gas, the mixing between the outflow and the primordial minihalo gas becomes important. In addition to creating an additional cooling pathway, it helps constrain the chemical makeup in the final stellar clumps. To study this properly, a sub-grid model for turbulence is required to track the mixing between these two fluid reservoirs.

Turbulent processes are instrumental in understanding a wide range of astrophysical observations, including the elemental homogeneity in field stars (Reddy *et al.* 2003), open clusters (e.g., Friel & Boesgaard 1992; Twarog *et al.* 1997; Carraro *et al.* 1998), the Magellanic clouds (Olszewsit *et al.* 1991), dwarf-irregular galaxies (Thuan *et al.* 1995), and galactic and disk H II regions (e.g., Deharveng *et al.* 2000, Henry & Worthey 1999). Turbulent mixing is also important for the enrichment of primordial gas (Pan *et al.* 2007) and the transition from Population III to Population II stars (Scannapieco *et al.* 2003).

Similarly, turbulence affects the distribution and formation of molecular species. Because most chemical reactions are strongly temperature-dependent, by simply moving material to a region with different physical properties such as density, temperature, and UV flux, or by creating a local heating event through turbulent dissipation, many reactions can be greatly enhanced, which alters the final abundance of each species (for a review see Scalo & Elmegreen 2004). This can be particularly important in primordial gas at high-redshift, whose cooling properties are highly dependent on the mass fraction of molecular hydrogen and hydrogen deuteride. Furthermore, turbulent transport is equally important after reactions occur, as it will alter the physical distribution of the newly formed chemical species (e.g, Xie *et al.* 1995).

The outcome of these galaxy outflow minihalo interactions show much promise of transforming the static minihalos into dense, compact objects that are optimal for forming stars. Since these interactions occur at early in cosmological time, only the oldest and long lived stars would survive to now. The population of halo globular clusters that exist may be the observable consequence of these interactions.

Globular clusters are among the oldest stellar complexes in the Universe and their formation remains an open question. A typical globular cluster has an age between 10 - 13 Gyrs (Krauss & Chaboyer 2003), which demands a cosmological origin to their formation. These objects house, on average, between 10^{5-6} stars. Observations of galactic globular clusters systems show a bimodal color distribution, which suggests two distinct stellar populations. The 'metal-poor' population has a characteristic metallicity of $[Fe/H] \approx -1.6$ and is associated with the halo of the Milky way and the 'metal-rich' population has a metallicity of $[Fe/H] \approx -0.5$ and is associated with the thick disk or bulge of galaxies. These disk globular clusters are thought to form during the build up of the parent galaxy.

Recent studies suggest an additional population characterized as younger halo globular clusters. These clusters exhibit comparatively red horizontal branch (HB) morphology for a given metallicity, as compared to the blue HB morphology of halo globular clusters. The distribution of positions among these young halo clusters forms a plane that aligns with the plane formed by satellite galaxies, which suggests they share a common origin. This suggests that this population comes from accretion through large scale filaments (Keller *et al.* 2011).

However, while disk and young halo globular clusters have plausible formation mechanisms, the older halo globular clusters do not. It is these mysterious clusters that I will now focus on.

There are several important properties of halo globular clusters that must be accounted for in any theory of their formation. The mass distribution of clusters is well described by a Gaussian with a mean of 10^5 $M_\odot$and a dispersion of 0.5 dex (*e.g.* Armandroff 1989). Several dynamical destruction mechanisms are responsible for the distribution of observed globular clusters. First, two-body interactions act to exchange energy between stars in the cluster. This develops a Maxwellian velocity distribution among the stars and allows those at the high energy tail to escape. The more compact the cluster, the stronger the two body reactions and the more stars are ejected. Second, the stars in the cluster gain energy as the cluster passes through the disk of the parent galaxy, decreasing the binding energy of the cluster. Over time this will completely unbind the cluster. These two processes set the minimum (relaxation) and maximum (disk shocking) cluster radius for a given cluster mass. Finally, dynamical friction between the cluster and the parent galaxy causes the largest clusters to fall into the galaxy and break up.

Schematically this is shown in Fig. 1.1, which is reproduced from Gnedin *et al.* (1997). Here the authors have plotted the classical survival triangle of globular clusters for a variety of galactocentric radii where each boundary is formed by one of the above destruction mechanisms. Each triangle represents the expected survival volume over a Hubble time. While most of the observed globular clusters fall within the survival triangles, it is interesting to note the distinct lack of globular clusters with masses greater than $\sim 10^6$ $M_\odot$. So, while dynamical friction sets the maximum theoretical mass for the globular cluster

population, something intrinsic to the initial population of pre-GC objects sets the observed maximum mass. Tantalizingly, primordial minihalos provide a natural explanation for this mass limit.

The metallicity of halo globular clusters also provides a formation constraint. The metallicity distribution of a globular cluster population is well described by a Gaussian with a mean value of $[Fe/H] \sim$ -1.6 with a dispersion of 0.3 dex (Zinn 1985; Ashmax & Bird 1993). However, the dispersion within a given cluster is much more uniform with an average dispersion of only 0.1 dex. This suggests that the gas the cluster formed from was well mixed before the stars formed.

Finally, observations of globular clusters show that at least some do not reside within dark matter halos. This provides one of the strongest constraints on their formation. These observations show that tidal forces by the parent galaxy strip off more stars than would be expected if these clusters resided with dark matter (Irwin & Hatzidimitriow 1993; Grillmair *et al.* 1995; Conroy *et al.* 2011).

Taken together, the early universe contains all the ingredients for forming high-redshift stellar clusters that maybe the evolutionary precursors to the present-day population of halo globular clusters. Therefore, the questions to be answered is what is the outcome in the interaction between a galaxy outflow and primordial minihalo and can they be related to halo globular clusters.

The quest to answer this question is split up into three primary objectives. In Chapter 2 we introduce our initial minihalo model, the galaxy outflow/shock model, and the chemistry/cooling network. In particular, we study the formation and evolution of H_2 and HD, the two primary molecular coolants in primordial gas. We present the initial results of the interaction using

a fiducial model and determine the effect a dissociating UV background has on the final outcome. In Chapter 3 we implement a sub-grid turbulence model which tracks the mixing of metals from the outflow into the minihalo gas. In addition, we update our cooling functions to include metal-lines. Again, using our fiducial model, we present results comparing the differences with and without turbulent mixing and comparing the final state of the minihalo. In Chapter 4 we study how robust our formation model is by performing a parameter study. We also turn our attention to whether or not this interaction is observable with current and near-future telescopes. In Chapter 5 we compare the properties of our simulated stellar clusters to present day halo globular clusters. In Chapter 6 we reiterate our conclusions. Chapter 7 and 8 are dedicated to other work we have done as well as future prospects.

All simulations were performed with FLASH version 3.1, a multidimensional adaptive mesh refinement hydrodynamics code (Fryxell *et al.* 2000) that solves the Riemann problem on a Cartesian grid using a directionally-split Piecewise-Parabolic Method (PPM) solver (Colella & Woodward 1984; Colella & Glaz 1985; Fryxell, Müller, & Arnett 1989). Furthermore, unlike earlier versions of the code, FLASH3 includes an effective parallel multigrid gravity solver as described in Ricker (2008). When applicable, a description of new physics modules will be presented along with applicable tests.

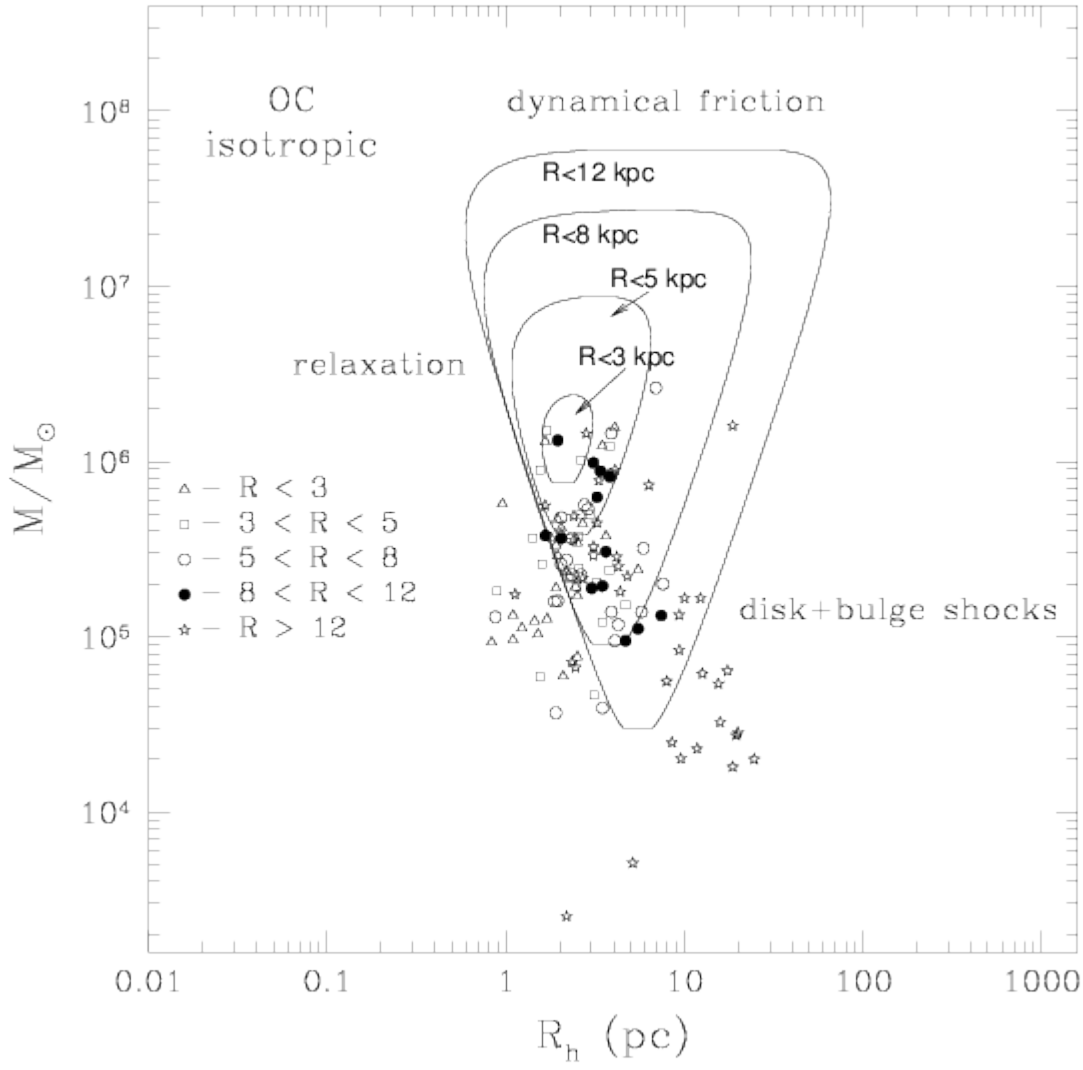

Figure 1.1: Theoretical survival triangles for globular clusters. Each leg of the triangle is set by a the destruction mechanisms, as labeled. The x-axis is the half mass radius in units of parsecs of a cluster and the y-axis is the cluster mass in units of solar masses. Observations are shown as points, where each shape differentiates between the galactocentric radius of each cluster. It is important to note that dynamical friction sets the theoretical upper mass limit, but no globular clusters are found with such high masses.

Chapter 2

Effect of Non-Equilibrium Chemistry

The first objective in this study is to look at the impact molecular formation and cooling has on the interaction between the primordial minihalo and galaxy outflow. To do this properly, two capabilities need to be added to FLASH: nonequilibrium primordial chemistry, and cooling from atoms and from molecules produced in these interactions. In this section we describe our numerical implementation of each of these processes, along with the tests we carried out before applying the code to shock-minihalo interactions.

Chemistry

As the minihalos we are considering in this paper are made up of primordial gas, their chemical makeup is highly restricted, with contributions from only hydrogen, helium, and low levels of deuterium. Yet even these three isotopes can exist in a variety of ionization states and molecules and are thus associated with a substantial network of chemical reactions that must be tracked throughout our simulations.

Implementation

The chemical network that was implemented into FLASH is outlined by Glover & Abel (2008, hereafter GA08). Throughout our simulations we track three states of atomic hydrogen (H, H^+, & H^-) and atomic deuterium (D, D^+, & D^-), three states of atomic helium (He, He^+, &, He^{++}), two states of molecular hydrogen (H_2 & H_2^+) and molecular hydrogen deuteride (HD & HD^+), and electrons (e^-). For simplification, any reaction that involved molecular deuterium (D_2) and all three-body reactions were neglected. As stated in GA08, the very small amount of D_2 and D_2^+ produced makes any cooling by these

molecules irrelevant, while three-body reactions only become important at $n \gtrsim 10^8$ cm^{-3} (*e.g.* Palla *et al.* 1983), many orders of magnitude denser than the conditions considered here. With these constraints, a total of 84 reactions were used out of the 115 described in GA08.

Photodissociation rates due to an external radiation field were also included as given in Glover & Savin (2009). These rates are calculated assuming a $T_{\rm eff} = 10^5$ K blackbody source and their strength is quantified by the flux at the Lyman limit, $J(\nu_\alpha) = 10^{-21} J_{21}$ erg s^{-1} cm^{-2} Hz^{-1} sr^{-1}. Note that once H_2 and HD are produced in sufficient quantities, some molecules are self-shielded from the background radiation. However, for simplicity, I consider only the case where there was no self-shielding, and thus our results place an upper limit on the effect of a dissociating background. This process adds an additional 7 reactions for a total of 91 reactions in the chemical network.

In reactions that involve free electrons recombining with ions, there are two possible choices for the reaction rate, depending on the overall optical depth of the cloud to ionizing radiation. In the optically-thin case (Case A; Osterbrock 1989) ionizing photons emitted during recombination are lost to the system, while in the optically-thick case (Case B), ionizing photons are reabsorbed by neighboring neutral atoms, which have the effect of lowering the recombination rates by essentially not allowing recombination to the ground state. There are three reactions ($H^+ + e^- \rightarrow H + \gamma$, $He^+ + e^- \rightarrow He + \gamma$, and $He^{++} + e^- \rightarrow He^+ + \gamma$) where this is a concern, and as I shall show below, in all cases our clouds are optically thick, such that Case B recombination rates are appropriate.

The binding energy from each species is also important in the total energy budget and on the evolution of the gas. In FLASH these are defined such

that all of the neutral species (H, D, e^-, & H) have binding energies equal to zero. As the gas is heated and the atomic species begin to ionize, the endothermic reactions remove the binding energy between the nucleus and electron(s) from the internal energy of the gas. For H and D this requires 13.6 eV, while the ionized states for Helium (He^+ and He^{++}) have ionization potentials of 24.5 eV and 79.0 eV respectively. H^- and D^- are only weakly bound and have similar binding energies of 0.75 eV. Finally H_2 and HD have binding energies of 4.4 eV, and H_2^+ and HD^+ have binding energies of 10.9 eV, somewhat lower than the atomic species.

To describe the evolution of our 14 species, we enumerate them with an index i such that each has Z_i protons and A_i nucleons, following the structure and syntax from Timmes (1999). Next we consider a gas with a total mass density ρ and temperature T and denote the number and mass densities of the ith isotope as n_i and ρ_i, respectively. For each species we also define a mass fraction

$$X_i \equiv \rho_i/\rho = n_i A_i/(\rho N_A), \tag{2.1}$$

where N_A is Avogadro's number, and I define the molar abundance of the ith species as

$$Y_i \equiv X_i/A_i = n_i/(\rho N_A), \tag{2.2}$$

where conservation of mass is given by $\sum_i^N X_i = 1$. Each of the 14 species can then be cast as a continuity equation in the form

$$\dot{Y}_i \equiv \frac{dY_i}{dt} = \dot{R}_i, \tag{2.3}$$

where $\dot{R}_i$ is the total reaction rate due to all the binary reactions of the form $i + j \rightarrow k + l$, defined as

$$\dot{R}_i \equiv \sum_{j,k} Y_l Y_k \lambda_{kj}(l) - Y_i Y_j \lambda_{jk}(i), \tag{2.4}$$

where λ_{kj} and λ_{jk} are the creation and destruction chemical reaction rates for a given species. If the species in question is affected by UV background radiation, the continuity equation takes the following form,

$$\dot{R}_i \equiv \sum_{j,k} Y_l Y_k \lambda_{kj}(l) - Y_i Y_j \lambda_{jk}(i) - Y_i J(\nu_\alpha), \tag{2.5}$$

where the last term accounts for the amount of these species that are destroyed by the background radiation, J(ν_α). Throughout our simulations, changes in the number of free elections are not calculated directly, but rather at the end of each cycle I use charge conservation to calculate their molar fraction, as

$$Y_{elec} = Y_{\mathrm{H^+}} + Y_{\mathrm{D^+}} + Y_{\mathrm{HD^+}} + Y_{\mathrm{H_2^+}} + Y_{\mathrm{He^+}} + 2Y_{\mathrm{He^{++}}} - Y_{\mathrm{H^-}} - Y_{\mathrm{D^-}}. \tag{2.6}$$

Because of the often complex ways that the chemical reaction rates depend on temperature and the intrinsic order of magnitude spread in the rates, the resulting equations are 'stiff,' meaning that the ratio of the minimum and maximum eigenvalue of the Jacobian matrix, $J_{i,j} = \partial \dot{Y}_i / \partial Y_j$, is large and imaginary. This means that implicit or semi-implicit methods are necessary to efficiently follow their evolution. To address this problem, we arrange the molar fractions of the 13 species, excluding $\mathrm{e^-}$, into a vector $\mathbf{Y}$, and solve the resulting system of equations using a 4^{th} order accurate Kaps-Rentrop, or Rosenbrock method (Kaps & Rentrop 1979). In this method, the network is advanced over a time step h via

$$\mathbf{Y}^{n+1} = \mathbf{Y}^n + \sum_{i=1}^{4} b_i \mathbf{\Delta}_i, \tag{2.7}$$

where the $\mathbf{\Delta_i}$ vectors are found by successively solving the four matrix equations

$$(\hat{1}/\gamma h - \bar{J}) \cdot \mathbf{\Delta}_1 = f(\mathbf{Y}^n), \tag{2.8}$$

$$(\hat{1}/\gamma h - \bar{J}) \cdot \mathbf{\Delta}_2 = f(\mathbf{Y}^n + a_{21}\mathbf{\Delta}_1) + c_{21}\mathbf{\Delta}_1/h, \tag{2.9}$$

$$(\hat{1}/\gamma h - \bar{J}) \cdot \mathbf{\Delta}_3 = f(\mathbf{Y}^n + a_{31}\mathbf{\Delta}_1 + a_{32}\mathbf{\Delta}_2) + (c_{31}\mathbf{\Delta}_1 + c_{32}\mathbf{\Delta}_2)/h, \qquad \text{and} \tag{2.10}$$

$$(\hat{1}/\gamma h - \bar{J}) \cdot \mathbf{\Delta}_4 = f(\mathbf{Y}^n + a_{41}\mathbf{\Delta}_1 + a_{42}\mathbf{\Delta}_2 + a_{43}\mathbf{\Delta}_3) + (c_{41}\mathbf{\Delta}_1 + c_{42}\mathbf{\Delta}_2 + c_{43}\mathbf{\Delta}_3)/h. \tag{2.11}$$

Here b_i, γ, a_{ij}, and c_{ij} are fixed constants of the method, $f(\mathbf{Y}) \equiv \dot{\mathbf{Y}}$, $\hat{1}$ is the identity matrix, and $\bar{J}$ is the Jacobian matrix. Note that the four matrix equations represent a staged set of linear equations and that the four right hand sides are not known in advance. At each step, an error estimate is given for the difference between the third and fourth order solutions. For comparison we also carry out tests, using a multi-order Bader-Deuflhard method (Bader & Deuflhard 1983). However in the end, the Rosenbrock method was chosen over this method because of its efficiency and speed.

As the species evolve, the temperature of the gas changes from the release of internal energy from recombinations or the loss of internal energy from ionizations and dissociations. These changes can in turn affect the reaction rates. Thus to ensure the stability of the chemistry routine while at the same time allowing the simulation to proceed at the hydrodynamic time-step, I developed a method of cycling over multiple Kaps-Rentrop time steps within a single hydrodynamic time step. Here I estimate an initial chemical time step of each species as

$$\tau_{\mathrm{chem},i} = \alpha_{\mathrm{chem}} \frac{Y_i + 0.1Y_{H^+}}{\dot{Y}_i}, \tag{2.12}$$

where α_{chem} is a constant determined at runtime that controls the desired fractional change of the fastest evolving species. The change in molar

abundances, $\dot{Y}_i$'s, were calculated from the ordinary differential equations that make up the chemical network, and the molar fractions of each species Y_i's are given by the current values. In both the tests and simulations, we chose a value of $\alpha_{\rm chem} = 0.5$.

Note that we offset the subcycling time step by adding a small fraction of the ionized hydrogen abundance to eq. (2.12). This is because there are conditions where a species is very low in abundance but changing very quickly, for example, rapid ionization of atomic species, which will cause the subcycling to run away with extremely small time steps. In regions in which most species are neutral, this has little effect since the chemical time step is likely longer than the hydrodynamical one, and in regions in which abundances are rapidly changing, then this extra term buffers against very small times steps. It also prevents rapid changes in internal energy as energy is removed as atomic species are ionized and gained as they recombine.

Once calculated, these species time steps are compared to each other and the smallest time step, associated with the fastest evolving species, is chosen as the subcycle time step. If this is longer than the hydrodynamic time step, the hydrodynamic time step is used instead and no additional subcycling is done. If subcycling is required, the species time step is subtracted from the total hydrodynamic time step and the network is then updated over the chemical time step. The species time steps are recalculated after each subcycle and compared to the remaining hydrodynamic time step. This is repeated until a full hydrodynamic time step is completed, as is schematically shown in Fig. 2.1.

In cases in which the gas is extremely hot or cold, the chemical make-up can be determined directly from the temperature, avoiding the need for matrix inversions. If the temperature is above 10^5 K then all atomic species become

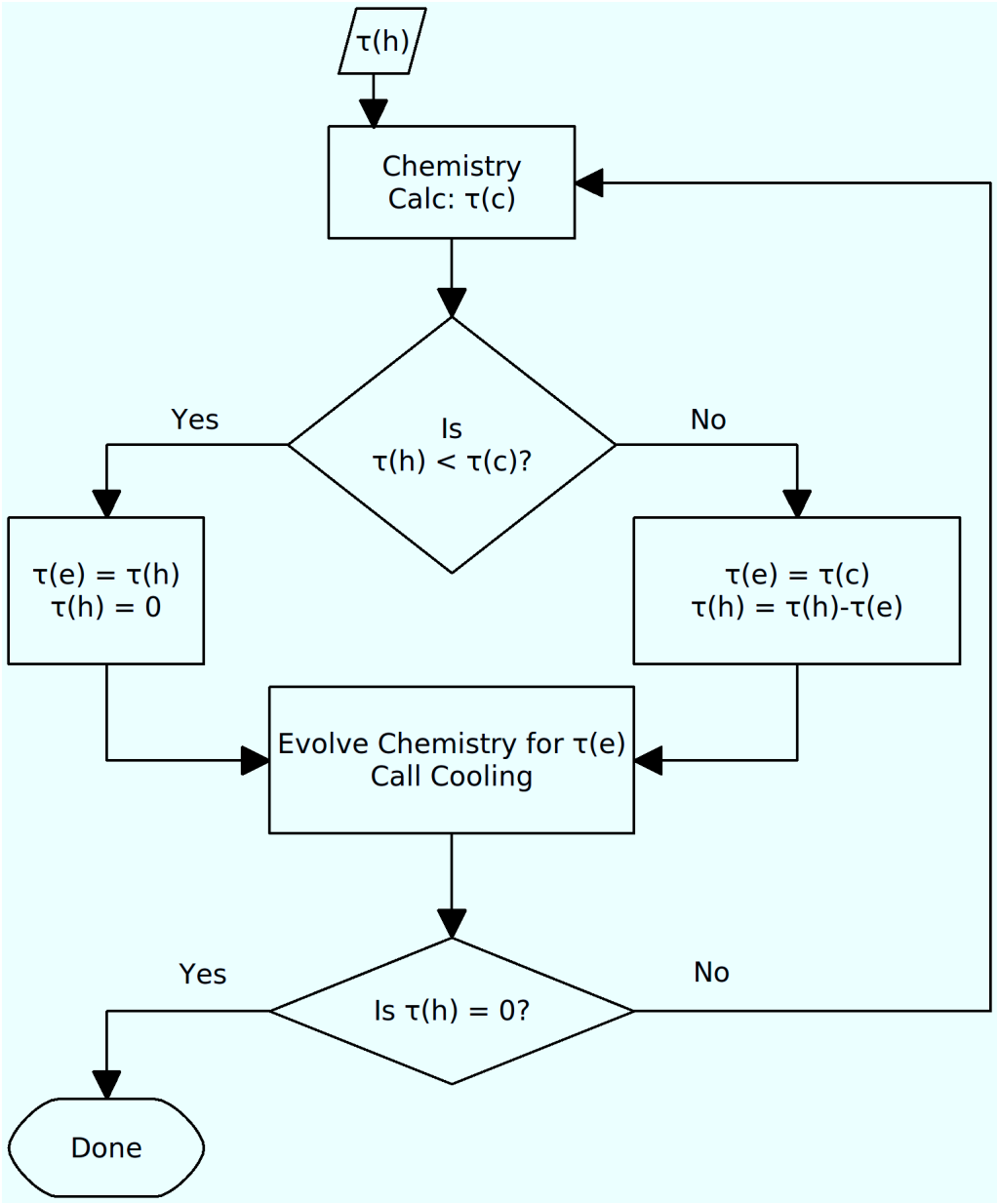

Figure 2.1: Schematic view of chemistry subcycling. First, the chemical time step, $\tau(c)$, is calculated using eqn. (2.12). If this is larger than the hydrodynamic time step, then the evolution time step, $\tau(e)$, is set to the hydrodynamic time step. Else, $\tau(e)$ is set to the chemical time step. The network is then evolved for $\tau(e)$ and the remaining time step $\tau(h)$ is calculated. If this is zero then we proceed to the next step, else we cycle back through the network with the updated abundances. This loop continues until the full hydrodynamic time step is covered. Note that after every chemical network iteration, the cooling routine is called.

ionized and all molecular species are dissociated, and the network can be bypassed. If the temperature is between 2.0×10^4 and 1.0×10^5 K , then we 'prime' the solutions and ionize 5% of available neutral hydrogen, 5% of neutral helium (4.5% into singly ionized helium and 0.5% into doubly ionized helium), before entering the iterative solver, to help accelerate the routine towards the correct solution. Finally if the temperature is less than 50 K, then all species are kept the same, and no reactions are calculated. This is done because cooling and chemistry rates become unimportant at such low temperatures. It also has the benefit of speeding up the simulation slightly as very little time is spent in either the cooling or chemistry routines. In all other cases, the full network is evolved without alterations.

Chemistry Tests

To test our implemented chemical network, we carry out a series of runs in which initially dissociated and ionized gas was held at constant temperature and density for 10^{16} seconds. A small initial time step ($t_0 \approx 10^6$ s) was used and allowed to increase up a maximum time step of 10^{12} seconds. Models were run with total hydrogen number densities varying from 0.01 cm^{-3} to 100 cm^{-3}, and temperatures ranging between 10^2 K and 10^4 K, and no external radiation. In each case, the results were compared to the results of a different implementation of the same chemical network within the ENZO code (Glover 2009, private communication, G09), yielding the molar fractions shown in Figure 2.2. In this figure, the three columns correspond to runs with different temperatures, the curves corresponds to runs with different densities, and the rows correspond to the evolution of different species.

The match between our tests and the numerical results from G09 is excellent. In all cases and at all temperatures, the curves closely track each

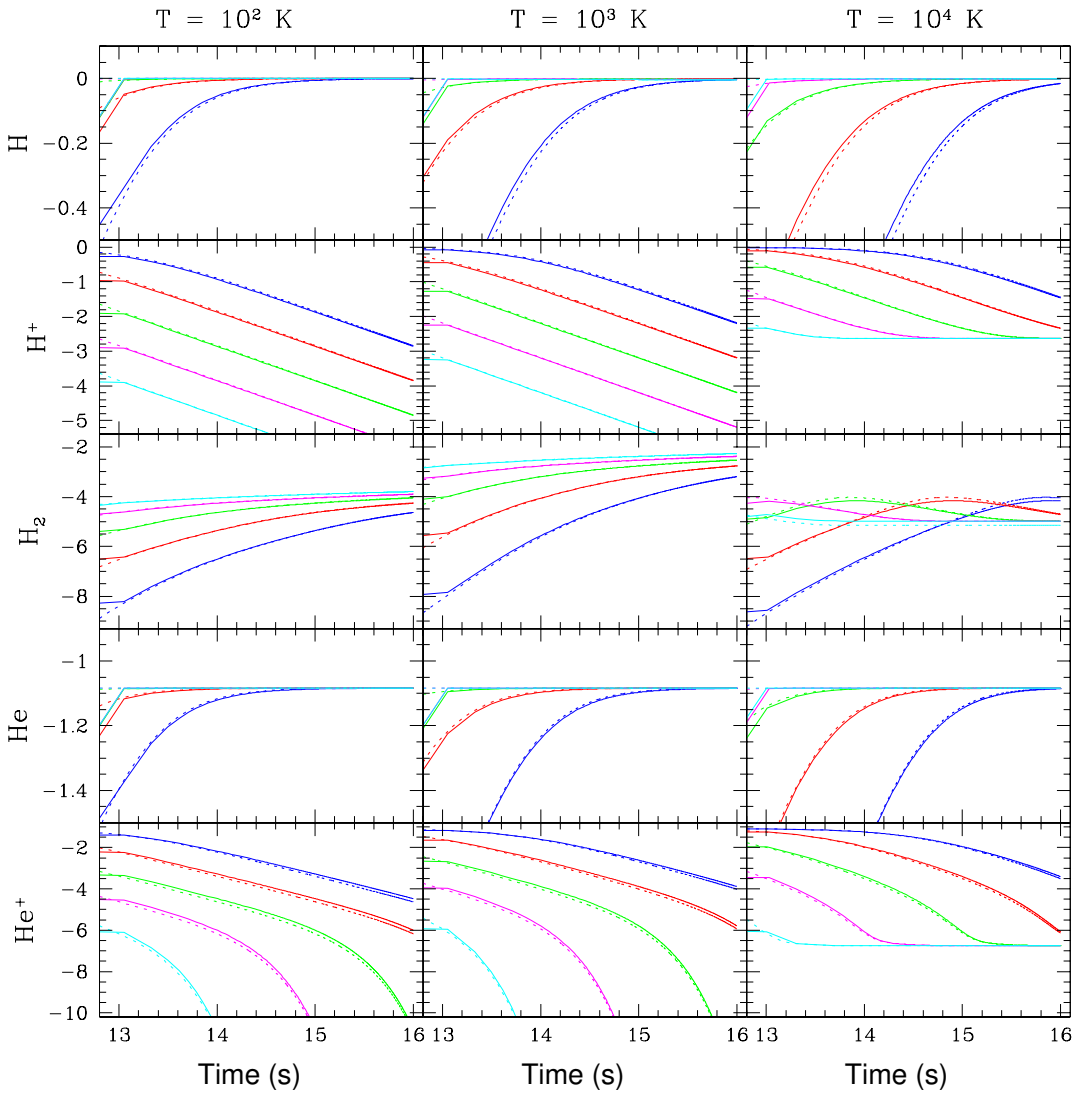

Figure 2.2: Chemical evolution tests. Column 1 shows the $T = 10^2$ K case, column 2 shows the $T = 10^3$ K case, and column 3 shows the $T = 10^4$ K. Time is given on the x-axis and the number density of each species divided by the total number density of hydrogen is given on the y-axis. The blue lines correspond to the $n = 0.01$ cm^{-3} case, red to the $n = 0.1$ cm^{-3} case, green to the $n = 1.0$ cm^{-3} case, magenta to the $n = 10.0$ cm^{-3} case, and teal to the $n = 100.0$ cm^{-3} case. The solid lines are results from FLASH and the dashed lines are results from G09.

other, in most cases leading to curves that are indistinguishable. Although the abundances of several species change by many orders of magnitude throughout the runs, the two methods track each other within to 10% in all cases except for H_2 at 10^4 K, which is unimportant as a coolant but nevertheless consistent within a factor of 1.5 at all times. Furthermore, this agreement between methods is also seen for deuterium species, which are not shown in this figure as they follow H exactly, maintaining a $\frac{1}{6000}$ ratio between both species at all times.

At $T = 100$ K, all ionized species quickly recombine with the free electrons to form neutral atoms. However, even during this relatively quick transition from ionized to neutral, H^+ and H^- ions (not shown) persist for long enough to catalyze the formation of substantial amounts of molecular gas, leading to final H_2 molar fractions of $\approx 10^{-4}$. At $T = 1000$ K, the evolution is very similar to the $T = 100$ K case, although the species do not reach equilibrium as quickly, leading to even higher levels of H_2 formation. Finally, at $T = 10^4$ K, it takes even longer for the ionized hydrogen to recombine, but in this case, less molecular species are formed, as collisional dissociation of H_2 and HD are more prevalent, limiting the maximum amount of these species.

Also apparent in these plots is the dependence of the species evolution on the density of the gas. Chemical reactions are fundamentally collisional processes whose rates are quadratic in number density. Thus, as we are not considering three-body interactions, the timescale associated with chemistry should decrease linearly with the density. This is seen for all temperatures and species shown in Figure 2.2, as in every case each line is separated from its neighbor by a factor of 10 in time, exactly corresponding to the density shift between cases.

Effect of the Background Radiation

Background radiation with photon energies between 11.2 and 13.6 eV can excite and dissociate molecular hydrogen. In the absence of other coolants, this can have drastic effect on the evolution of the cloud. Two extremes are immediately apparent, a strong background case in which any H_2 or HD formed is quickly dissociated, and a background-free case in which no molecules are photodissociated. A simple test was constructed to study the effect of the background and determine a fiducial value for J_{21}. J_{21} was varied between 0 and 1 at five different values. For each value of J_{21} the number density was varied between $n = 10^{-1}$ and 1.0 cm^{-3}. Each test was run at a constant temperature and constant density with evolving chemistry and no cooling. The results are given in Figure 2.3. From this, I determine that only background levels at or above $J_{21} = 0.1$ give an appreciable difference in the abundance of H_2 and HD over a megayear timescale, which as we shall show below, is the timescale of shock-minihalo interactions. At the same time, $J_{21} = 0.1$ provides a reasonable upper limit to the level of background expected before reionization (*e.g.* Ciardi & Ferrara 2005). Therefore, we use this value as a fiducial value in the simulations with a background.

Cooling

The second major process added to the code was radiative cooling, which was divided into two temperature regimes. At temperatures $\geq 10^4$K, cooling results mostly from atomic lines of H and He, with bremmstrahlung radiation also becoming important at temperatures above $10^7 K$. Below 10^4 K, on the other hand, the net cooling rate is determined by molecular line cooling from H_2 and HD, which, as it is an asymmetric molecule, can radiate much more efficiently

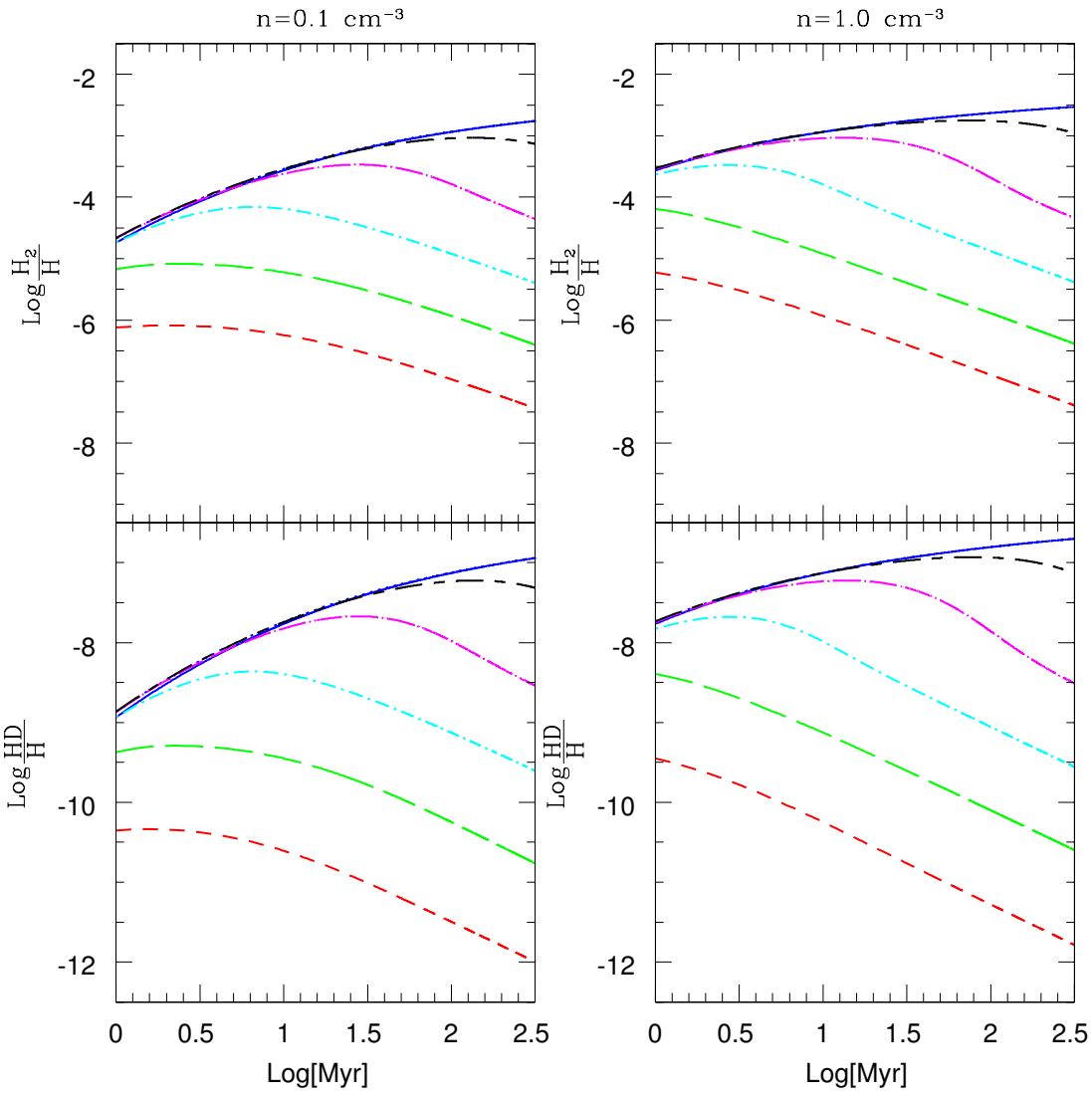

Figure 2.3: Comparison of different UV backgrounds. The dotted line is the comparison from G09, the solid line is $J_{21} = 0$, the short-and-long-dashed line is $J_{21} = 10^{-4}$, the dot-long-dashed line is $J_{21} = 10^{-3}$, the dot-short-dashed line is $J_{21} = 10^{-2}$, the long-dashed line is $J_{21} = 10^{-1}$, and the short-dashed line is $J_{21} = 1.0$. Time is given on the x-axis and number density of each species normalized by the number density of neutral hydrogen is given on the y-axis. Note that the solid line and dotted lines coincide with each other, demonstrating that we recover the expected results in the background-free case.

than H_2, and thus can be almost as important although it is much less abundant. Cooling from H_2 operates down to $T \leq 200$ K and to number densities $n > 10^4$ cm^{-3} (Glover & Abel 2008; Galli & Palla 1998), while HD which can cool the gas to slightly lower temperatures and to higher number densities (Bromm, Coppi, & Larson 2002). As we are restricting ourselves to primordial gas in this study at any given temperature the overall cooling rate, $\Lambda_{\rm Total}$, is the combination from both regimes,

$$\Lambda_{\rm Total} = \Lambda_{\rm Atomic} + \Lambda_{\rm Molecular}. \tag{2.13}$$

Each cooling rate has the form:

$$\Lambda_{i,j} = n_i n_j \lambda_{i,j}, \tag{2.14}$$

where $\Lambda_{i,j}$ is the energy loss per volume due to species i and j, n_i and n_j are the number densities of each species, and $\lambda_{i,j}$ is the cooling rate in ergs cm^3 s^{-1}. Cooling rates for the collisional excitation between H_2 and H, H_2, H^+, and e^- and between H_2^+ and H or e^- are taken from GA08. The cooling rate for the collisional excitation between HD and H is taken from Lipovka, Núñez-Lóez, & Avila-Reese (2005). Finally, cooling rates from Hydrogen and Helium atomic lines are calculated using CLOUDY (Ferland, G.J., *et al.* 1998). In calculating these rates, we follow the procedure described in Smith *et al.* (2008) and used the "coronal equilibrium" command which considers only collisional ionization. The cooling curve was calculated assuming case B recombination for the recombination lines of hydrogen and helium, as discussed further in §3.1.

Any cooling routine contains a natural timescale that relates the total internal energy to the energy loss per time:

$$\tau_{\rm cool} = \frac{\alpha_{\rm cool} \times E_i}{\dot{s}}, \tag{2.15}$$

where $\alpha_{\rm cool}$ is a constant between 0 and 1, in all cases set at 0.1, E_i is the internal energy, and $\dot{s}$ is the energy loss per time. Cooling rates are very dependent on temperature and species abundances and these quantities can change rapidly over a single chemical time step.

A method of subcycling over cooling time steps was developed to ensure that the correct cooling rates are used. An initial cooling time scale is calculated assuming $\alpha_{\rm cool} = 0.1$ using eqn. (2.15) which is then compared to the chemical time step. If $\tau_{\rm cool}$ is smaller than the fraction of the chemistry time step then that fraction of energy is subtracted from the internal energy and temperature. The cooling rate and cooling time step is recalculated with the updated temperature. This continues until the chemistry time step is reached. This is schematically given in Fig. 2.4.

Cooling Tests

As a test of our cooling routines, we reproduced the example curves given in Prieto *et al.* (2008). In this work, the authors present the effects of H_2 and HD cooling in a primordial gas. The gas begins at an initial temperature of $T = 500$ K with initial number densities, relative to hydrogen:
$n_{\rm H^+} = 10^{-4}; n_{\rm H^-} = n_{\rm H_2^+} = 10^{-12}; n_{\rm H_2} = 10^{-3}; n_{\rm D} = 10^{-5}; n_{\rm D^+} = 10^{-9}; n_{\rm HD} = 10^{-6}; n_{\rm HD^+} = 10^{-18}; n_{\rm He^+} = n_{\rm He^{++}} = 0.0$l and with initial hydrogen and helium densities of $\rho_{\rm H} = 0.75 \times \rho_{tot}$ and $\rho_{\rm He} = 0.24 \times \rho_{tot}$, where ρ_{tot} is the total baryonic matter density.

Three models were run with total number densities of $n_{tot} = 1.0, 10.0,$ and 100.0 cm^{-3}. Cooling was tracked for 10^8 yrs with chemistry evolving simultaneously. The results of this calculation are shown in Figure 2.5, which indicates good agreement with Prieto *et al.* (2008). It should be noted that temperature evolution in this plot has a linear dependence of the number density

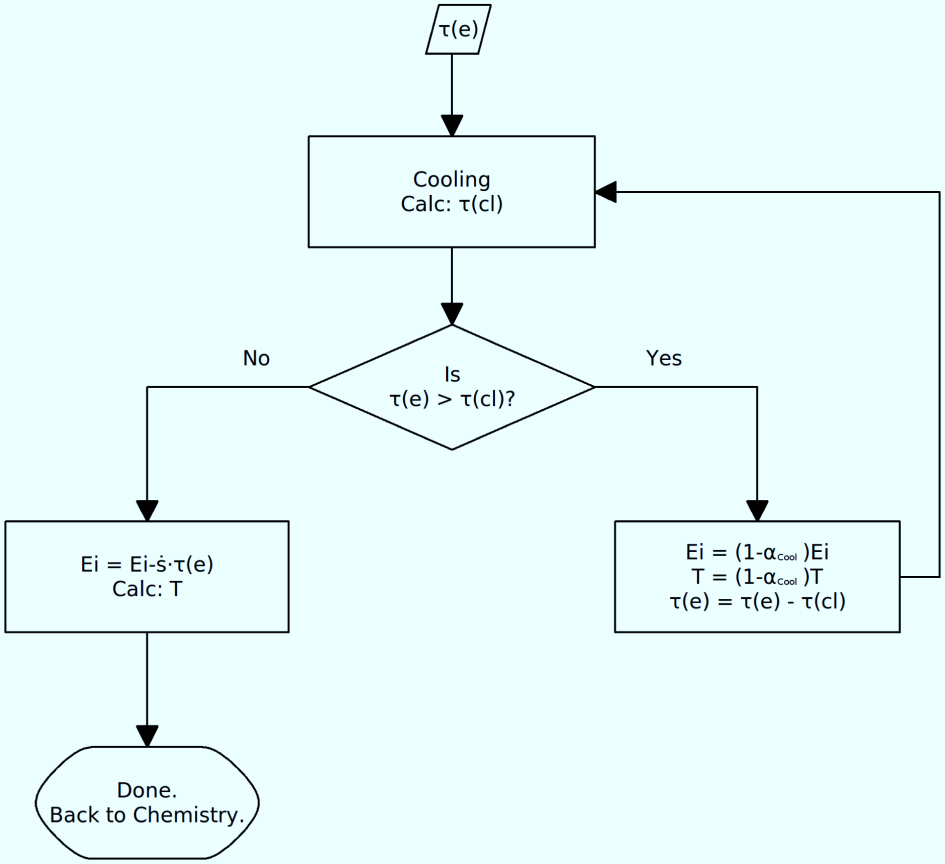

Figure 2.4: Schematic view of the cooling subcycle. The time over which chemistry evolves $\tau(e)$ is used as the initial time step. This is compared against $\tau(cl)$ the cooling time step, as given by eq. (2.15). If the cooling time step is shorter than the evolved time step, then a portion of the internal energy and temperature are subtracted and the evolved time step is updated. The cooling time step is then recalculated. If the cooling time step is longer than the evolving time step then the internal energy is directly updated and used to calculate the new temperature. Once this is done, cooling is complete and we return to the chemistry routine

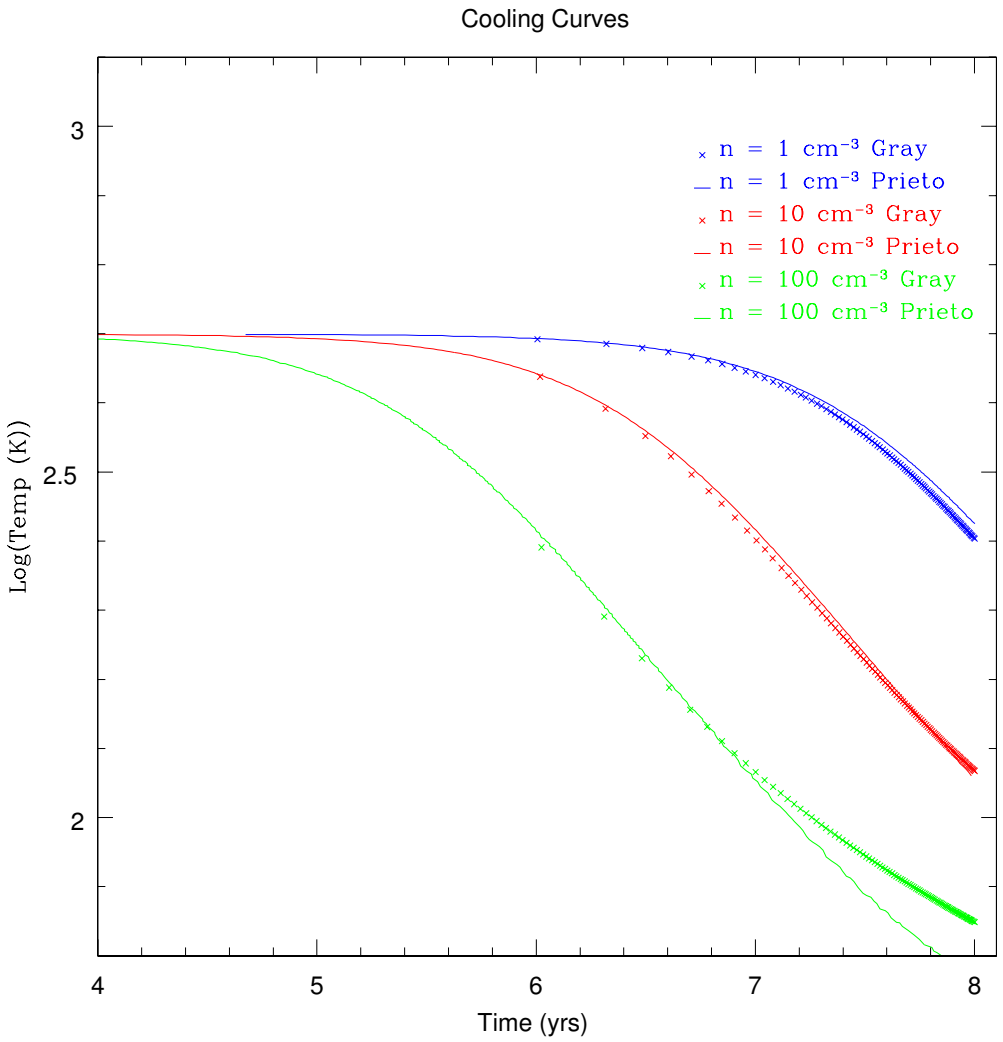

Figure 2.5: Cooling tests. The solid lines are taken from Prieto *et al.* (2008) and compared to our model. The blue curves correspond to a number density $n = 1.0$ cm^{-3}, red to $n = 10.0$ cm^{-3}, and green to $n = 100.0$ cm^{-3}. The temperature is not allowed to go below 50 K.

of the gas. For example, a gas with ten times the number density of another gas will cool ten times quicker. This is again because most of the cooling is coming from the collisions between two species, in this case H_2 or HD and H.

As mentioned above, HD can be more important than H_2 for gas cooling at higher densities and colder temperatures. To determine whether or not HD cooling is important in this simulation, we apply the cooling test to two different

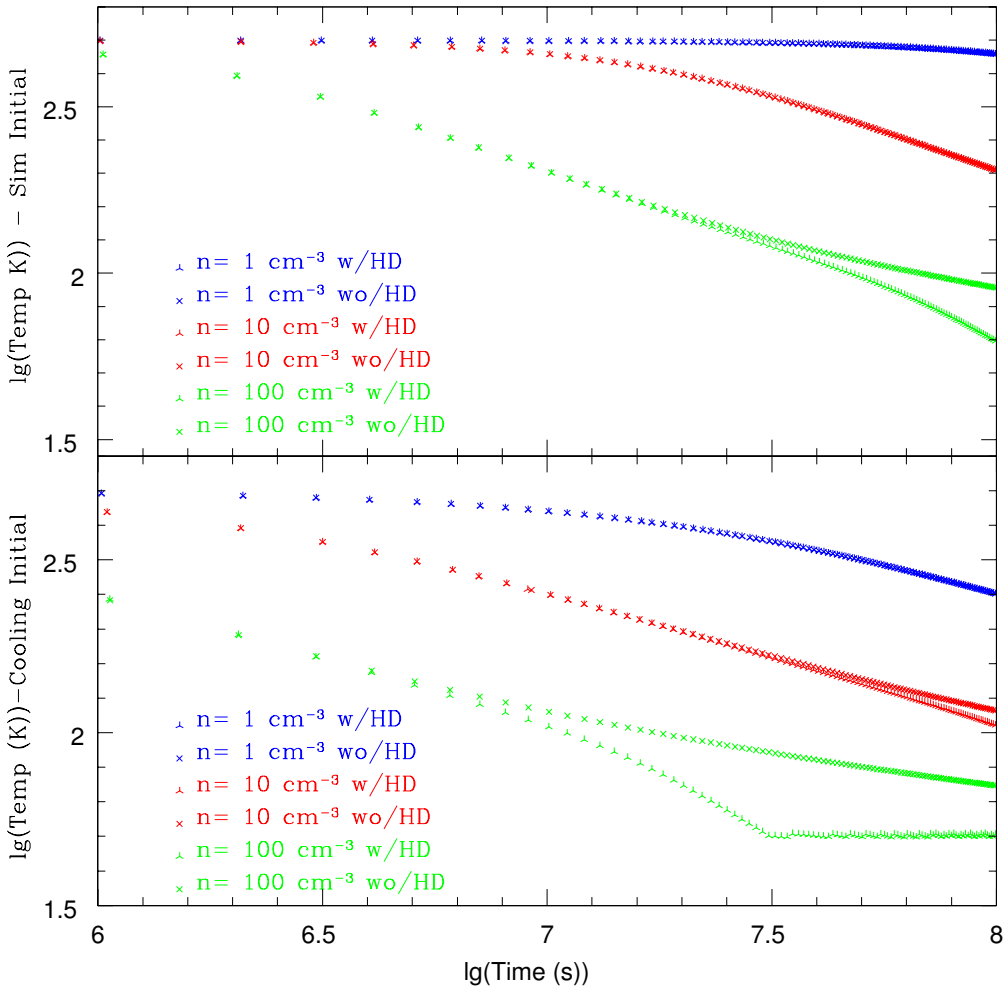

Figure 2.6: Test of the impact of HD cooling. The top panel shows the results using primordial abundances while the bottom shows for abundances from the cooling test. Initially, the temperature is started at 500 K and evolved for 100 Myrs.

scenarios. First, we use the same initial abundances as described above and second, using primordial abundances with a small fraction (0.01%) of each atomic species ionized. Each test was run twice, once with deuterium and once without. The results of these tests is given in Figure 2.6. At high number densities, HD cooling does not have a perceivable effect. At intermediate temperatures, HD cooling is important for a gas with the initial abundances from the cooling tests. Finally, at low temperatures, HD cooling is very important in both cases.

Note on Chemistry Rate Uncertainties

The primary source of uncertainty in our chemistry network comes from the uncertainty in the individual chemistry rates. For example, even important reactions, such as the associative detachment or mutual neutralization of hydrogen, can be uncertain by up to an order of magnitude. If fact, it is these two reactions that can have a large impact on the final abundance of H_2 and, therefore, cooling in primordial gas (G08; Abel *et al.* 1997). In general, the reaction rates are either experimentally measured in a laboratory setting or computed using theoretically calculated cross sections for a given species. In this work, we have used the default rates as presented in G08 as well as the important cooling functions. While this represents a fairly up-to-date chemistry network, further experimental and theoretical work is required to constrain these uncertain rates.

2.1 Model Framework

Having developed and tested the chemistry and cooling routines necessary to study minihalo-shock interactions, we then turn to the detailed shock-minihalo interactions. Here we restrict our attention to a Cold Dark Matter (CDM) cosmology, with parameters are $h = 0.7$, $\Omega_0 = 0.3$, $\Omega_\Lambda = 0.7$, and $\Omega_b = 0.045$

(*e.g.* Spergel *et al.* 2007), where h is the Hubble constant in units of 100 km s^{-1} Mpc^{-1}, Ω_0, Ω_Λ,and Ω_b are the total matter, vacuum, and baryonic densities, respectively, in units of the critical density. For our choice of h, the critical density is $\rho_{crit} = 9.2 \times 10^{-30}$ g/cm^3.

The Minihalo

A simple model is used for the gas and dark matter of the protocluster whose collapse redshift of $z_c = 10$ (a cosmic age of $\approx$ 0.5 Gyr) is taken to be just before the epoch of reionization, and whose total mass of $M_c = 3.0 \times 10^6 M_\odot$ is taken to be on the large end of minihalos formed at this redshift. The gas is assumed to have a primordial composition of 76% neutral atomic hydrogen and 24% neutral atomic helium by mass. Initially, the cluster has a mean density that is enhanced by a factor $\Delta = 178$ (e.g. Eke, Navarro, & Frenk 1998) above the background, $\rho_c = \Delta\Omega_0(1+z_c)^3\rho_{\rm crit} = 6.54 \times 10^{-25}$gm/cm^3. In this case, the cloud's virial radius is $R_c = 0.393$ kpc and virial velocity of $v_c = 6.55$ km/s. We assume that the radial profile is given by Navarro *et al.* (1997)

$$\rho(R) = \frac{\Omega_0\rho_c}{cx(1+cx)^2}\frac{c^2}{3F(c)}\ \mathrm{gm/cm^3}, \tag{2.16}$$

where c is the halo concentration factor, $x = R/R_c$, and $F(t) \equiv \ln(1+t) - \frac{t}{1+t}$. We assume that as the gas collapses inside the dark matter halo, it is shock-heated to its virial temperature, $T_c = 1650$ K and develops a density distribution of isothermal matter in the CDM potential well:

$$\rho_{\rm gas}(R) = \rho_0 e^{-\left(\frac{v^2_{\rm esc}(0) - v^2_{\rm esc}(R)}{v_c^2}\right)}\mathrm{gm/cm^3}. \tag{2.17}$$

where the escape velocity is as a function of radius is given by $v(xR_{\rm vir}) = 2v_c^2[F(cx) + cx(1+cx)^{-1}][xF(c)]^{-1}$. From Madau *et al.* (2001), we take a typical value of the halo concentration to be $c = 4.8$, although some observations suggest that high-redshift haloes maybe less concentrated than

Table 2.1: Optical Depths. τ is the optical depth to the center of the cloud. In all cases the optical depth is much greater than 1.

Species	Incident Energy eV	τ
H^+	13.6	3553.9
He^+	24.6	1049.2
He^{++}	54.4	280.6

expected from this estimate (Bullock *et al.* 2001). With this value of c, we can compute the central density as:

$$\rho_0 = \frac{(178/3)c^3\Omega_b e^A (1+z)^3}{\int_0^c (1+t)^{A/t}\, t^2 dt}\rho_{\rm crit} = 39215\ \Omega_b \rho_{\rm crit}\,(1+z_c)^3 = 2.16\times 10^{-23}{\rm gm/cm}^3, \tag{2.18}$$

where $A \equiv 2c/F(c) = 10.3$ and $t = cx$.

To determine which case to use in our chemistry routine the optical depth for H^+, He^+, and He^{++} recombination was calculated from this profile:

$$\tau_\nu(r) = \int_{r_0}^{r} \sigma_\nu n(r')dr', \tag{2.19}$$

where σ_ν is the cross section of interaction and $n(r')$ is the number density. For hydrogen-like atoms the cross section is

$$\sigma_\nu = \frac{7.91\times 10^{-18}}{Z^2}\left(\frac{\nu_1}{\nu}\right)^3\ {\rm g}\ \ {\rm cm}^2, \tag{2.20}$$

where $h\nu_1 = 13.6\ Z^2$ eV and Z is the nuclear charge. Calculating the optical depth from eqs. (2.17 - 2.20) yields the results given in Table 1. We assume for the case of He^{++} recombination, that the surrounding helium is singly ionized. In all cases the optical depth is much greater than 1 (see §3.0) and therefore we use case B rates for all recombination reactions in our fiducial simulations.

Gravity

As the minihalo in our simulation is made up of both gas and collisionless dark matter, a two-part gravity scheme was required. First, the Ricker (2008)

multigrid Poisson solver was used to calculate the gravitational potential due to the gas component. Second, the acceleration due to the total matter was calculated using Eq. (2.17) above. The general equation for the gravitational acceleration of an ideal gas is given by $a_{\rm Grav} = \frac{k}{\rho(R)m_p}\left[T(R)\frac{\partial\rho(R)}{\partial R} + \rho(R)\frac{\partial T(R)}{\partial R}\right]$ cm/s^2. To account for the dark matter halo's contribution to gravity, we calculated the gravitational acceleration of the total matter and subtracted its contribution from the baryonic matter in the initial configuration using the above equation with constant temperature. Finally, we add the gravitational contribution from the self-gravity of the gas. The total acceleration is given simply by:

$$a_{\rm Tot} = a_{\rm M,0} - a_{\rm gas,0} + a_{SG}, \tag{2.21}$$

where a_M is the acceleration from the total initial mass density as given by Eq. (2.17), $a_{\rm gas,0}$ is the contribution from the baryonic matter in the initial configuration, and a_{SG} is the contribution from the self-gravity calculated from the Poisson solver. Initially, when the minihalo gas is in hydrostatic balance with its surroundings, these last two terms will cancel each other and the cloud will remain unchanged. When the cloud is disrupted and cooling takes effect, the self-gravity will cause the cloud to collapse.

The above equations are correct up to the viral radius of the cloud. To ensure a smooth density transition from the cloud, we simply keep the gas outside of the cloud be gravitationally bound to the cloud and solve for the expected density profile. The acceleration here is then,

$$a_{\rm Grav} = -\frac{GM(R > R_c)}{R^2}, \tag{2.22}$$

and the density is

$$\rho(R > R_c) = \rho(R_c)e^{\left(\frac{R_0}{R} - \frac{R_0}{R_c}\right)}, \tag{2.23}$$

with $R_0 = GM_c m_p / k_b T$. Here G is the gravitational constant,m_p is the mass of a proton, k_b is Boltzmann's constant, and, as above M_c and T_c are the mass and temperature of the cloud. As $R \to \infty$, the density goes down to a small fraction of $\rho(R_c)$. A test of our gravity routine showed that the cloud was able to maintain hydrostatic balance for many dynamical times in the absence of an impinging galaxy outflow.

The Outflow

A Sedov-Taylor solution is used to estimate the properties of the galactic outflow. The initial input energy is taken to be $E = \epsilon E_{55}(\text{ergs})$, where E_{55} is the energy of the supernovae driving the wind in units of 10^{55} ergs, and the wind efficiency ϵ is derived from the amount of kinetic energy from the supernovae that is channeled into the outflow. The shock expands into a gas that is δ times greater than the background at a redshift of z_c. As in Scannapieco *et al.* (2004), we assume that the cloud is a distance $R_s = 3.6$ kpc, using fiducial values: $z_c = 10$, $E_{55} = 10$, $M_6 = 3$, $\delta = 44$ and $\epsilon = 0.3$.

With these values, the velocity of the blast front is $v_s = 225$ km s^{-1}, when it reaches the minihalo, and the resulting temperature of the fully-ionized post-shock medium is $T = 2.4 \times 10^6$ K. By the time the shock has covered the separation distance, R_s, it will have entrained a mass

$$M_{s,\text{Total}} = 4.4 \times 10^7 \text{ M}_\odot, \tag{2.24}$$

with a surface density of

$$\sigma_s = 2.6 \times 10^5 \text{ M}_\odot \text{ kpc}^{-2}. \tag{2.25}$$

Note that while the above equations are the solutions that come from a simple spherical blast wave, the wind in the simulation is still well-approximated

by a plane wave solution, because the size of cloud is much smaller than the distance between the supernova and the cloud.

To model this wind, a time-dependent boundary condition is imposed at the leftmost boundary of the simulation volume. The expected lifetime of the shock is given by $\sigma_s = v_{\rm post}\,\rho_{\rm post}\,t_s$, where $v_{\rm post}$ is the post-shock velocity of the blast wave, $\rho_{\rm post}$ is the post-shock density, and σ_s is the surface density of the entrained material. Solving for t_s and putting in the appropriate values, the expected shock life time is $t_s = 2.5$ Myr. After this time the shock begins to taper off with the density decreasing and temperature increasing and keeping the pressure constant. This is done to prevent the excessive refinement that a sharp cutoff would cause. The density falls off as

$$\frac{\rho(t)}{\rho(0)} = 0.01 + 0.99e^{-\tau_s/1.5} \tag{2.26}$$

and the temperature rises as

$$\frac{T(0)}{T(t)} = 0.01 + 0.99e^{-\tau_s/1.5}\ , \tag{2.27}$$

where τ_s is defined as $\frac{t-1\ \rm Myr}{1\ \rm Myr}$. This also prevents the hydrodynamic (Courant) timestep from becoming extremely short behind the shock, in order to maintain pressure equilibrium in an extremely rarified medium.

Note that in this initial study, the dark matter and gas distributions have been somewhat idealized, and more complicated geometries could be used to model these components in greater detail. For example, a triaxial instead of a spherical distribution could be assumed for the dark matter halo, inhomogeneities could be added to the minihalo gas, and the shock could be assumed to impact the minihalo off-axis. While each of these possibilities would be qualitatively interesting, and naturally alter the final outcome of the halo, they are nevertheless beyond the scope of this study.

Table 2.2: Summary of the numerical simulations in this study.

Name	l_{ref}	Resolution(pc)	Cooling Mode	Background (J_{21})
HBN	6	4.55	Case B	0
LBN	5	9.11	Case B	0
HBY	6	4.55	Case B	10^{-1}
LBY	5	9.11	Case B	10^{-1}
HAN	6	4.55	Case A	0
LAN	5	9.11	Case A	0

2.2 Results

My simulations were carried out in a rectangular box with an effective volume of 3.2 $\times 10^9$ pc^3. The y-axis and z-axis were the same length of 1170 pc and range between [-585, 585] pc while the x-axis was twice as long, stretching between [-585, 1170] pc. The shock started on the left boundary while the cloud was centered at [0,0,0] pc. As hydrodynamic refinement criteria, FLASH uses the second derivative of "refinement variables," normalized by their average gradient over a cell. If this was greater than 0.8, the cell was marked for refinement, and if all the cells in a region lie below 0.2, those cells were marked for derefinement.

A detailed summary of the runs performed is given in Table 2. The runs are labeled as either high or low resolution (H or L), whether atomic H-He recombination follows Case A or Case B (A or B), and whether I impose a UV background (Y or N). The high-resolution, Case B, no-background run (HBN) is taken to as our fiducial run and compared against other choices of parameters below.

Hydrodynamic Evolution

In this simulation, several distinct stages of evolution are identified during the interaction between the cloud and the outflow, as shown in Figures 2.7 and 2.8. Initially, the cloud is in hydrostatic equilibrium as the shock enters the

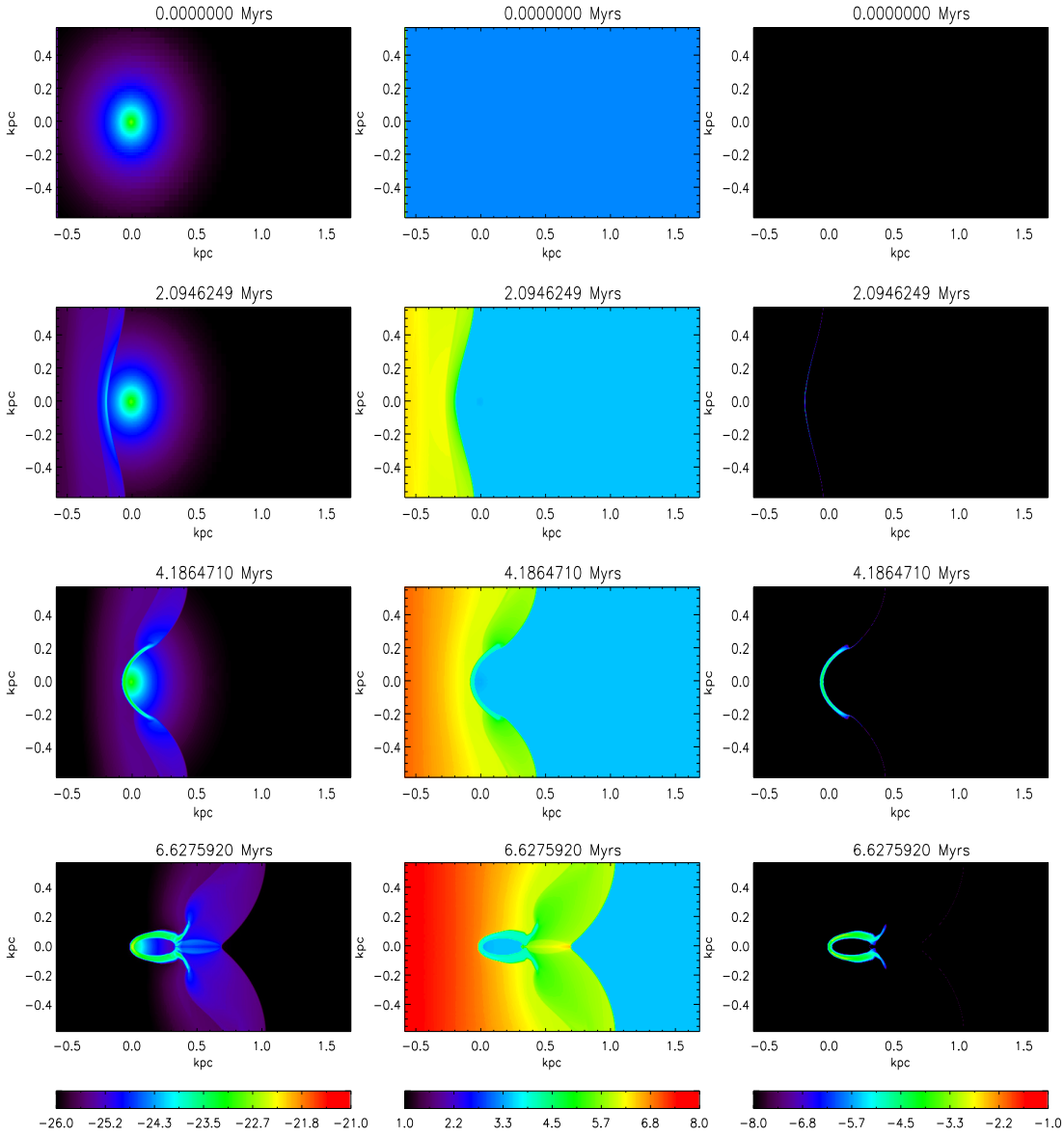

Figure 2.7: Initial evolution of the fiducial run, HBN, from $t = 0$ through $t = t_{\rm ic}$ the time the shock completely surrounds the cloud. Each row shows the conditions in the central in a slice through the center of the simulation volume at times of 0 (top), 2.1 (second row), 4.2 (third row), and 6.6 Myrs (bottom row). The first column shows contours of the log of density from $\rho_{\rm gas} = 10^{-26}$ to 10^{-21} g cm^{-3}, which corresponds to number densities from $n \approx 10^{-2}$ to 10^{2}, the second column shows contours of the log of temperature from $T = 10$ to 10^{8}K, and the third column shows contours of the log of the H_2 mass fraction from $X_{\rm H_2} = 10^{-8}$ to 10^{-1}.

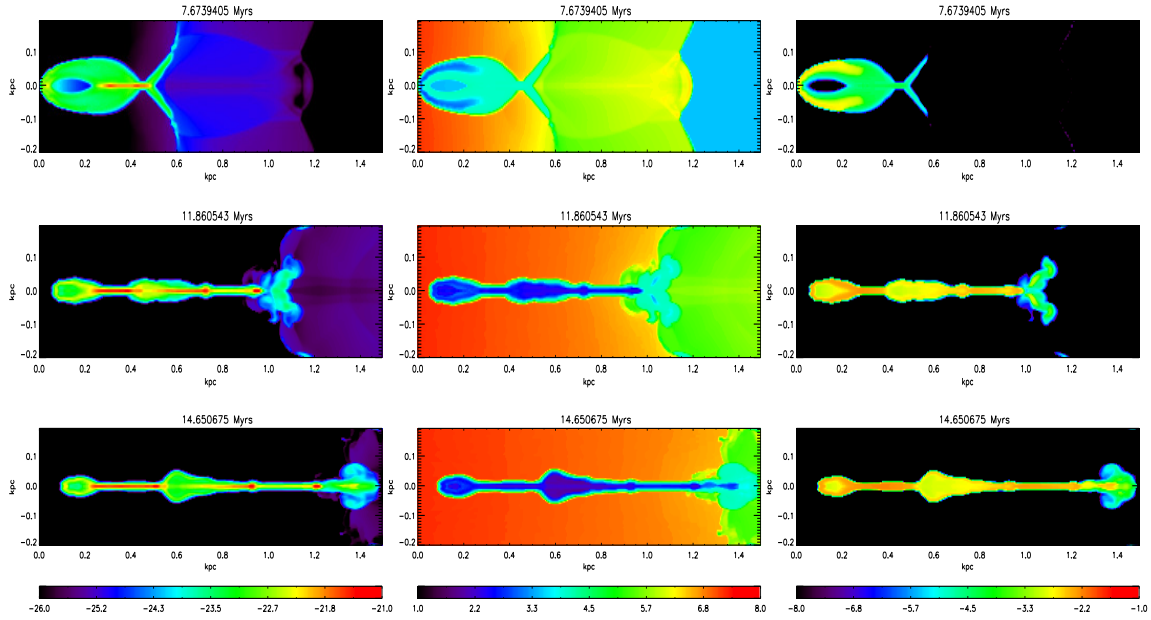

Figure 2.8: Final evolution of the cloud from the propagation of the reverse shock across the cloud at $t = 7.7$ Myrs (top row), to collapse at $t = 11.8$ Myrs (center row), through to the end of the simulation at $t = 14.7$ Myrs (bottom row). The panels have been cropped to show only the extended mass along the x-axis. Columns, values, and contours are the same as Fig. 2.7.

simulation domain. If it were not supported by pressure, the cloud would collapse on the free-fall time which, using the average cloud density, is

$$t_{\rm ff} = \sqrt{\frac{3\pi}{32G\rho}} \approx 100 \text{ Myr}. \tag{2.28}$$

As the cloud is initially in hydrostatic balance, the initial sound crossing time is similar to the free-fall time.

As the shock contacts and surrounds the cloud, it heats and begins to ionize the gas. The shock completely envelops the cloud on a characteristic "intercloud" crossing time scale, defined by Klein *et al.* (1994) as

$$t_{\rm ic} = \frac{2R_c}{v_s} \approx 4.5 \text{ Myr}. \tag{2.29}$$

As the cloud is enveloped, the shock moves through the outer regions fastest and

ionizes this gas first. This in turn promotes rapid molecule formation as the gas cools and recombines incompletely, leaving H^+ and H^- to catalyze the formation of H_2 and HD. Interestingly, because the shock slows down as it moves through denser material, the gas behind the center of the halo remains undisturbed until the enveloping shocks meet along the axis at the back of the halo. The leads to a "hollow" H_2 distribution at 6.6 Myrs, in which the molecular coolants are confined to a shell surrounding the undisturbed, purely atomic gas.

After the enveloping shocks collide at the back of the cloud, a strong reflected shock is formed that moves away from the rear of the cloud and back through the halo material. Without cooling, this reflected shock would eventually lead to cloud disruption (Klein *et al.* 1994). However in our case, the shock has the opposite effect. It moves through the cloud, and the gas is briefly ionized, but then quickly cools and recombines, forming H_2 and HD throughout the cloud. This can be seen in the upper row of Figure 2.8, which shows the conditions at ≈ 8 Myrs.

At this point the cloud is denser, smaller, and full of new coolants. Using the conditions from the center of the cloud 8 Myr after the start of the simulation, we calculate new timescales. Now the freefall time is 21 Myr and the sound crossing time is ≈ 27 Myr. The cloud is cold and dense enough to start collapsing.

The timescale for the formation of H_2, given in GA08, is

$$t_{\mathrm{H_2}} = \frac{X_{H_2}}{k_1 X_e n}(\mathrm{s}), \tag{2.30}$$

where $X_{\mathrm{H_2}}$ is the mass fraction of H_2, X_e is the mass fraction of electrons, k_1 is the reaction rate for the formation of H^- ($H + e^- \rightarrow H^- + \gamma$), and n is the total number density (≈ 1 cm^{-3} at 8 Myrs). Initially, as the shock begins to impact

the cloud, this timescale is very short, on the order of 0.1 Myrs to get a final abundance of $\approx 10^{-5}$. As the abundance of H_2 increases and the abundance of electrons decrease, this timescale quickly increases. Although as the cloud collapses the density increases which lowers this timescale.

The H_2 cooling timescale, given by Klein *et al.* (1994) is

$$t_{\rm cool} = \frac{1.5nkT}{n_{\rm H_2} n_{\rm H} \Lambda_{\rm H,H_2}} \text{ (s)}, \tag{2.31}$$

where $n_{\rm H_2}$ and n_H are the number densities of H_2 and H respectively, and $\Lambda_{\rm H,H_2}$ is the cooling rate between H and H_2. At 8 Myr the H_2 cooling time in most of the cloud is only 0.2 Myr, meaning that pressure support drops dramatically after this time. Any expansion due to shock heating is halted as the gas is quickly cooled by H_2 and HD as they form. Furthermore, as the cloud collapses, the chemistry and cooling timescales decrease, rapidly accelerating the collapse.

The final state of the cloud in our simulation is a thin cylinder stretching from the center of the dark matter halo to several times the initial virial radius. The temperature of this gas is 100 to 200 degrees, much colder than the initial virial temperature. The gas is also much denser than the initial minihalo, reaching values of up to 10^{-21} cm^{-3} or $n \approx 10^3$ cm^{-3}, in the center of the cloud, and even this density is probably only a lower limit set by the resolution of our simulation. On the other hand, the cloud is quite extended along the x-axis, with substantial differences in velocity along the cylinder. Thus it is continually stretched and fragments until the end of the simulation at 14.7 Myrs (Row 3 in Figure 2.8).

Figure 2.9 shows rendered density contours of the major stages of evolution of the cloud from $t = 0$ through the end of the simulation. The first panel shows the initial configuration, with the cloud in hydrostatic equilibrium,

and the shock front entering from the left side of the simulation volume. The next panel shows the cloud after being impacted by the shock, highlighting the density enhancement in the outer shell of the minihalo gas. The bottom left panel shows the cloud as it begins to cool and collapse, at a time at which the reverse shock has already passed though the cloud and coolants are found throughout the shocked, recombined material. Finally, the last panel shows the distribution at the end of the simulation. The cloud has now been stretched over a large distance and much of its mass has been accelerated to above the escape velocity, moving outside of the dark matter halo. The dense knots of this material in this figure are tightly gravitationally bound, have number densities approaching 10^3 cm^{-3}, and are destined to form extremely compact stellar clusters.

Stellar Clusters

While the collision happens on order of the shock crossing time of the halo, the final distribution of the clumps evolves on the longer timescale defined by $R_{\rm vir}/v_c \approx 100$ Myrs. To study the final state of the stretched and collapsed distribution without continuing the simulation out to such extremely long times, we divide the x-axis into 100 evenly spaced bins between $x = 0$ kpc and $x = 1.4$ kpc. we then calculate the mass of each bin by summing up the gas from each cell from the FLASH simulation in a cylinder with a 24 pc radius and length of the bin. Similarly, we calculate the initial velocity of each bin by adding the momentum from each cell within this cylinder and dividing by the total mass in each bin.

We evolve this distribution forward in time using a simple numerical model, which assumed that motions were purely along the x axis and pressure was negligible at late times. In this case, acceleration could be calculated

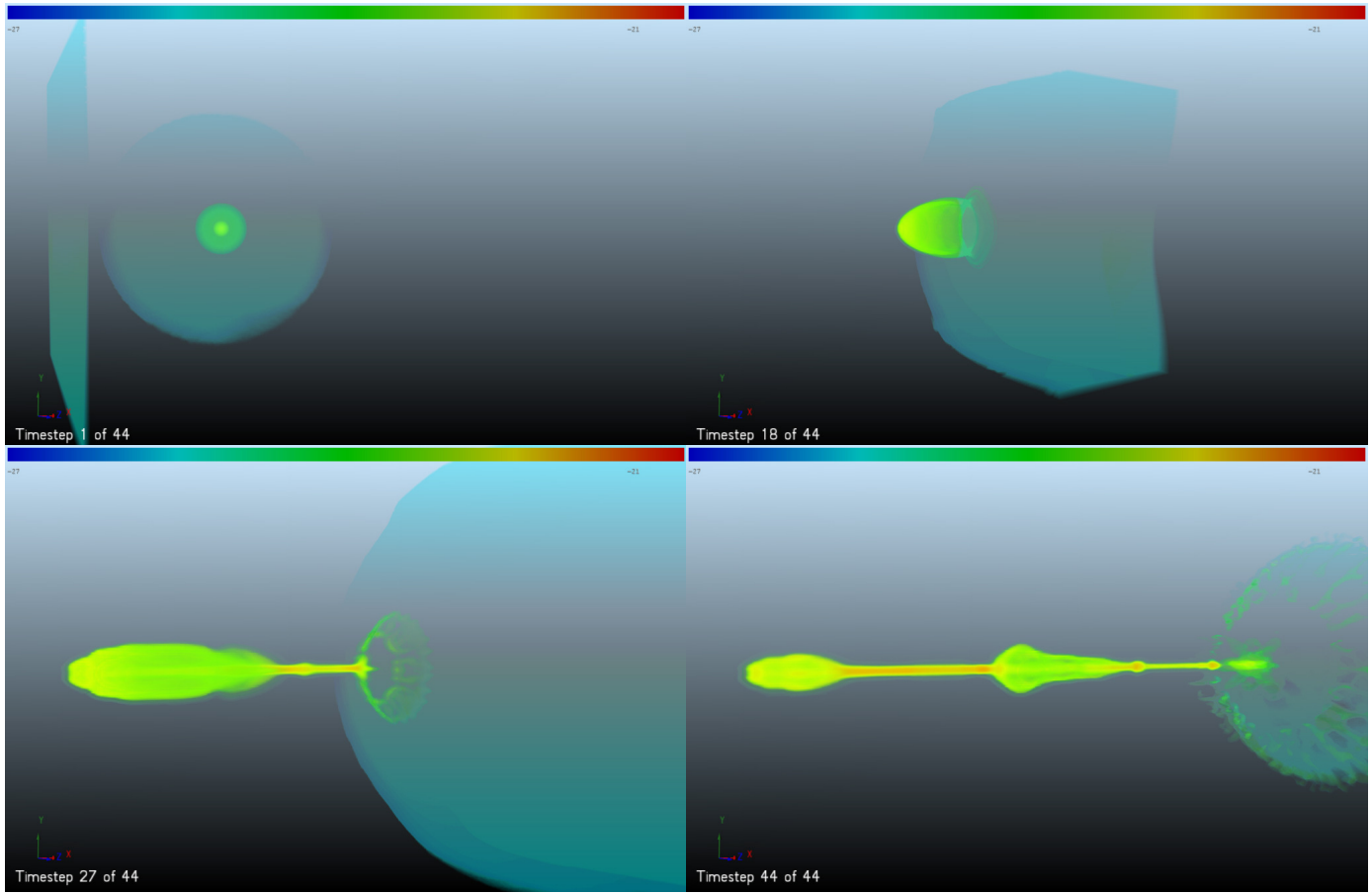

Figure 2.9: Rendered density snapshots from the fiducial run, HBN. Colors show contours of log ρ from 10^{-27} to 10^{-21} cm^{-3}. The top left panel, $t = 0.0$ Myrs, shows the initial setup with the stationary minihalo and the shock entering on the left. Top right, $t = 6.3$ Myrs, shows the state of the cloud as the shock as it envelopes the cloud. Bottom left, $t = 9.4$ Myrs, shows the cloud during collapse and cooling. Finally, bottom right, $t = 14.7$ Myrs, shows the final state of the cloud as it is stretched. Dense clumps can be seen in this panel, which we expect to become compact stellar clusters.

directly from the gravity between each pair of particles and from the potential of the dark matter halo. Furthermore, if any given particle moved past the particle in front of it we merge them together, adding their masses and calculating a new velocity from momentum conservation.

Evolving the distribution in this way for an additional 200 Myrs past the end of the simulation yielded the results shown in Figure 2.10. As the stretched cloud continues to move outward, particles begin to attract each other, and eventually merge together to create larger clumps. By 100 Myrs most of the particles have merged, after which their motions are purely ballistic. This can seen in the top panel as the lines for the late times overlap each other and in the middle panel as the velocity profiles overlap.

At the final time of 200 Myrs after the end of numerical simulation, three small, stable clumps with masses of 5.0×10^4 $M_\odot$, 4.0×10^4 $M_\odot$, and 3×10^4 $M_\odot$, as can be seen in the top panel of Fig. 2.10. Each of these new peaks is located far outside of the original dark matter halo.

Case A vs. Case B

At temperatures above 10^4 K, the primary source of cooling is atomic lines from hydrogen and helium. Although we have shown that for the primordial cloud, Case B rates should be used for both the chemical network and cooling functions, Figure 2.11 shows a comparison between our fiducial run, HBN, and a run in which reaction and cooling rates are taken for case A recombination (HAN). The high temperature Hydrogen-Helium cooling curve is taken from Weirsma *et al.* (2009). The upper panels show density contours and the bottom show contours of H_2 abundance.

As expected, the Case B simulation produces greater molecular coolant abundance at similar overall densities. This difference can be seen in the lower

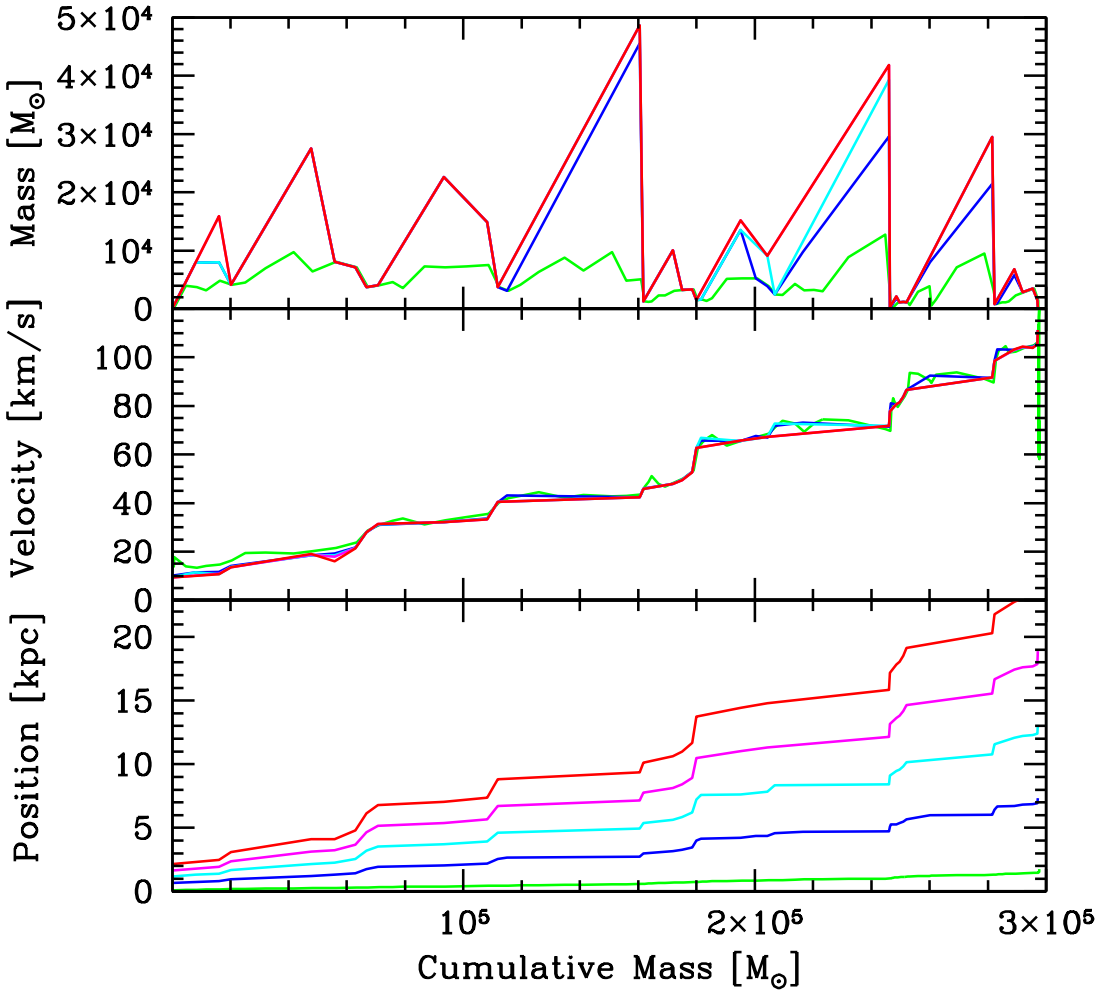

Figure 2.10: Evolution of the cloud up to 200 Myrs after the end of the simulation. The x-axis in each panel is the cumulative mass in solar masses. The top panel shows the mass of each particle, the middle panel shows their velocities, and the bottom panel shows their positions. The solid green lines show the profile at the end of the simulation $t_f = 14.7$ Myrs, the dotted blue lines show the profile 50 Myrs later, the short-dashed cyan lines show the profile at $t_f + 100$ Myrs, the dot-short dashed magenta lines show the profile at $t_f + 150$ Myrs, and finally the short dash-long dashed red lines show the profile at $t_f + 200$ Myrs. As time progresses we find that much of the material in the linear feature from Fig. 2.8 merges together. Most of this merging is complete by 100 Myrs after the end of the simulation.

two panels of the first column of Fig. 2.11 at 6.63 Myrs. To remain in pressure support as the cloud becomes denser from the shock, the cloud must get hotter. However, because Case A cools slightly faster, this support is quickly removed and the cloud takes on a more extended shape as evident in the first two columns of Fig. 2.11. Although, by 14 Myrs the abundance of molecular coolants are very similar between HBN and HAN with each containing $X_{H_2} \approx 10^{-2.5}$.

In both cases, the fate of the minihalo gas is the same. Atomic cooling occurs sufficiently rapidly to sap the shock of its energy and drop the post-shock temperature to $\approx 10^4$ K, and nonequillibrium processes step in to provide molecular coolants below 10^4 K. The gas is then able to collapse and form into a long dense filament within which clumps are formed. In fact the only substantial differences between the runs are the details of the distributions of clumps, which is somewhat more extended in the case A run as compared to the case B run.

UV Background

A more uncertain aspect of our simulation is the assumption of a negligible dissociating background. In fact, the presence of at least a low level of dissociating background is necessary in order for the minihalo not to collapse and form stars on its own, cooling by H_2 and HD left over from recombination. To set an upper limit on the impact of such a background we modify the rates in our chemical network to approximate a relatively large dissociating background of $J_{21} = 0.1$, as discussed in section 2.1. Furthermore, as these rates are modified for all reactions throughout the simulation, this background is taken to affect even the densest regions of the cluster. This is equivalent to assuming that the cloud is optically thin to 11.2 to 13.6 eV photons at all times during the simulation.

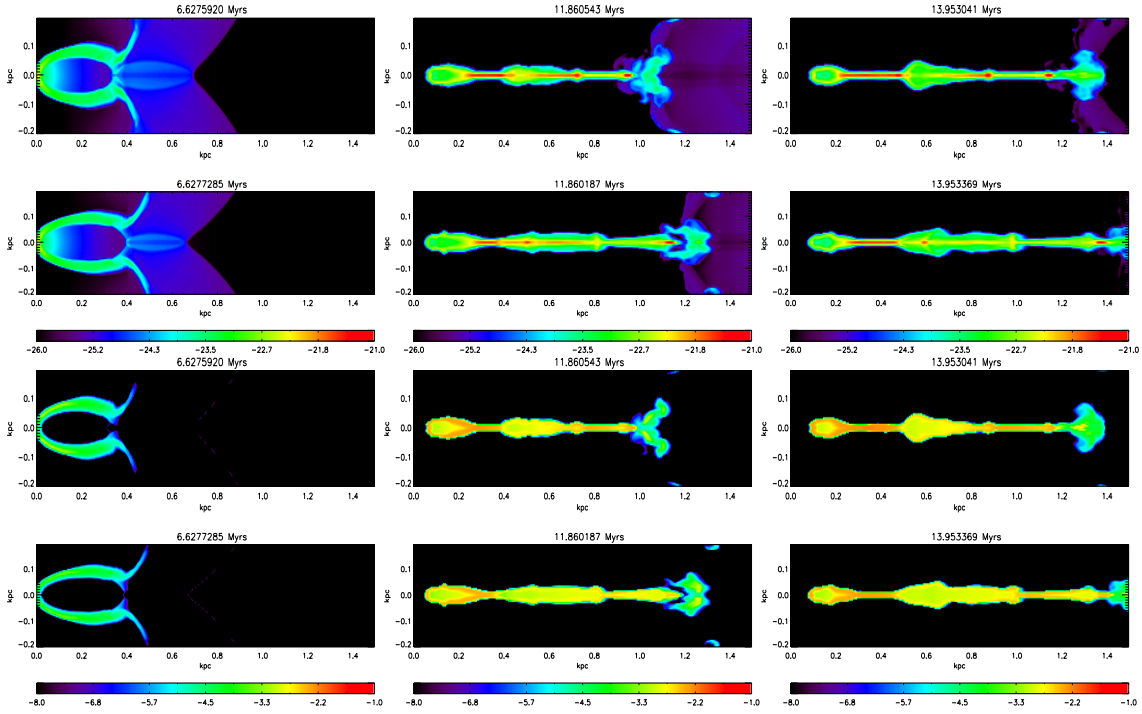

Figure 2.11: Comparison between Case A and Case B cooling and chemistry rates. In this plot time varies across columns, moving from $t = 6.6$ Myrs (left column), to 7.7 Myrs (center column), to 14.0 Myr (right column). The upper two rows show the density in the central slice from the fiducial, case B run (HBN, top row), and the case A run (HAN, second row), with log contours ranging from $\rho = 10^{-26}$ to 10^{-21} g cm^{-3}. The lower two rows show the H_2 mass fraction in the fiducial run (third row) and the Case A run (bottom row). Here the log H_2 mass fraction contours range from $X_{H_2} = 10^{-8}$ to 10^{-1}.

Figure 2.12 shows the comparison between the run including this background (HBY) and the fiducial run HBN. As expected, the abundance of H_2 is reduced in the case with the UV background, peaking at about $\approx 10^{-4}$ instead of $\approx 10^{-2}$ in the run without a background. Interestingly, this difference persists even after a few megayears into the simulation, and the abundance of the HPY run remains stable at about $\approx 10^{-4}$.

However, this value is more than sufficient to cool the gas to the same temperature as in HBN. Even with this lower mass fraction, the cooling time is

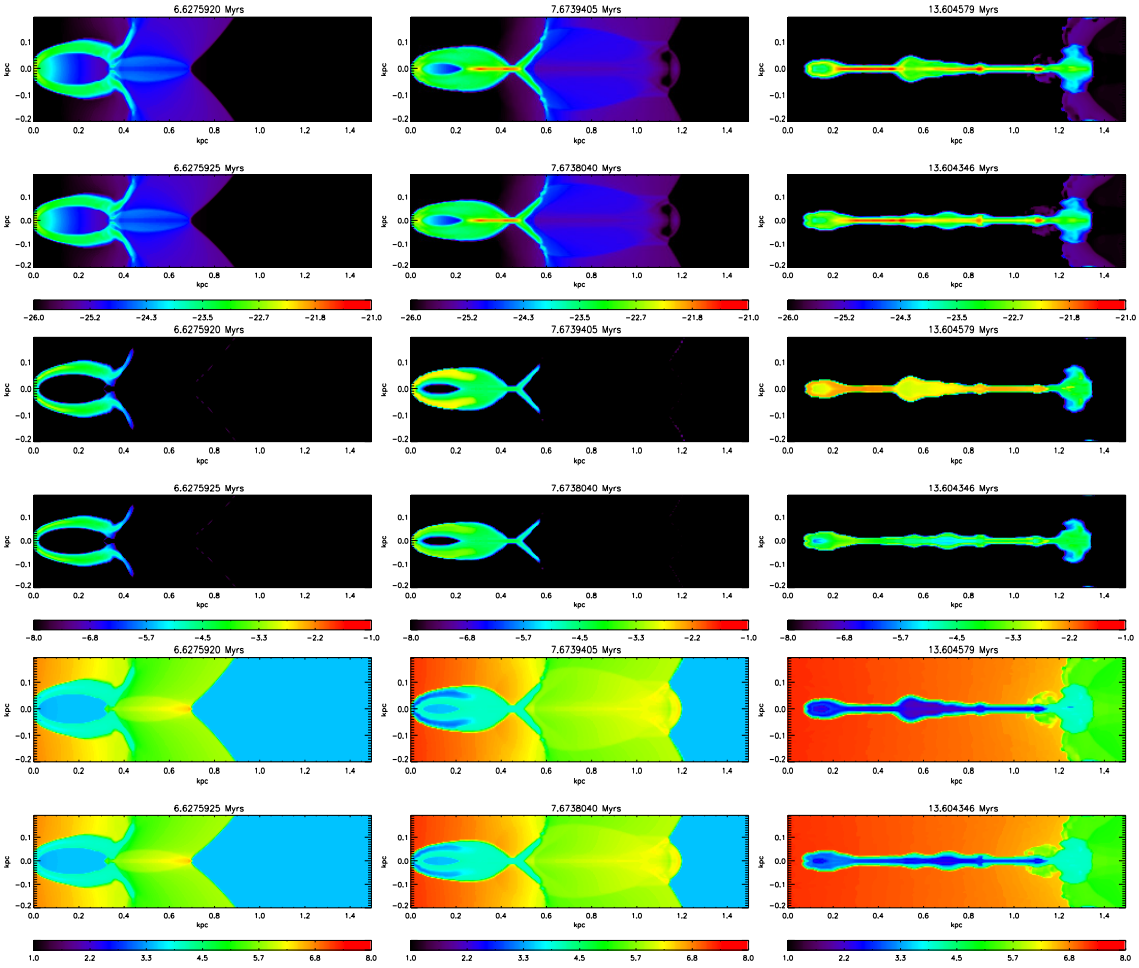

Figure 2.12: Comparison between the fiducial run (HBN) and a run including a dissociating background (HBY) at three important stages of evolution. As in Fig. 2.11, from left to right the columns correspond to $t = 6.6$, 7.7, and 14.0 Myrs. From top to bottom the rows represent log density contours in the fiducial run (Row 1) and the dissociating background run (Row 2), contours of log H_2 mass fraction in run HBN (Row 3) and HBY (Row 4), and contours of log temperature from run HBC (Row 5) and HBY (Row 6). The limits of each panel are the same as Fig 2.7. The addition of a background greatly reduces H_2 but has almost no effect on the dynamics of the interaction.

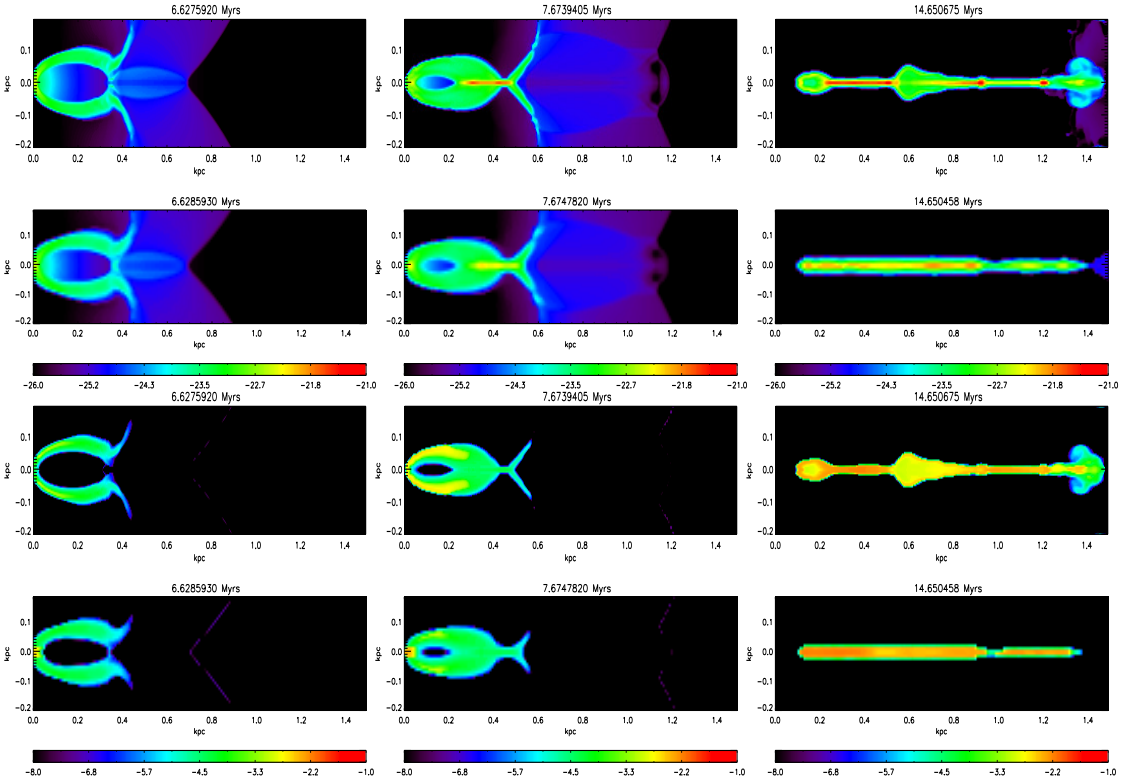

Figure 2.13: Impact of maximum levels of refinement. Row 1 and Row 3 show the density and H_2 contours respectively for the fiducial HBN while Row 2 and Row 4 show contours of density and H_2 for LBN. Contour levels are the same as Fig. 2.11. Time is given at the top of each panel, and proceeds from $t = 6.6$ Myrs (left column) to $t = 7.7$ Myrs (center column) to 14.7 Myrs (right column).

smaller than the dynamical time, and the evolution of the cloud remains essentially unchanged. The cloud collapses and is stretched into the same configuration as found without a background. Dense clouds are again found between 0.2 and 0.4 kpc, at 0.55 kpc, and 0.9 kpc and the density and temperature of each of these clouds is comparable to those found in the fiducial without a background. By neglecting any molecular self-shielding, this represents a worst case scenario for H_2, yet shock minihalo-interactions continue to make compact stellar clusters.

Resolution

Finally, I consider the impact of the maximum refinement level on our results. Figure 2.13 compares the fiducial run with 6 levels of refinement and an effective resolution of 4.55 pc to a lower resolution run (LBN) with 5 maximum levels of refinement and an effective resolution of 9.1 pc. Here density is shown in the upper two rows in each pair while the mass fraction of H_2 is shown in the bottom two rows.

Only a slight dependence on the formation for H_2 is found with resolution. This is most apparent in the second column, corresponding to $t =$ 7.7 Myrs, which shows that the shocks is slightly broadened in the lower resolution case. Since both chemical reactions and cooling go as n^2, this smearing out has the effect of slightly decreasing H_2 formation and cooling in the lower resolution run. However, enough H_2 is produced in both cases for the cloud to collapse efficiently, and evolve in the same manner up until late times, when the difference in H_2 abundance is small.

Furthermore, we also conduct similar resolution studies using Case A recombination, and also modifying chemistry and cooling to account for the presence of a dissociating UV background. Again comparisons between the high-resolution runs (HAN and HBY) with the low resolution runs (LAN and LBY) uncovered only weak differences with resolution. Compact stellar clusters were formed in all cases.

2.3 Conclusions

In this chapter, we have presented the first phase of our investigation of the outcome between a primordial minihalo and galaxy outflow. To properly model this interaction, we have implemented a primordial chemistry network and

associated cooling routines in the AMR hydrodynamics code FLASH. This network traces the formation and evolution of 13 distinct species, including the molecular coolants H_2 and HD. In addition, we have included the effect from a dissociating background and cooling from both atomic and molecular lines.

With these code improvements in place, we simulate the interaction between a cosmological minihalo and galaxy outflow. The outflow fulfills two very important roles during the interaction. First, it shock heats the primordial minihalo gas which catalyzes the formation of molecular coolants. These molecules then provide a mechanism for the gas to cool to below 10^4 K and allows for star formation. Secondly, the shock imparts momentum into the primordial gas which accelerates it to above the escape velocity of the dark matter halo. The end result is a population of massive, dense stellar clusters. In a subsequent chapter we will relate these clusters to present day halo globular clusters.

In the next chapter, we explore effect that metals play in this interaction. we aim to answer two important questions, first how well the metals are mixed in with the primordial minihalo gas, and how much metal-line cooling has on the evolution of the minihalo.

Chapter 3

Effect of Turbulence

In Chapter 2, we developed and verified a 14 species chemical network that traced the evolution of both atomic (H and He) and molecular (H_2 and HD) species, which included all the pertinent cooling rates. To follow this up, we study the evolution and impact of metals in outflow-minihalo interactions. To do this, we added two further packages to our simulations: a turbulence model that tracks the subgrid mixing of enriched and primordial gas and a cooling function that accounts for additional cooling in the presence of metals. Here we describe each of these in turn.

K-L Turbulence Model

Within FLASH we have implemented a buoyancy and shear driven model of turbulence using a two equation K-L model, where K represents the turbulent kinetic energy and L represents the eddy length scale. The model was originally developed and used with great success to describe turbulent fluid flow in inertial confinement fusion (ICF) experiments (Dimonte & Tipton 2006, hereafter DT06; Chiravale 2006), and it reproduces three primary fluid instabilities: the Rayleigh-Taylor (RT) instability, which arises when a low density fluid supports a high density fluid under the influence of gravity or acceleration, the Richtmyer-Meshkov (RM) instability, which occurs when a shock interacts with a fluid of different acoustic impedance such as a density gradient, and the Kelvin-Helmholtz instability, which arises from velocity shear between two fluids, even when they have otherwise identical properties.

In Scannapieco & Brüggen (2008; hereafter SB08), the authors used the original DT06 model to study AGN-driven turbulence in galaxy clusters focusing purely on RT and RM driven turbulence. For our expanded model, we have

added the additional contribution from the KH instability, which is crucial to the problem we are studying. The DT06 model is based on the Navier-Stokes equations expanded to include a turbulent viscosity μ_T and pressure P_T which are dependent on the eddy size L and the turbulent kinetic energy K. To compute these properties we divide the flow into two components; writing velocity, for example, as the sum of mean $\tilde{u}$ and fluctuating u'' components:

$$u \equiv \tilde{u} + u'', \tag{3.1}$$

where $\tilde{u}$ is the mass averaged variable $\tilde{u} \equiv \overline{\rho u}/\bar{\rho}$, $\overline{\rho u''} = 0$, ρ is the mass density, and the overbar represents an ensemble average over many realizations of the flow. This corresponds to an expansion about the mean flow and to first order yields the following evolutionary equations in 3D,

$$\frac{D\bar{\rho}}{Dt} = -\frac{\partial \widetilde{\rho u_i}}{\partial x_i}, \tag{3.2}$$

$$\frac{D\bar{\rho}F_r}{Dt} = \frac{\partial}{\partial x_i}\frac{\mu_T}{N_F}\frac{\partial F_r}{\partial x_i}, \tag{3.3}$$

$$\frac{D\bar{\rho}\tilde{u}_i}{Dt} = -\frac{\partial P}{\partial x_i} - \frac{\partial \tau_{ij}}{\partial x_j}, \tag{3.4}$$

$$\frac{D\bar{\rho}\varepsilon}{Dt} = \frac{\partial}{\partial x_j}\frac{\mu_T}{N_\varepsilon}\frac{\partial \varepsilon}{\partial x_j} - P\frac{\partial \widetilde{u_j}}{\partial x_j} - \tau_{ij}\frac{\partial u_i}{\partial x_i}, \tag{3.5}$$

where $\bar{\rho}$ is the mean density, F_r is the mass fraction of species r, $\widetilde{\rho u_i}$ is the momentum in the i^{th} direction, P is the mean gas pressure, and ε is the internal energy per unit mass which, unlike in DT06 and SB08, includes both the thermal and turbulent kinetic energy components. As discussed in Scannapieo & Brüggen (2010), this formulation allows me to follow the model into the highly supersonic regime in which most of the internal energy is turbulent rather than

thermal. Turbulence affects the mean flow through the turbulent stress tensor τ_{ij} and the turbulent viscosity μ_T which is scaled in the energy equation by $N_\varepsilon = 1$ and in the mass fraction equation by $N_F = 1$. Finally, the Lagrangian time derivative is defined as

$$\frac{D}{Dt} \equiv \frac{\partial}{\partial t} + \widetilde{u_j}\frac{\partial}{\partial x_j}, \tag{3.6}$$

where there is an implied summation over all dimensions.

These equations depend on the evolution of the eddy scale L and the turbulent kinetic energy K. Equations that include the diffusion, production, and compression of these quantities are

$$\frac{D\bar{\rho}L}{Dt} = \frac{\partial}{\partial x_i}\frac{\mu_T}{N_L}\frac{\partial}{\partial x_i}L + \bar{\rho}V + C_C\bar{\rho}L\frac{\partial \widetilde{u_i}}{\partial x_i} \tag{3.7}$$

$$\frac{D\bar{\rho}K}{Dt} = \frac{\partial}{\partial x_j}\frac{\mu_T}{N_\varepsilon}\frac{\partial K}{\partial x_j} - \tau_{ij}\frac{\partial \widetilde{u_i}}{\partial x_j} + S_K. \tag{3.8}$$

In eqn. (3.7) the first term represents the diffusion of the eddy length scale as scaled by the turbulent viscosity μ_T and scale factor $N_L = 0.5$. The second term is the primary production term and is proportional to $V \equiv \sqrt{2K}$ and independent of the flow. The third term is the growth of eddies due to the expansion and compression of the mean flow. Finally, $C_C = 1/3$ is a constant in the model and is determined by mass conservation in eddies as they are compressed. In eqn. (3.8), which parallels eq. (3.5), the first term is the diffusion of turbulent kinetic energy and is scaled by μ_T/N_ε. The second term is the work associated with the turbulent stress which drives the KH instabilities. Finally, the third term is a source term that drives RT and RM instabilities.

Note that we assume that $\mathrm{N}_F \approx \mathrm{N}_\varepsilon$. Pan & Scannapieco (2010) studied the efficiency of mixing over a large range of high Mach number turbulent flows. By comparing the scalar (e.g. mass fraction) dissipation time scale to the time

scale for the total kinetic energy loss, they find that this ratio does not deviate much from one, which validates this choice.

The primary source term for RT and RM instabilities is S_K, which is represented by and defined by DT06,

$$S_K = \bar{\rho} V \left(-C_B A_i \frac{1}{\rho} \frac{\partial P}{\partial x_i} - C_D \frac{V^2}{L} \right), \tag{3.9}$$

where the coefficients $C_B = 0.84$ and $C_D = 1.25$ are fit to turbulence experiments. Physically, turbulent entrainment is described by C_B which reduces any density contrasts, and C_D is a drag coefficient that describes the dissipation of turbulent energy when the average length scale is proportional to L. Likewise, $V \equiv \sqrt{2K}$ is the average turbulent velocity, P is the pressure, ρ is the density , and A_i describes the Atwood number in the i^{th}-direction. This is determined by,

$$A_i = \frac{\bar{\rho}_+ - \bar{\rho}_-}{\bar{\rho}_+ + \bar{\rho}_-} + C_A \frac{L}{\bar{\rho} + L|\partial\bar{\rho}/\partial x_i|} \frac{\partial \bar{\rho}}{\partial x_i}, \tag{3.10}$$

where $C_A = 2$ is a constant of the model, $\bar{\rho}_+$ and $\bar{\rho}_-$ are the densities on the front and rear boundaries of a cell in the i^{th}-direction.

Additionally, and unlike DT06 and SB08, we include the full Reynolds stress tensor, constructed from mean velocities:

$$\tau_{ij} = C_P \delta_{\mathrm{ij}} \bar{\rho} K - \mu_T \, \tau_{\mathrm{KH}} \left(\frac{\partial \widetilde{u}_i}{\partial x_j} + \frac{\partial \widetilde{u}_j}{\partial x_i} - \frac{2}{3} \delta_{\mathrm{ij}} \frac{\partial \widetilde{u}_k}{\partial x_k} \right), \tag{3.11}$$

where δ_{ij} is the Kronecker delta function, μ_T is the turbulent viscosity, τ_{KH} is a function of the local Mach number which is calibrated to produce the correct KH growth rate as discussed below, and C_P is a constant. The first term is the isotropic turbulent pressure and has a trace of $2\bar{\rho}K$ when $C_P = 2/3$. The second term is the deviatoric tensor which has a zero trace (note the implied summation over all dimensions) and is the primary source of shear instabilities.

Table 3.1: List of Model Coefficients

Coefficient	Value	Effect
N_F	1.0	Diffusion of Species
N_ε	1.0	Diffusion of Internal Energy
N_L	0.5	Diffusion of L
C_C	1/3	Compression Effects
C_B	0.84	Buoyancy-driven turbulence
C_D	1.25	Drag term on K
C_A	2.0	Atwood Number
C_P	2/3	Turbulent Pressure
C_μ	1.0	Turbulent viscosity
τ_{KH}	variable	KH growth scaling

Finally, the turbulent viscosity is calculated as.

$$\mu_T = C_\mu \bar{\rho} L \sqrt{2K}, \tag{3.12}$$

where $C_\mu = 1$ is a constant. Table 3.1 summarizes all model coefficients, their values, and their effects.

The numerical implementation of this model is divided into five steps:

1. Update the velocities using the turbulent viscosity in the fourth-order PPM solver before the turbulence package is called during the hydrodynamic step.

2. Calculate the Reynolds stress tensor and update the turbulent kinetic energy, K, as in eqn. (3.8).

3. Use the updated value for K and actualize the diffusive mixing terms in eqns. (3.3), (3.5), (3.7), and (3.8).

4. Compute the contributions from the source terms as:

   a) Calculate $V \equiv \sqrt{2K}$.

b) Add the $\bar{\rho}V$ term to the L equation and use a leapfrog approach to add the source term $(S_K/\rho V)$ to the V equation.

c) Write K back as $K = V^2/2$ a'nd update the turbulent viscosity as in eqn. (3.12).

5. Enforce a minimum time-step from turbulence as $dt \leq (\Delta^2/\mu_T)/6$, where Δ is the minimum between dx, dy and dz in a given cell and μ_T is the turbulent viscosity in that cell. The minimum per block is calculated where a block in FLASH is composed of $nx \times ny \times nz$ cells. Finally the global minimum is calculated across all blocks.

Sub-Grid Turbulence Model Tests
Rayleigh-Taylor Shock Tube Test

To verify the implementation of our model, we reconstruct the RT problem as described in §5 of DT06 (and §3.1 of SB08). Initially a 1 cm region was filled with two $\gamma = 5/3$ fluids with constant density, $\rho_1 = 1.0$ g cm^{-3} in the region from $x = 0.0$ to 0.5 cm and $\rho_2 = 0.9$ g cm^{-3} from$x = 0.5$ to 1.0 cm. A gravitational field acted in the x direction with a constant acceleration of 9.8×10^8 cm s^{-2} or 10^6 times the Earth's gravity. The initial temperature profile was calculated so that both fluids were in hydrostatic equilibrium and so that at x = 0.5 cm the temperature of the lower density fluid was $T_2 = 50$ K and the temperature in the higher density fluid was $T_1 = 45$ K. Finally, to test the mass fraction diffusion, we initialized each side with different generic mass fractions with atomic masses equal to hydrogen.

Despite being described as a 1-dimensional problem, to test our implementation in FLASH we set up a 2-dimensional 50 "block" by 1 "block" region. Each block represented 8×8 simulation cells. Each test was allowed to refine up to a $l_{ref} = 4$ based on density and pressure profiles. This led to an

initial cell size of $1.0/50/8/2^3 = 3.1 \times 10^{-4}$ cm at the interface and a minimum resolution of 2.5×10^{-3} cm.

Although there is an explicit turbulent time step that must be enforced, this implementation works very well with the AMR hydrodynamic time step imposed in FLASH. Initially when the center is fully refined, the hydrodynamic time step is shorter than the one imposed by turbulence. As the turbulent viscosity grows the time steps become comparable, however, because of the diffusion associated with turbulence the density contrast is smoothed. This allows the AMR to derefine these areas, which in turn increases the turbulent time step. Finally the turbulent time step reaches an equilibrium of 1/6 of the hydrodynamic time step at the end of the simulation after the whole volume has reached the lowest refinement level.

As described in DT06, this problem has an analytic solution for the evolution of K and L,

$$K(x,t) \approx K_0(t)\left(1 - \frac{x^2}{h^2(t)}\right), \tag{3.13}$$

$$L(x,t) \approx L_0(t)\sqrt{1 - \frac{x^2}{h^2(t)}}, \tag{3.14}$$

where $h(t)$ is the scale length for the interpenetrating fluid and is defined as,

$$h(t) = \alpha_b A(0) g t^2, \tag{3.15}$$

here $\alpha_b = 0.06$, $A(0)$ is the initial Atwood number $= 0.05$, g is the gravitational acceleration and is set to 9.8×10^8 cms^{-2}, t is time in seconds, $K_0(t) = (dh/dt)^2/2$, and $L_0(t) = h(t)^2/2$. Initially both K and L were set to a small values throughout the simulation except near the interface where I set both K and L to the analytic values at time of 50 μs.

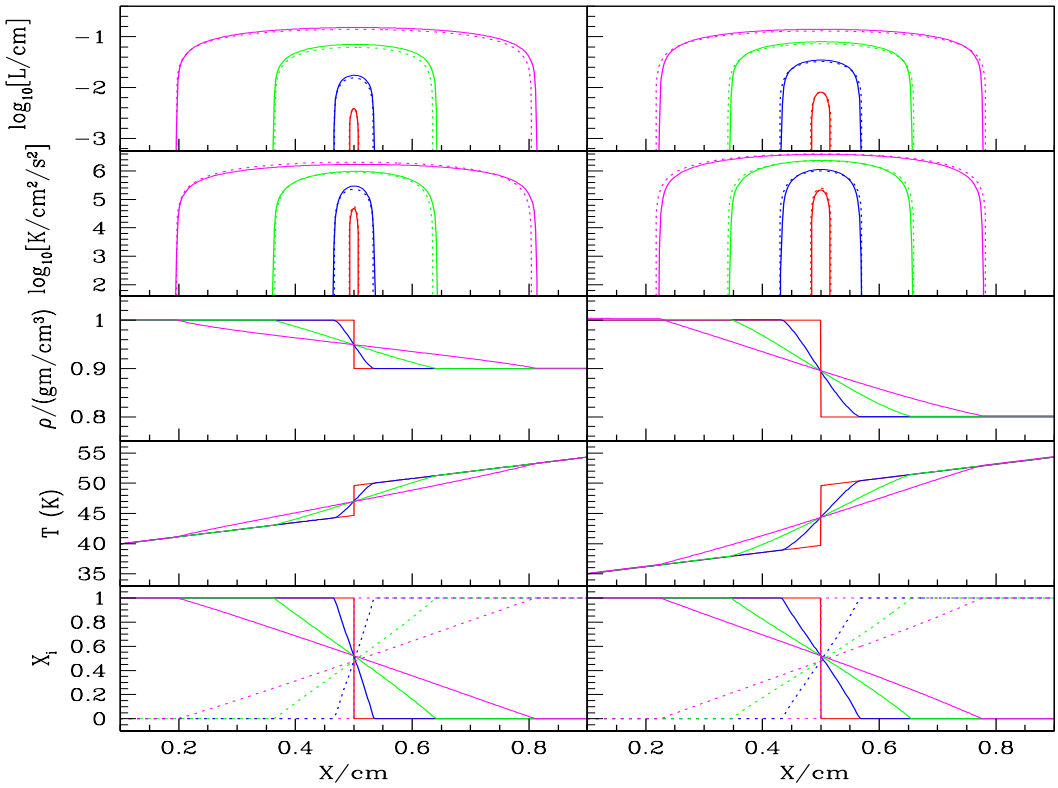

Figure 3.1: Evolution of the shock tube tests. The $\rho_2 = 0.9$ g cm^{-3} case is given in the first column and the $\rho_2 = 0.8$ g cm^{-3} case is given in the second column. *Top left panel*: Profiles of turbulent length scale at 50 (red), 100 (blue), 200 (green), and 300 (magenta) μs. In each case, the dotted lines are the analytic solution and the solid lines are the simulation results. *Second left panel*: Profiles of the kinetic turbulent energy of the same case at the same times as the top panel. *Third left panel*: Density profiles at the same times. *Fourth left panel*: Temperature profiles. *Bottom left panel*: Profiles of species mass fractions. The dotted lines show the mass fraction of the species that was initially on the left side and the solid for the species on the right side. *Right panels:* same as the left except the profiles correspond to 50 (red), 100 (blue), 150 (green), and 200 (magenta) μs respectively. The x-axis and y-axis scales are the same in both columns.

We find that our model matches the expected profiles for K and L at all times and as expected L and K evolve as $\propto t^2$. As K and L quickly increase, the mixing layer also increases which promotes rapid mixing between the two fluids which can be seen in the species profiles. We carried out the same test expect with a sharper density contrast with $\rho_2 = 0.8$ gm/cm^3 and $T_2 = 40$ K. The results are shows in the second column of Fig. 3.1. Again, there is excellent agreement with the expected analytic profiles.

Shear Flow Test

To test the ability of our model to accurately model subsonic shear flow mixing we adapted the shear flow test problem described in §3 of Chiravalle (2006). We begin the problem with an initial velocity shear discontinuity at the origin. Left of the origin we set the y-velocity to 7.8×10^4 cms^{-1} ($\mathrm{M}_1 = 0.46$) while on the right we set the velocity to 1.09×10^5 cms^{-1} ($\mathrm{M}_2 = 0.66$). Pressure and density were held constant across the full domain at 1.72×10^{10} erg cm^{-3} and 1.0 g cm^{-3} respectively. To study mass fraction diffusion, we again initialize each side with different mass scalars with identical properties.

In this case, the shear layer is expected to grow linearly with time as

$$\delta = 0.181\, \Delta v\, t, \tag{3.16}$$

where δ is the width of the mixing layer, Δv is the difference in velocity across the interface, and t is the time (Chiravalle 2006). Unlike the test in Chiravalle (2006), we also add a small initial shear layer of size $\delta_{\mathrm{init}} = 0.1$ cm split equally through the interface with $K = 0.02\ (\Delta v)^2$ and $L = 0.2\ \delta_{\mathrm{init}}$. With this setup, I was able to vary τ_{KH} as a free parameter to approximate the expected growth rate. After 150 μs, the expected width of the shear layer is 0.923 cm, we find that $\tau_{\mathrm{KH}} = 0.20$ reproduces this result, as shown as the top line in Fig. 3.2. This value is close to the one suggested by DT06 ($\tau_{\mathrm{KH}} \approx 0.1$).

Supersonic Shear Test

To extend our model into the supersonic regime, we compare our mixing layer widths to those obtained experimentally by Papamoschou & Roshko (1988), who measured the growth rate of the shear mixing layer as a function of Mach number by forcing two fluids across each other at different relative speeds. Defining the convective Mach number as

$$M_{\rm cl} \equiv \frac{|U_1 - U_2|}{a_1 + a_2}, \tag{3.17}$$

where a_1 and a_2 are the sound speeds and U_1 and U_2 are the fluid velocities in region 1 and 2 respectively, Papamoschou & Roshko (1988) found that as $M_{\rm cl}$ increases, the mixing layer quickly decays asymptotically to 20% of the subsonic mixing layer width. To match this behavior at high Mach numbers we allow the variable $\tau_{\rm KH}$ to vary depending on a 'local' Mach number which we define as

$$M_{\rm l} \equiv \frac{|(\nabla \times \tilde{\mathbf{u}})|L}{c_s}, \tag{3.18}$$

where $|\nabla \times \tilde{\mathbf{u}}|$ is the magnitude of the curl of the mean velocity field, L is the local eddy scale, and c_s is the local sound speed. This local Mach number approximates $M_{\rm cl}$ and we use it to scale $\tau_{\rm KH}$ as

$$\tau_{\rm KH} = \begin{cases} 0.2 & M_{\rm l} \leq 0.3, \\ 0.2 - 0.65(M_{\rm l} - 0.3) & 0.3 \leq M_{\rm l} \leq 0.6, \\ 0.00575 & 0.6 \leq M_{\rm l}. \end{cases} \tag{3.19}$$

To compare the result of this approach to the experimental measurements of δ as a function of time, we adapted the subsonic shear test from §3.2 by changing the velocity on one side of the interface to match the the expected $\rm M_{cl}$. As above, we also initialize a small shear layer of size $\delta_{\rm init} = 0.1$

cm split equally through the interface with $K = 0.02\ (\Delta v)^2$ and $L = 0.2\ \delta_{\rm init}$. K and L are initialized to zero everywhere else. Finally, by changing the initial Δv (and thus $\mathrm{M_{cl}}$) and evolving for the appropriate time we measure the width of the final mixing zone.

Fig. 3.2 shows the results of selecting a variety of values for $\mathrm{M_{cl}}$ and varying $\tau_{\rm KH}$. Each set of points in this figure gives the mixing width measured as the distance between the two points which correspond to 1% and 99% of the velocity difference. Note that this is discretized due to this definition and the spatially discrete (AMR) structure of FLASH. Also in Fig. 3.2 rhe solid lines are the theoretical mixing widths of the form

$$\delta = \delta_0 + 0.181\,\Delta v\,t\,k, \tag{3.20}$$

were δ_0 is the initial mixing width, Δv is the velocity difference between the two fluids, t is time, and k is a constant between 0 and 1.

In this figure the simulation time has been normalized by the evolution time, defined as $0.812\,\mathrm{cm}/\Delta v$, the time required for each case to reach a final mixing width of $\delta = 0.923$ cm if k were equal to 1. If $\tau_{\rm KH}$ is scaled correctly, then when fitting the mixing width using eqn. (3.20) k will equal the expected mixing layer widths divided by the expected width as a function of Mach numbers as given by Papamoschou & Roshko (1988) in their Fig. 16. As Fig. 3.2 shows, our model reproduces the expect linear growth extremely well across a range of Mach numbers. This range is much larger that seen our simulations, which have typical Mach numbers between 0.3-0.7. Table 3.2 summarizes the initial setup parameters for the results in Fig. 3.2 as well as the final mixing widths and values for k.

Table 3.2: Parameters used for the Fig. 3.2. The first 2 columns are the initial velocities on either side of the interface in units of Mach numbers, the 3rd column is the convective Mach number, the 4th column is the evolution time for each model, the 5th column is the final mixing width, and the 6th column is the parameter k as defined in eqn. 3.20.

M_1	M_2	$M_{cl}(\frac{\Delta M}{2})$	τ (μs)	δ(cm)	k
0.46	0.66	0.10	150	0.923	1.0
0.46	1.46	0.50	30	0.48	0.52
0.46	1.96	0.75	20	0.32	0.32
0.46	3.46	1.50	10	0.15	0.16

The growth rate of a shear layer is dependent primarily on the velocity and density ratio on either side of the shear discontinuity. This dependence has been studied by numerous authors (e.g. Brown & Roshko (1974), Slessor *et al.* (2000) and references within) and as shown by Soteriou & Ghoniem (1995) is small and for a given velocity ratio does not alter the growth rate very much.

Radiative Cooling

Above 10^4 K the cooling function is primarily controlled by atomic radiation and, at very high temperatures, bremsstrahlung radiation. These contributions are calculated from a table lookup using values calculated using CLOUDY (Ferland *et al.* 1998). Here we assume Case B recombination and consider only collisional ionization by use of the "coronal equilibrium" command of a metal free gas. Below 10^4 K the cooling is dominated by molecular line cooling and metal-line cooling.

Molecular cooling is described in Chapter 2, but now in addition, we have included metal line radiative cooling in the optically thin limit. To simulate metals in our simulations, we define a generic mass scalar in FLASH, which is advected with any flows. For the cooling rates we use the tabulated results from Weirsma *et al.* (2008), which assume local thermodynamic equilibrium, and in

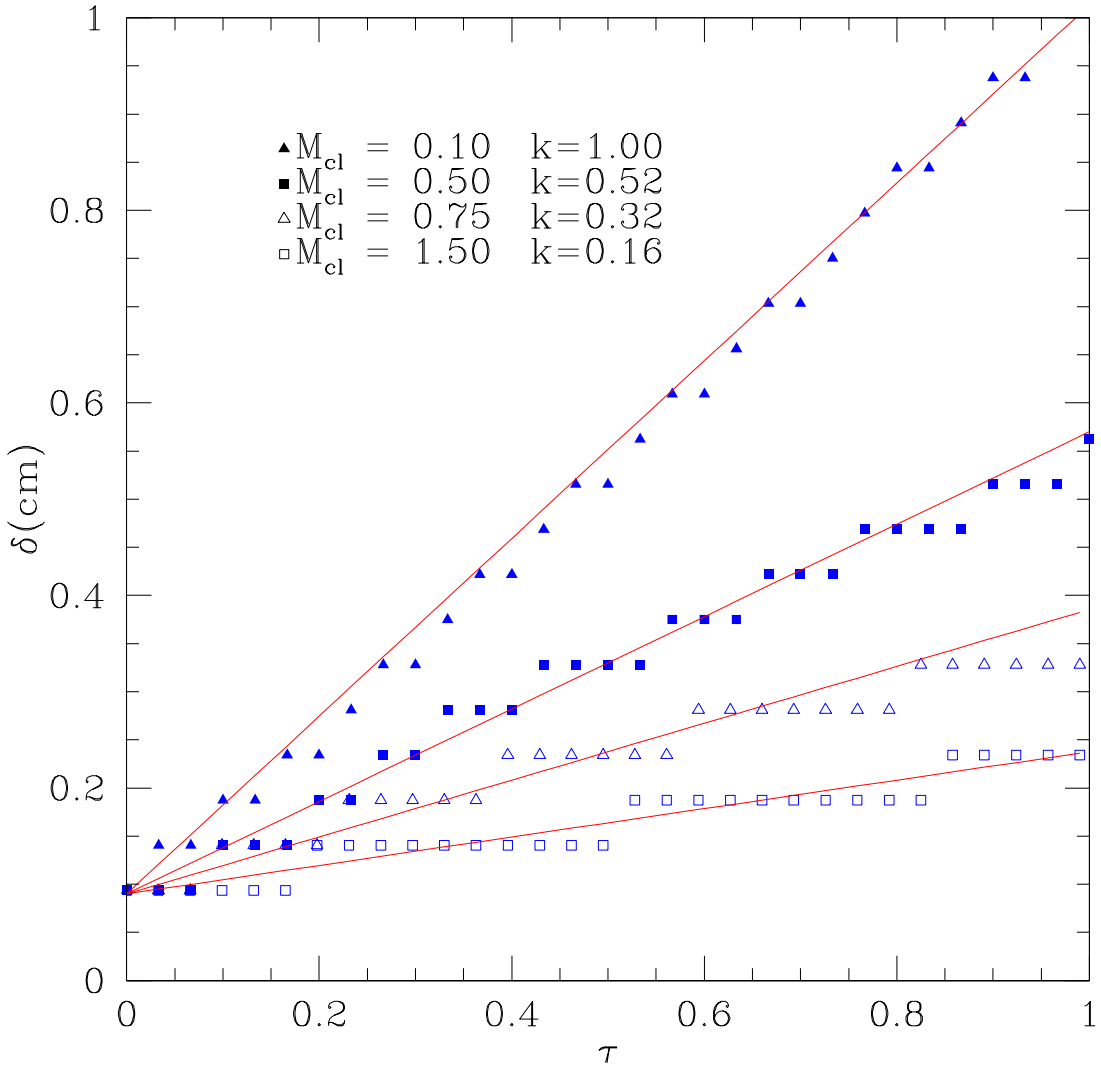

Figure 3.2: Expected growth rate at different Mach numbers. The y-axis is the width of the mixing layer in cm and the x-axis is the normalized evolution time (the simulation time divided by the total evolution time 0.812cm/Δv,). The red lines are the expect mixing widths from the k values given in Papamoscho & Roshko (1988) while the blue points are the measured widths from our model. Table 3.2 summarizes the parameters used for the fits and for the model. The range of Mach numbers studied here is much larger than the range of Mach numbers found in our simulations, which vary between 0.3-0.7.

all cases we use standard solar abundance ratios. The radiative rates are defined over a large temperature range, from 10^2 K through 10^9 K. The specific cooling rate for a given temperature is found using a table lookup from a data file and scaling by the local metallicity.

3.1 Modeling Outflow-Minihalo Interactions

Having described the new physical processes, we return our attention to the model developed in Chapter 2. Again I assume a ΛCDM cosmology with $h = 0.7$, $\Omega_0 = 0.3$, $\Omega_\Lambda = 0.7$, and $\Omega_b = 0.045$ (e.g., Spergel *et al.* 2007), where h is the Hubble constant in units of 100 km s^{-1} Mpc^{-1}, and Ω_0, Ω_Λ, and Ω_b are the total matter, vacuum, and baryonic densities in units of the critical density. The critical density for our choice of h is $\rho_{\rm crit} = 9.2 \times 10^{-30}$ g cm^{-3}.

We begin with a neutral primordial minihalo, which is composed of 24% helium and 76% hydrogen with a total mass of both dark and baryonic matter of $\mathrm{M}_c = 3.0 \times 10^6$ $\mathrm{M}_\odot$. The initial minihalo has a total radial density profile given by Navarro *et al.* (1997):

$$\rho(R) = \frac{\Omega_0 \rho_c}{cx(1+cx)^2} \frac{c^2}{3F(c)} \text{ g cm}^{-3}, \tag{3.21}$$

where c is the halo concentration factor, $x \equiv R/R_{\rm c}$, $R_{\rm c}(= 0.393)$ kpc is the virial radius, $F(t) \equiv \ln(1+t)$ - $\frac{t}{1+t}$, and $\rho_{\rm c} = 6.54 \times 10^{-25}$ g cm^{-3} is the mean cluster density. The baryonic matter is taken to be in hydrostatic equilibrium and follows an isothermal radial profile with a virial temperature of T = 1650 K:

$$\rho_{\rm gas}(R) = \rho_0 e^{-\frac{(v^2_{\rm esc}(0) - v^2_{\rm esc}(R))}{v^2_c}} \text{ g cm}^{-3}, \tag{3.22}$$

where the escape velocity is $v^2_{\rm esc}(xR_{\rm vir}) = 2v^2_c[F(cx) + cx(1+cx)^{-1}][xF(c)]^{-1}$ and $\rho_0 = 2.16 \times 10^{-23}$ g cm^{-3}.

Gravity is treated using the multigrid Poisson solver for self gravity of the gas (Ricker 2008) as well an additional component of gravitational acceleration

due to dark matter. The initial metallicity of the halo and surrounding gas is set to zero, and the initial values of K and L are set to 1% of the total internal energy and one parsec respectively. All other parameters are left at their fiducial values including the background UV radiation field ($J_{21} = 0.0$).

The outflow is approximated by the Sedov-Taylor blast wave solution. We assume that the minihalo is at a distance $R_s = 3.6$ kpc and that the shock has a velocity of $v_s = 225$ km s^{-1}. By the time the shock reaches the minihalo it will have entrained a total mass of $M_{s,total} = 4.4 \times 10^7$ $M_\odot$ with an associated surface density of $\sigma_s = 2.6 \times 10^5$ $M_\odot$ kpc^{-2}. The input energy for this outflow was derived from SNe from the host galaxy, and was taken to be $E = (\epsilon E_{55})$ erg where ϵ is the wind efficiency which is obtained from the fraction of the SNe energy funneled into the outflow and is set at our fiducial value of $\epsilon = 0.3$ and E_{55} is the total SNe energy in units of 10^{55} erg.

We initialized the left boundary with the same initial properties as our previous models. As in the rest of the simulation domain, we set K and L to 1% of the internal energy and one parsec respectively. To determine the initial metallicity of the shock, I followed the analysis from Scannapieco *et al.* (2004). We infer that roughly 2 $M_\odot$ worth of metals are produced per 10^{51} ergs of energy in both Type II and pair instability supernova from Population III stars (Woosley & Weaver 1995; Heger & Woosley 2002). If we assume that half of these metals escape from the host galaxy and are funneled into the outflow, we can expect a total mass of metals of $M_{metal} = 10^4$ E_{55} $M_\odot$. This leads to a metal fraction of the shock of $X_{metal} = M_{metal}/M_{s,total} = 0.12$ $Z_\odot$, which we use as our fiducial value.

Table 3.3: Summary of the simulations.

Name	$l_{\rm ref}$	Resolution (pc)	Turbulence	Metal Cooling
LWT	4	18.22	Y	Y
LNT	4	18.22	N	Y
MWT	5	9.11	Y	Y
MNT	5	9.11	N	Y
HWT	6	4.55	Y	Y
HNT	6	4.55	N	Y
HBN*	6	4.55	N	N

3.2 Results

My simulations were carried out in a rectangular box with an effective volume of 3.2×10^9 pc^3. The y-axis and z-axis were both 1170 pc and ranged from (-585,585) pc. The x-axis was twice as long, 2340 pc, and ranged from (-585,1170) pc. The minihalo was centered at (0,0,0) pc and the shock originated from the left boundary with a velocity along the positive x direction. Both density and pressure were used as the refinement/derefinement variables, and we also force derefinement after 7 Myrs in regions with density less than 3.26×10^{-26} g cm^{-3} outside a central sphere of radius 324 pc centered at (0,0,0) kpc. This had the advantage of derefining unimportant blocks, which was especially important in the runs without subgrid turbulence, as turbulent mixing tends to smooth the density gradients, allowing the AMR to naturally derefine.

A summary of the runs performed are given in Table 3.3. We label them by whether they were high, medium, or low resolution (H, M, or L) and whether they used the subgrid turbulence package (WT or NT). In our new simulations metal cooling was always included, and to asses the impact of this cooling we also include the fiducial run from Chapter 2 (HBN), noted by the asterisk, which is used to compare with run HNT.

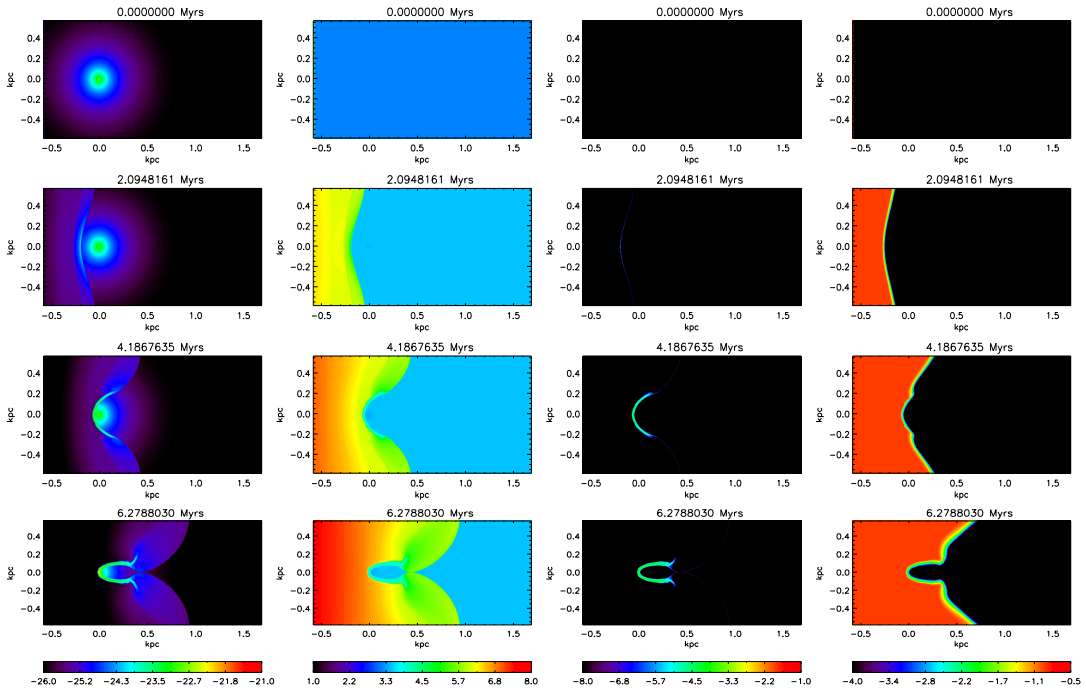

Figure 3.3: Evolution of run HWT from $t = 0$ to the time at which the shock completely surrounds the cloud. Each image shows an x-y slice through the center (z=0) of our simulation volume. The first column shows logarithmic density contours from 10^{-26} g cm^{-3} to 10^{-21} g cm^{-3}, which correspond to number densities between n $\approx 10^{-2}$ cm^{-3} and 10^{2} cm^{-3}. The second column shows the logarithmic temperature contours from 10 K to 10^{8} K, the third column shows the logarithmic H_2 mass fraction contours between $X_{H_2} = 10^{-8}$ to 10^{-1}, and finally the fourth column shows the logarithmic metal mass fraction contours between Z = 10^{-4} Z$_\odot$ to $10^{-0.5}$ Z$_\odot$.

Hydrodynamic Evolution

Figures 3.3 and 3.4 show the evolution of the minihalo from initial setup through the shock interaction and to the final collapse of the cloud, focusing on several important stages of evolution throughout these figures. The first row in Fig. 3.3 shows the initial minihalo. Because the gas consists of neutral hydrogen and helium, it is unable to cool on its own. Instead it remains in hydrostatic

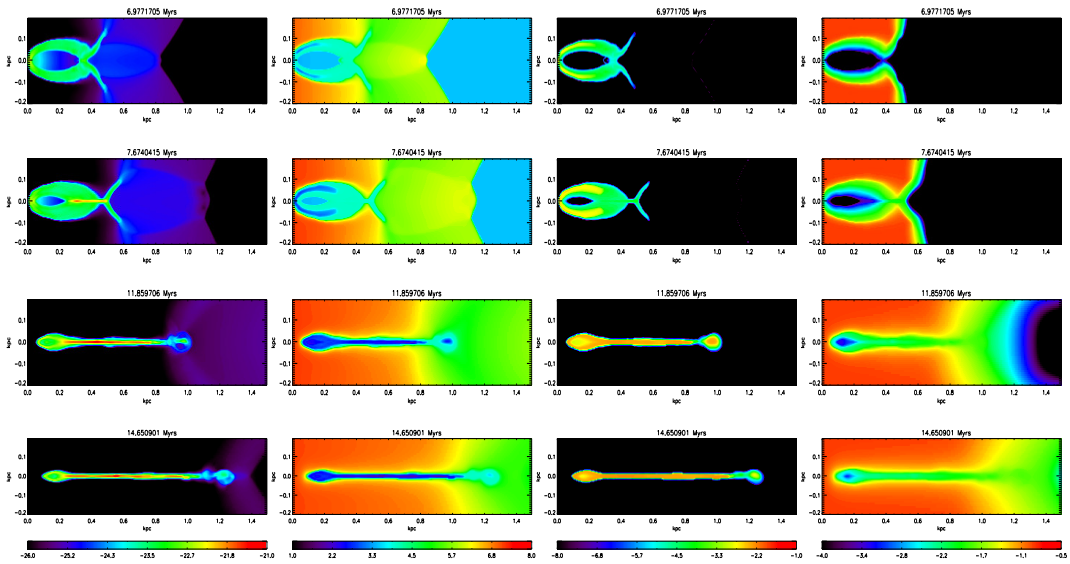

Figure 3.4: Evolution of run HWT from the time at which the shocks meet at the back of the cloud ($t = 6.797$ Myrs), to the time at which the reverse shock passes through the cloud ($t = 7.67$ Myrs), to the collapse of the cloud ($t = 11.9$ Myrs), and the end of the simulation ($t = 14.65$ Myrs). Columns and rows are the same as in Fig. 3.3. For this figure I have cropped the individual images along the x and y axes for clarity. Until t= 7.67 Myrs the molecule and metal distributions closely follow each other, but at later times molecule formation is enhanced near the core of the cloud due to the reverse shock, which does not carry metals.

balance with a free fall time of

$$t_{\rm ff} = \sqrt{\frac{3\pi}{32G\rho}} \approx 100 \text{ Myrs}, \tag{3.23}$$

that is roughly equal to the sound crossing time.

As the shock interacts with the minihalo, it begins to heat and ionize the neutral gas. The ionized gas then recombines and starts to catalyze the formation of H_2 and HD. This results in a 'hollow' distribution of molecules that is concentrated in the interacting regions at the front and sides of the cloud. The metal distribution closely follows this molecular distribution, because the shock is able to move faster in the less dense portions of the cloud. The shock fully

envelopes the minihalo in a 'cloud-crossing' time defined by Klein *et al.* (1994) as

$$t_{\rm cc} = \frac{2R_c}{v_s} \approx 4.6 \text{ Myrs}, \tag{3.24}$$

which occurs at about $t \approx 6.5$ Myrs after the beginning of our simulations and is shown in the last row of Fig. 3.3.

The time scale for H_2 formation is given by Glover *et al.* (2008) as

$$t_{\rm H_2} = \frac{X_{\rm H_2}}{k_1 X_{\rm e} n}, \tag{3.25}$$

where X_{H_2} and X_e are the mass fractions of H_2 and electrons respectively, n is the number density, and k_1 is the reaction rate for the formation of H^- a key reactant in formation of H_2. When the shock first interacts with the cloud, this time scale is very short since $n \approx 1$ cm^{-3} and the fraction of electrons (X_e) is relatively large. However the cloud quickly reaches an abundance of $X_{H_2} \approx 10^{-4}$ as shown in the third column of Fig. 3.3. This fraction continues to grow as the cloud is surrounded, but does so at a much slower rate as X_{H_2} increases and X_e decreases. Again, the distributions of molecules and metals closely track each other.

At ≈ 7 Myrs, after the shock meets on the back of the cloud, it creates a reverse shock, which begins to catalyze molecule formation, as shown in the top row in Fig. 3.4. It is here that the metal and molecule distribution diverge as the metals have not had the time to diffuse in the interior of the cloud. We define a turbulent mixing time scale as

$$t_{\rm mix} = \frac{d^2}{(\mu_T/\bar{\rho})} \text{ s}, \tag{3.26}$$

where d is the distance over which the metals are diffused, μ_T is the turbulent viscosity, and $\bar{\rho}$ the local density. By looking at the third and fourth columns of Fig. 3.4 and comparing the distributions of H_2 and metals at t = 7.67 Myrs, it is

obvious that metals are deficient along the x-axis at $y \sim 0.3$ kpc. If we approximate the distance that metals need to diffuse through as $d \approx 10$ pc and estimate the turbulent viscosity around the collapsing cloud to its post-shock value $\mu_T/\bar{\rho} \approx 25$ pc^2 Myr^{-1} then the mixing time scale is ≈ 4 Myrs. Thus at $\approx 7 + 4 = 11$ Myrs, the distributions of molecules (shown by H_2) and metals once again follow each other, as can be seen in the third row of Fig. 3.4.

The fourth row of Fig. 3.4 shows the final state of the cloud. Most of the material is found in a small dense ribbon that is stretched along the x-axis and extends many times the initial virial radius away from the center of the dark matter halo. This material is now much colder than it started with typical temperature around 100 K. The H_2 mass fraction abundance of this ribbon is around $10^{-2.2}$, and it has a metallicity of about 10^{-2} $Z_\odot$.

Fig. 3.5 shows a 3D rendered density plot at several important points in the interaction. The top left panel shows the initial $t = 0$ distribution with the shock and minihalo clearly seen. A $t = 6.3$ Myrs, the shock starts to compress the minihalo and the initial collapse of the minihalo begins. The start of the final ribbon stage occurs at at $t = 9.5$ Myrs as the cloud continues to collapse. At the final time of $t = 14.6$ Myrs, the minihalo gas has been compressed, enriched, and cooled into a ribbon along the x-axis that contains a dense series knots. It is here that vigorous star formation is expected to occur.

Model Dependencies

Effect of Turbulence

Turbulence has two primary effects in our simulations: the diffusion of metals from the shock into the minihalo and the smoothing of sharp density contrasts. Fig. 3.6 compares the difference between runs with (HWT) and without (HNT) our subgrid model for turbulence. As expected many of the sharp density

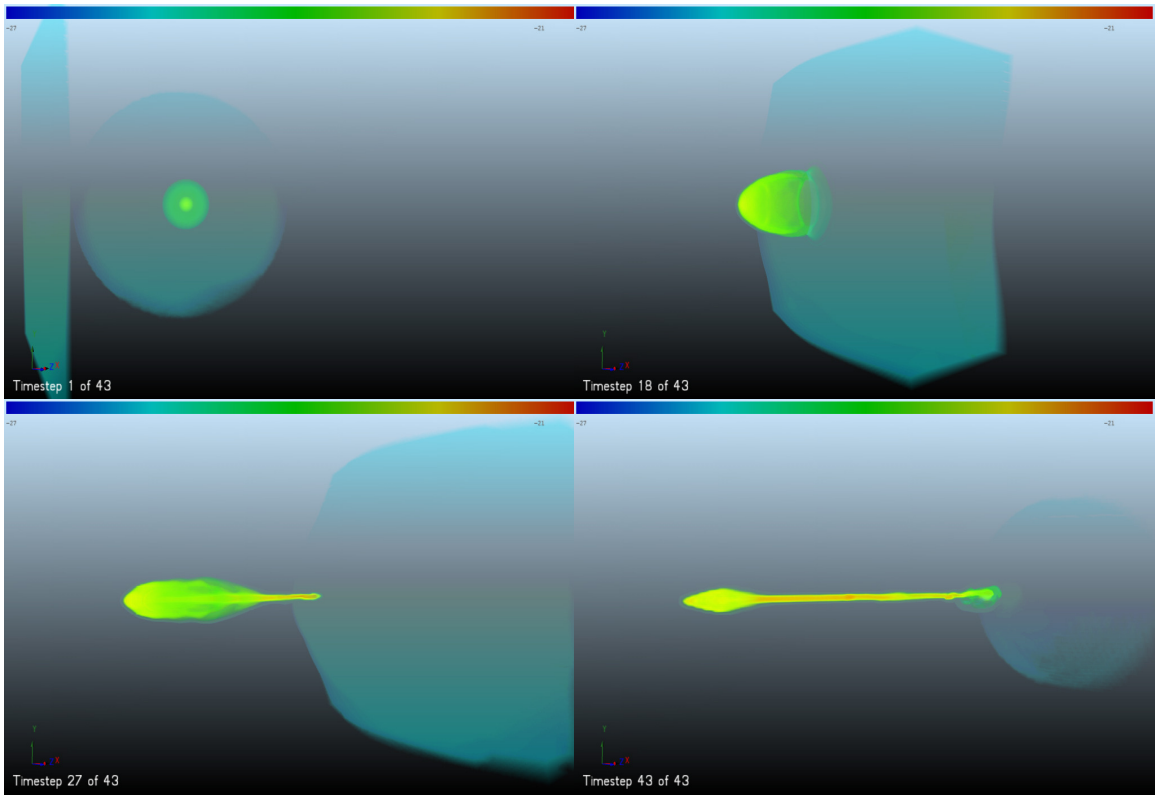

Figure 3.5: Three-dimensional rendering of run HWT at a variety of important stages of evolution. The colors show the logarithmic density contours between 10^{-27} g cm^{-3} and 10^{-21} g cm^{-3}. *Top left:* the ($t = 0.0$ Myrs) initial setup of the simulation with the minihalo and shock visible. *Top right:* the state of the simulation at $t = 6.3$ Myrs, as the shock almost completely surrounds the minihalo. *Bottom left:* the interaction at $t = 9.5$ Myrs, after the shock has passed through the minihalo. Here the cloud has started to collapse and some of the dense knots have started to form. *Bottom right:* the final state of the cloud at $t = 14.6$ Myrs, when we end the simulation. The ribbon of dense material is clearly seen.

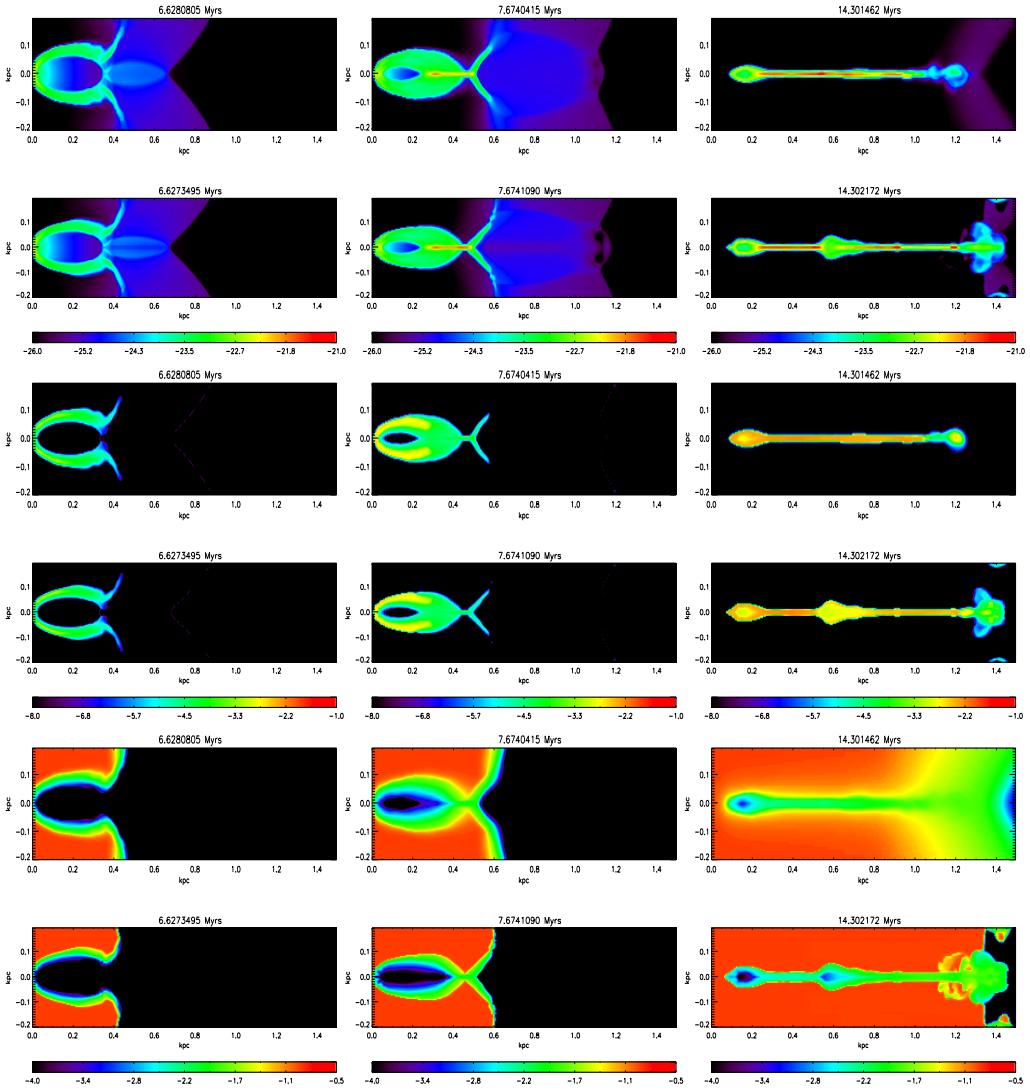

Figure 3.6: Late time comparison between a run with subgrid turbulence (HWT) and a run without it (HNT). Each column represents a different snapshot in time. The top two rows shows logarithmic density contours from 10^{-26} to 10^{-21} g cm^{-3}. Rows 3 and 4 show the logarithmic contours of H_2 mass fraction from 10^{-8} to 10^{-1}. Finally, Rows 5-6 show the contours of metallicity in units of solar metallicity between $10^{-4.0}$ to $10^{-0.5}$ $Z_\odot$. In each set of rows the model with subgrid turbulence (HWT) is on top of the model without it (HNT). Each image is a slice through the center of the domain along the z-axis.

features found in the model without turbulence are diffused away in the model with subgrid turbulence. This is seen in the late-time panels in Rows 1 and 2 in Fig. 3.6 where there was a prominent lower density feature in HNT (at $x \approx 0.65$ kpc) that is not seen at all in HWT. Also absent are the smaller density features at the far end of the simulation domain along the x-axis. Although, in both cases the general result is the same: much of the mass has formed into a dense ribbon along the x-axis.

The most striking difference between the two simulations is the metal distribution. HWT shows a very uniform metal abundance in the final cloud. Almost every portion has a final abundance of $Z \approx 10^{-2}$ $Z_{\odot}$ except for a low density region near the initial center of the cloud. HNT however shows a much more uneven distribution with two regions of low metallicity; one at 0.15 kpc and the other at 0.6 kpc. However, it is important to note that in both cases (HWT and HNT) the densest regions in both models have essentially the same final metal abundance, and thus the spread in metal distribution in the stars that are formed would be small with or without the inclusion of subgrid turbulence.

Effect of Metal-Line Cooling

At temperatures below $T \approx 10^4$ K the primary coolants are molecules and low-energy metal-lines. Therefore the total cooling is expected to be strongly dependent on differences between metal and molecule abundances. Figure 3.7 shows the difference between a fiducial model with (HNT) and without (HBN) metal cooling, where HBN is taken from Chapter 2. There is little difference between these runs aside from slight changes in the positions of small structures. In both cases the same dense knots are found in essentially the same places. Furthermore, the abundances of molecular coolants are essentially identical and are not affected by the inclusion of metals. This suggests that metal cooling is

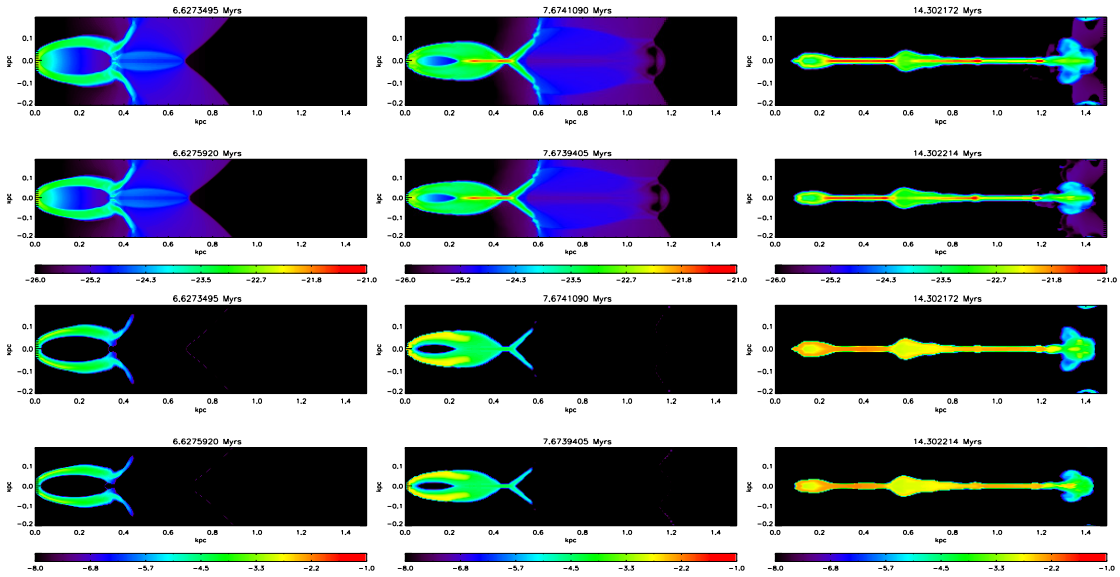

Figure 3.7: Comparison between a run with metal cooling (HNT) and a run without it (HBN). Rows 1 and 2 show the logarithmic contours of density for HNT and HBN while Rows 3 and 4 show the logarithmic contours of H_2 mass fraction. Apart from the slight differences in the positions of similar features there is very little difference between the runs.

not as important as molecular cooling, because otherwise the abundance of molecules in run HNT would be lower than that in run HBN due to the temperature dependence in the molecule formation rates.

The time scale for H_2 cooling can be estimated as

$$\tau_{\mathrm{H}_2} = \frac{1.5nkT}{n_e n_{\mathrm{H}_2} \Lambda(T)_{\mathrm{H,H}_2}}, \tag{3.27}$$

where n is the total number density, k is Boltzmann's constant, T is the temperature, n_e and n_{H_2} are the number densities of electrons and H_2 respectively, and $\Lambda(T)_{\mathrm{H,H}_2}$ is the cooling rate as a function of temperature. Similarly for metal cooling the time scale is

$$\tau_{\mathrm{M}} = \frac{1.5nkT}{n_e n_H \Lambda(T)_{\mathrm{M}} \frac{\mathrm{Z}}{\mathrm{Z}_\odot}} \text{ s}, \tag{3.28}$$

where n_e and n_H are the number densities for electron and hydrogen and $\Lambda(T)_M$ is the cooling rate for metals. The ratio of these time scales is then

$$\frac{\tau_{\rm H_2}}{\tau_M} = \frac{X_e}{X_{\rm H_2}} \frac{A_{\rm H_2}}{A_e} \frac{\Lambda(T)_{\rm M}}{\Lambda(T)_{\rm H,H_2}} \frac{\rm Z}{\rm Z_\odot}, \tag{3.29}$$

where the number densities have been replaced using $X_i = n_i A_i / \rho N_A$. To get an idea of the relative importance of each cooling method, we take representative values for these variables at $t = 7.67$ Myrs, an important point in the evolution of the cloud as it begins to collapse. We find that $\tau_{\rm H_2}/\tau_{\rm M} \sim 10^{-2}$ which means that at this moment molecular line cooling is more important than metal line cooling. Overall, the inclusion of meal line cooling does not make a significant difference in the final state of the cloud.

Effect of Resolution

Finally, we study the impact of resolution on our results. Fig. 3.8 shows the result of our models over a range of maximum resolution levels. The left two columns show the results for models with turbulence while the right two columns show the results without turbulence. Generally, the outcome is independent of resolution. In the case of density the higher the resolution the smaller and more dense the final cloud becomes. However, the structure of the cloud is the same: it has been stretched into a ribbon and moved out of the dark matter halo. Furthermore, the metallicity distribution is almost indistinguishable between the runs with different resolution levels. For each choice of resolution level the final cloud is enriched to $\approx 10^{-2} Z/Z_\odot$, both for runs with and without subgrid turbulence.

Not shown is the difference in molecular abundances. Here there is a resolution dependence on the formation time scale for molecular coolants, as discussed in Chapter 2. However, the amount formed is always sufficient to cool

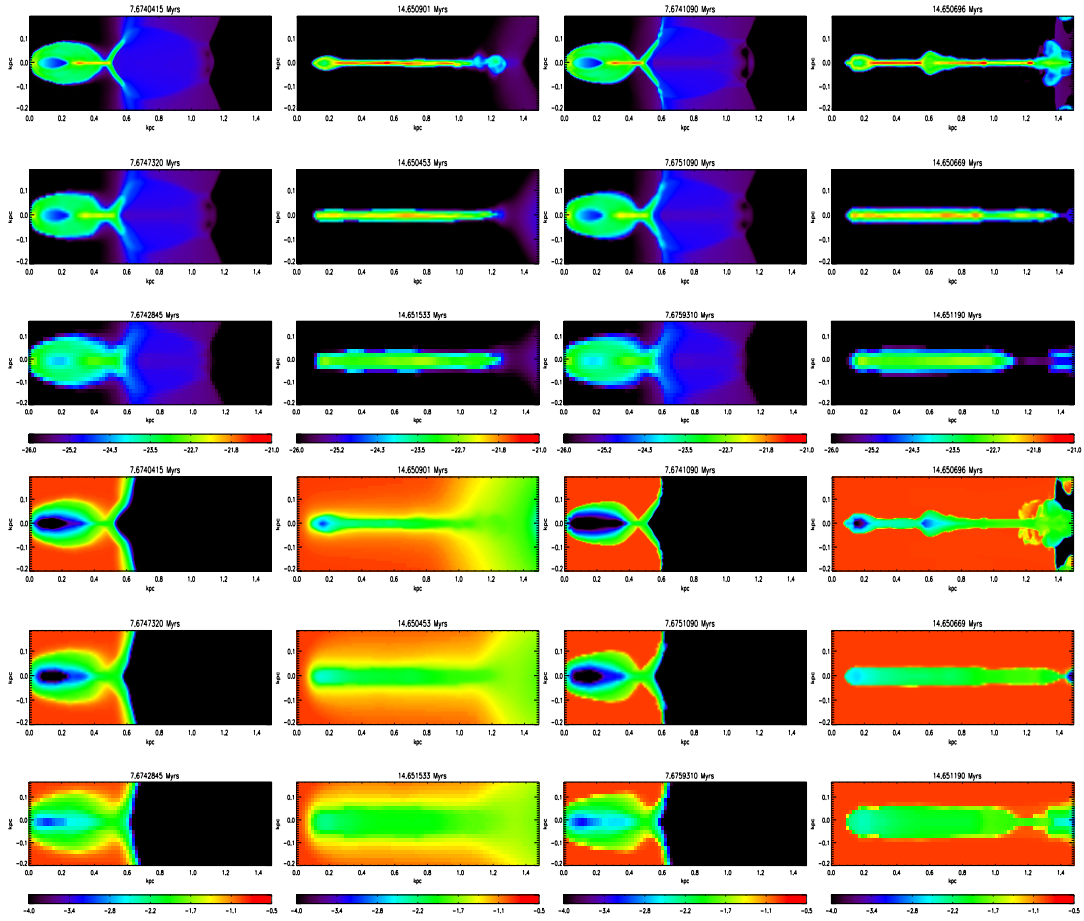

Figure 3.8: The impact of maximum resolution on our runs with (left two columns) and without (right two columns) subgrid turbulence. The top three rows show the logarithmic density contours at t = 7.67 Myrs and t = 14.65 Myrs and the bottom three rows show the logarithmic metallicity contours in units of solar metallicity. Rows 1 and 4 show the respective contours at the highest resolution with $l_{\max} = 6$ (runs HWT and HNT), Rows 2 and 5 at $l_{\max} = 5$ (runs MWT and MNT), and Rows 3 and 6 at $l_{\max} = 4$ (runs LWT and LNT).

the cloud enough to produce the same final outcome. The final abundances are nearly identical at each refinement level except at the lowest resolution, which is different only outside of the dense regions in the final ribbon. Aside from features that do not affect the final distribution of star-forming gas, our results are independent of resolution from $l_{\max} = 4$ to $l_{\max} = 6$.

Stellar Clusters

The final distribution of the dense clumps evolves over 100s of Myrs, a much longer time scale than the shock-minihalo interaction itself. To evolve our simulation over such a long time scale, we adopt the simple one-dimensional procedure described in Chapter 2. Here we subdivide the x-axis into 100 evenly spaced bins from $x = 0$ kpc to $x = 1.4$ kpc. The mass for each bin is calculated by summing up the gas density from the simulation in a cylindrical volume with a radius of 24 pc and length of the bin. We also calculate the velocity of each new bin by summing together the momentum from each cell that goes into it and dividing by the total mass.

This distribution is then evolved using a simple numerical model in which we assume all motion is along the x-axis and that pressure is not important at late times. The acceleration of each point is calculated by adding together the gravitational acceleration from all other particles as well as the gravitational acceleration from the dark matter halo. A leapfrog method is used to calculate the updated position and velocity from the calculated acceleration and updated velocity respectively. Finally, if a bin is evolved past the one in front of it, we merge these two by summing their mass and using conservation of momentum to compute its velocity.

The model is evolved for 200 Myrs past the end of the simulation, and the results are shown in Fig. 3.9 for runs HWT and MWT. As the gas continues

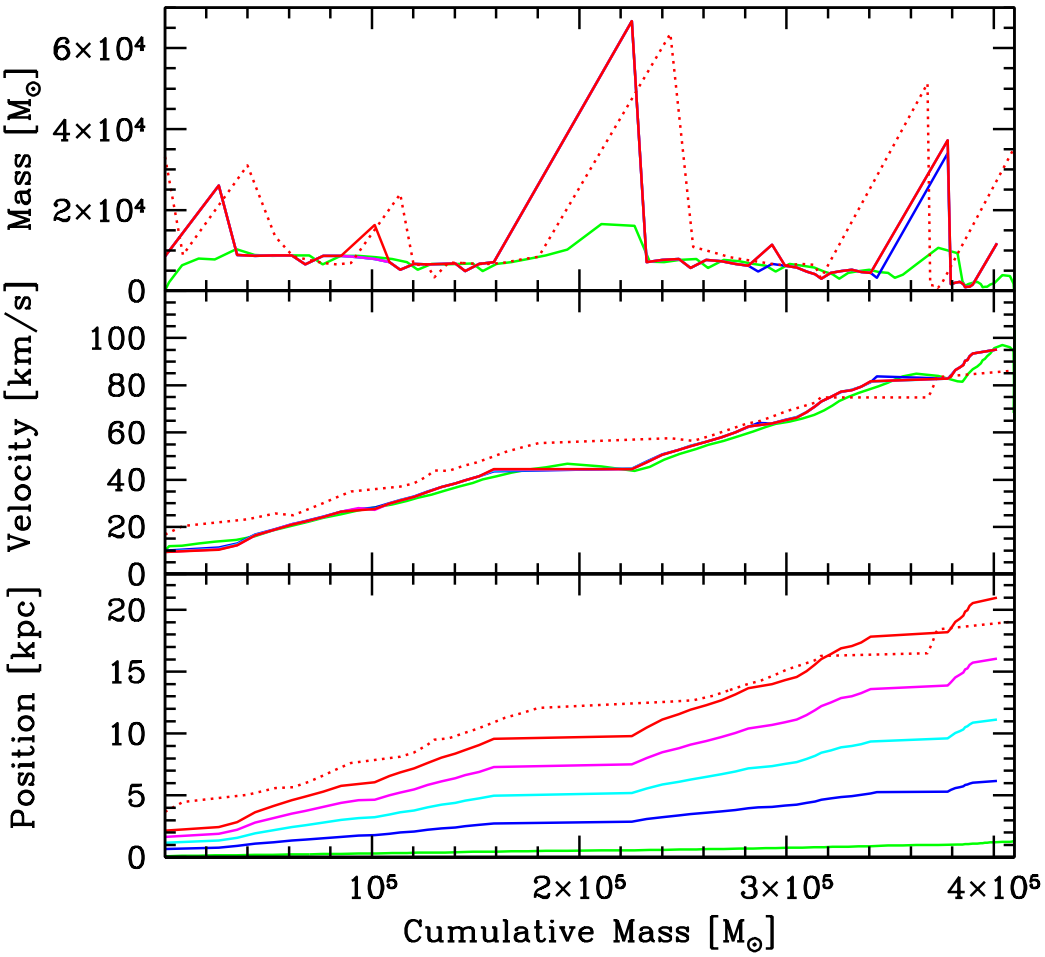

Figure 3.9: Long-term evolution of the distribution of particles after the end of the FLASH simulations. The x-axis gives the cumulative mass in units of a solar mass. The top panel shows the mass of each particle, the middle panel shows the velocity of each particle in units of kilometers per second, and the bottom panel shows the position of each particle in units of kpc. The solid lines are taken from run HWT, and the green line shows the initial profile at $t_f = 14.65$ Myrs, the blue line shows the profile at 50 Myrs later, cyan shows the profile at $t_f + 100$ Myrs, magenta shows the profile at $t_f + 150$ Myrs, and the red line shows the t_f+200 Myrs. By $t_f + 50$ Myrs most of the merging has finished and the largest clumps have formed. The dotted red line shows the $t_f + 200$ Myrs distribution for run MWT and illustrates the difference between the same model at different resolutions. Although some minor differences are present, the same conclusions can be drawn from both runs.

to move outward the particles begin to attract each other and merge. By 50 Myrs after the FLASH simulation, most of the particles have merged and the motion of the remaining particles is purely ballistic. This can be seen in the top and middle panels of Fig. 3.9 as the lines begin to overlap each other.

At the final time of 200 Myrs after the end of the simulation, we can identify one primary clump with a mass over 6.0×10^4 $M_\odot$ with two smaller clumps with masses of 4.0×10^4 $M_\odot$ and 2.5×10^4 $M_\odot$ respectively. The two largest masses are far outside the dark matter halo, and are no longer bound to it.

Comparing the solid (HWT) and dotted red line (MWT) we conclude that regardless of the resolution level the same general conclusions hold. There are some differences between the two resolution levels, primarily in the speed and position of the final clumps formed, but these are minor. In each case a nearly identical distribution of stellar clusters is formed: one large cluster with a few smaller neighbors.

3.3 Conclusion

In this chapter, we have introduced the effect of metals on the interaction between a cosmological minihalo and a galaxy outflow. Of great importance is the extent to which the metals are mixed into the primordial gas. To model this process, we have introduced and tested a sub-grid turbulence model that allows for the mixing of metals and chemical species. In addition, metals provide the gas with an additional cooling pathway and I have updated our cooling functions to account for this new path.

Once these developments were in place, we once again simulated the minihalo/galaxy outflow interaction. We find uniform metal abundances throughout the minihalo gas, suggesting that the turbulent mixing processes are

incredibly efficient. These simulations also reconfirm the results from Chapter. 2. The minihalo gas is transformed into a thin ribbon of material stretching away from the dark matter halo. Several small, dense stellar clusters are found embedded in this ribbon. Finally, each of these clusters has been enriched with metals to a uniform level of $\sim 10^{-2}$ $Z/Z_{\odot}$.

In the next and final chapter on the minihalo/galaxy outflow interaction, we look at the robustness of our results by performing a parameter study on the model parameters. We also look at the observability of these clusters.

Chapter 4

Parameter Study and Observability

In the previous chapters, we have introduced models for different physical processes and have studied their impact on the minihalo-outflow interaction. However, a proper assessment of these outcomes is not possible without understanding how robust the mechanism is to the many likely variations in the properties of high-redshift minihalos and galaxy outflows. Thus, here we turn out attention to the range of interactions that lead to the formation of compact stellar clusters, carrying out a detailed parameter study in which we vary a wide range of properties, including minihalo mass, minihalo formation redshift, outflow energy, outflow redshift, distance, concentration, and spin. With these results we are able to asses in detail the viability of this mechanism in producing compact stellar clusters, as well as make a series of high-redshift predictions to be verified with the next generation of telescopes.

4.1 Model Framework

Numerical Methods

We have implemented a version of the non-equilibrium chemistry network from Glover & Abel (2008). This tracks the full set of two-body reactions that determine the evolution of three atomic hydrogen species (H, H^+, and H^-), three atomic helium species (He, He^+, and He^{++}), three atomic deuterium species (D, D^+, and D^-), two states of molecular hydrogen (H_2 and H_2^+), two states of hydrogen deuteride (HD and HD^+), and electrons (e^-). However, we have neglected the contribution from three-body reactions, since they only become important at densities of $n > 10^8$ cm^{-3} (*e.g.* Palla *et al.* 1983), and neglected the contribution from reactions concerning molecular deuterium (D_2), because the cooling from D_2 and D_2^+ is negligible (Glover *et al.* 2008). While we

included UV dissociation rates from Glover & Savin (2009) to capture the effect of a dissociating background, we discovered that for all reasonable choices of background intensity, they did not effect the evolution of these interactions significantly (Chapter 2). Thus we did not include a dissociating background in the present study. Further details of this implementation and the impact of the UV background are given in Chapter 2.

Secondly, we have implemented molecular and atomic cooling rates. At temperatures below 10^4 K cooling is dominated by both molecular line transitions from H_2 and HD and metal line transitions. We have implemented the cooling rates from Glover & Abel (2008) for the collisional excitation between H_2 and a variety of atomic species as well as the Lipovka *et al.* (2005) rate between HD and H. Above 10^4 K, primordial cooling is dominated by atomic hydrogen and helium, whose cooling rates are calculated using CLOUDY (Ferland *et al.* 1998) assuming Case B recombination. The metal-line cooling function is taken from Wiersma *et al.* (2009) via a table lookup, assuming solar abundances ratios, scaled by the local metal abundance.

Finally, we have implemented a buoyancy and shear driven model of turbulence that extends the two equation $K - L$ model of Dimonte & Tipton (2006; see also Chiravalle 2006), where K represents the turbulent kinetic energy and L is the eddy length scale. This model reproduces the effect of three primary instabilities: the Rayleigh-Taylor instability that arises when a low density fluid supports a high density fluid under an acceleration, the Richtmyer-Meshkov instability, which appears when a shock interacts with a fluid with a different impedance (such as a density gradient), and the Kelvin-Helmholtz instability, which occurs between two fluids that shear in a direction perpendicular to their interface. This model also includes diffusion

terms for both the molecular species and metal abundances, which allows for metal mixing. Further details of this package are given in Chapter 3.

As in Chapter 2 and Chapter 3, we assume a standard ΛCDM cosmology with $h = 0.7$, $\Omega_0 = 0.3$, $\Omega_\Lambda = 0.7$, and $\Omega_b = 0.045$ (*e.g.* Spergel *et al.* 2007), where h is the Hubble constant with units of 100 km s^{-1} Mpc^{-1}, Ω_0, Ω_Λ, Ω_b are the total matter, vacuum, and baryonic matter densities, in units of the critical density. With our choice of h, the critical density is $\rho_{\rm crit} = 9.2 \times 10^{-30}$ g cm^{-3}.

Minihalo

In all runs the minihalo was comprised of a dark matter halo and a metal-free, neutral atomic cloud made up of 76% hydrogen and 24% helium by mass. The total mass of the minihalo was defined as $\mathrm{M}_c = \mathrm{M}_6 \times 10^6$ $\mathrm{M}_\odot$, and we assume that the dark matter and gas have collapsed by a redshift z_c at which time the object had a mean overdensity of $\Delta = 178$ (e.g., Eke *et al.* 1998). This leads to a mean density of $\rho_c = \Delta\ \Omega_0\ (1 + z_c)^3\ \rho_{\rm crit}$ in the cloud. With these choices the virial radius of the cloud is

$$R_c = 0.3 M_6^{1/3} \left(\frac{1 + z_c}{10}\right)^{-1}\ \mathrm{kpc}, \tag{4.1}$$

and its virial velocity is

$$v_c = 4.4 M_6^{1/3} \left(\frac{1 + z_c}{10}\right)^{1/2}\ \mathrm{km\ s^{-1}}. \tag{4.2}$$

The radial profile of the minihalo was taken from Navarro *et al.* (1997):

$$\rho(R) = \frac{\Omega_0 \rho_c}{cx(1 + cx)^2} \frac{c^2}{3F(c)}\ \mathrm{g\ cm^{-3}}, \tag{4.3}$$

where c is the halo concentration parameter, $x \equiv R/R_c$, and $F(t) \equiv \ln(1 + t) - \frac{t}{1+t}$. As the minihalo collapses, we assume that the gas is isothermal and heated to its virial temperature of $T_c = 720 M_6^{2/3}[(1 + z_c)/10]$ K, which

produces an isothermal gas density distribution in the CDM potential well of

$$\rho_{\rm gas}(R) = \rho_0 e^{-[v^2_{\rm esc}(0) - v^2_{\rm esc}(R)]/v_c^2} \text{ g cm}^{-3}, \tag{4.4}$$

where $v^2_{\rm esc}(R = xR_c) = 2v_c^2[F(cx) + cx/(1+cx)][xF(c)]^{-1}$ is the escape velocity of a particle at a distance R from the halo center, $v^2_{\rm esc}(0) = 2v_c^2 c/F(c)$, and c is the halo concentration factor which has a fiducial value of 4.8 (Madau *et al.* 2001). The central gas density of the cloud is then

$$\rho_0 \quad = \quad \frac{(178/3)c^3\Omega_b e^A (1+z_c)^3}{\int_0^c (1+t)^{(A/t)} t^2 dt} \text{ gm cm}^{-3}, \tag{4.5}$$

where $A \equiv 2c/F(c)$ and $t \equiv cx$. Outside the virial radius of the cloud, we assume that the gas is at the same temperature as the minihalo and in hydrostatic balance with it. This leads to a density distribution of

$$\rho(R > R_c) = \rho(R_c) e^{\frac{R_0}{R} - \frac{R_0}{R_c}} \text{ gm cm}^{-3}, \tag{4.6}$$

where R is the radius, R_c is the virial radius, and $R_0 = GM_c m_p / k_b T$, where $\rm M_c$ and T are the mass and virial temperature of the cloud.

We begin each simulation with the halo in hydrostatic equilibrium using a two part gravity scheme to account for the self-gravity of the gas and the dark matter halo. The self-gravity was handled by the efficient multigrid Poisson solver (Ricker 2008) which is included in FLASH. The dark matter term was handled by first calculating the total gravitational acceleration due to the total (dark matter + gas) mass distribution (via Eqn. 4.4) and subtracting off the term for the initial gas configuration before adding the results of the self-gravity calculation. Thus, initially when the cloud is pressure supported against collapse the gas-only and self-gravity terms cancel. Outside the acceleration due to the dark matter was calculated as $-GM_c/R^2$ cm s^{-2}, and again the gas was taken to be in initial hydrostatic equilibrium according to Eq. 4.6.

Outflow

The galactic outflow was modeled as a Sedov-Taylor blast wave. I assumed that the minihalo sits at a (physical) distance R_s and that the shock moves with a velocity of

$$v_s = 760\delta_{44}^{-1/2}(\epsilon E_{55})^{1/2}\left(\frac{1+z_s}{10}\right)^{-3/2} R_s^{-3/2} \text{ km s}^{-1}, \tag{4.7}$$

where $\delta_{44} = \delta/44$, and δ is defined as the ratio of the density of the gas compared to the mean density at that redshift, ϵE_{55} is the input energy of the shock wave where ϵ is the wind efficiency and E_{55} is the total SNe energy in units of 10^{55} ergs, and z_s is the redshift when the outflow reaches the halo (Scannapieco *et al.* 2004). The postshock temperature is $T_s = 1.4 \times 10^5 (v_s/100 \text{ km s}^{-1})^2$ K. By the time the outflow reaches R_s it has entrained a mass of

$$M_{\text{s,total}} = 1.4 \times 10^6 \delta_{44}\left(\frac{1+z_s}{10}\right)^3 R_s^3 \text{ M}_{\odot}, \tag{4.8}$$

and has a surface density of

$$\sigma_s = 1.0 \times 10^5 \delta_{44}\left(\frac{1+z_s}{10}\right)^3 R_s \text{ M}_{\odot} \text{ kpc}^{-2}. \tag{4.9}$$

The outflow is assumed to consist of completely ionized hydrogen and helium with the same relative abundances as the primordial gas, but enriched with metals from the supernovae that drove the material out of the host galaxy. To determine the metal abundance, we followed the estimate from Chapter 3 and Scannapieco *et al.* (2004) and assumed that each supernova, whether a core-collapse or more-exotic pair-instability supernova (Woosley & Weaver 1995; Heger & Woosley 2002), generates 2 $\text{M}_{\odot}$ of metals per 10^{51} ergs of energy. If half of these metals are funneled into the outflow, we can expect a total mass of metals of $\text{M}_{\text{metal}} = 10^4 E_{55}$ $\text{M}_{\odot}$. We therefore initialized the shock with an initial

abundance of

$$\frac{Z_{\rm metal}}{Z_\odot} = \frac{M_{\rm metal}}{M_{\rm s,total}} = \frac{10^4 E_{55}\ M_\odot}{1.4 \times 10^6 \delta_{44} \left(\frac{1+z_s}{10}\right)^3 R_s^3} \tag{4.10}$$

The lifetime of the shock can be estimated from $\sigma_s = \rho_{\rm post} v_{\rm post} {\rm t}_s$, where σ_s is the surface density of the outflow, $\rho_{\rm post}$ is the post shock density, v_{post} is the post shock velocity, and ${\rm t}_s$ is the shock lifetime. After a period ${\rm t}_{full}$, which is nominally defined as 1.5 Myrs, the shock was allowed to taper off by slowly lowering the density and raising the temperature so that the pressure stayed constant. This prevents the courant time step from becoming exceedingly small long after the shock had passed over the minihalo. For more setup details see Chapter 2 and Chapter 3.

4.2 Parameter Study

Table 4.1 summarizes the range of parameters studied in our simulations. Each case is given a name based on the value of the parameter that was changed from the fiducial case. OFID is the fiducial model from Chapter 3, in which it was labeled MRWT. In all simulations the wind efficiency was $\epsilon = 0.3$, and the mean overdensity of the medium between the outflow and the minihalo was 44 ($\delta_{44} = 1$). Each simulation was performed in a rectangular box with the x-axis twice the size of the y- and z-axes. The minihalo was centered at [0,0,0] and the shock originated from the left x boundary. The base grid was taken to have 16 by 8 by 8 cells in the x, y, and z directions, and ${\rm l}_{\rm max} = 5$, such that up to 4 additional levels of refinement were added in regions with significant pressure or density structure. In Chapter 2 and Chapter 3 we varied the maximum resolution in our simulations, and showed that such medium-resolution ($256 \times 128 \times 128$ effective) simulations were able to faithfully reproduce the outcome of shock-outflow interactions. In the interest of speed we also included a forced-derefinement routine that required regions to derefine if their density

was less than 3.0×10^{-26} g cm^{-3}. This was implemented outside 393 pc from the center of the halo and after 7 Myrs from the beginning of the simulations, such that it only impacted low-density regions far from the evolving cloud.

Each simulation was run to a time at which the shock completely overran the minihalo, which was typically on the order of a few Myrs. However, the clouds are expected to evolve over hundreds of Myrs before reaching a final configuration, a time that is much longer than we were able to run our FLASH simulations. To get around this limitation, we transformed the final mass distribution in our 3-D simulations into a 1-D ballistic problem, as described in Chapter 2.

Here, the mass distribution at the final output from each simulation was divided into 100 evenly spaced bins along the x-axis, and the mass of each bin was calculated by summing together the gas within a cylinder with a radius of 10^{21} cm and a length set by the bin spacing. Next each bin was converted into a particle, whose initial position was located at the center of mass of the summed density distribution, and whose initial velocity was calculated from conservation of momentum. These particles were then evolved ballistically using a leap-frog method. At every time step, the acceleration of each particle was calculated from the self-gravity from all other particles as well as from the gravity from the dark matter halo. If a particle moved past the one in front of it, they were merged by adding together their masses and calculating a new velocity from momentum conservation. The outcomes from the different runs were then compared with each other at a time of 200 Myrs after the end of each simulation.

Table 4.1: Summary of Study Parameters. M_6 is the minihalo mass in units of $M_6 = M_c/10^6$ $M_\odot$, E_{55} is the energy of the shock in units of $E/10^{55}$ ergs, R_s is the distance between the galaxy and the minihalo in units of (physical) kpc, z_c is the redshift at which the halo virializes, z_s is the redshift at which the shock reaches the minihalo, λ' is the spin parameter (see §4.2), c is the concentration parameter, Z is the metal abundance of the outflow in units of solar metallicity ($Z_\odot$), and Res is the minimum resolution of each simulation in units of pc.

Name	M_6	E_{55}	R_s (kpc)	z_c	z_s	λ'	c	Z ($Z_\odot$)	Res (pc)	Notes
OFID	3	10	3.6	10	8	0	4.8	0.12	9.14	Original Fiducial
PM10/NFID	10	10	3.6	10	8	0	4.8	0.12	19.85	New Fiducial
PM03	0.3	10	3.6	10	8	0	4.8	0.12	5.06	
PM30	30	10	3.6	10	8	0	4.8	0.12	19.85	
PE1	10	1	3.6	10	8	0	4.8	0.06	19.85	
PE5	10	5	3.6	10	8	0	4.8	0.06	19.85	
PE20	10	20	3.6	10	8	0	4.8	0.24	19.85	
PE30	10	30	3.6	10	8	0	4.8	0.36	19.85	
PZC8	10	10	3.6	8	8	0	4.8	0.12	19.85	
PZC15	10	10	3.6	15	8	0	4.8	0.12	19.85	
PZS10	10	10	3.6	10	10	0	4.8	0.12	19.85	
PR21	10	10	2.1	10	8	0	4.8	0.60	19.85	
PR66	10	10	6.6	10	8	0	4.8	0.019	19.85	
PR120	10	10	12	10	8	0	4.8	0.003	19.85	
PSPZ	10	10	3.6	10	8	0.023	4.8	0.12	19.85	Angle = 0°
PSPN	10	10	3.6	10	8	0.023	4.8	0.12	19.85	Angle = 90°
PC32	10	10	3.6	10	8	0	3.2	0.120	19.85	
PC73	10	10	3.6	10	8	0	7.3	0.12	19.85	

Effect of Halo Mass

The outflow-minihalo interaction goes through several evolutionary stages, which are illustrated in Figure 4.1. As the outflow impacts the front of the minihalo, the atomic gas is ionized but then cools rapidly. As the temperature approaches $\approx 10^4$K, molecules begin to form, catalyzed by H^- and H^+. Since the shock moves faster through the less dense regions of the minihalo, molecule formation predominately occurs in the gas surrounding the center of the impacted minihalo (top left panel). When the outflow meets at the back of the minihalo, however, a second shock is driven backwards toward the center of the collapsing cloud. This promotes molecule formation in the center of the minihalo, which continues to collapse as it further loses pressure support (top right panel). As the cloud becomes more elongated (bottom left panel), the

shear layer between the outflow and cloud becomes more and more turbulent, mixing metals into the cloud. The final state of the simulation (bottom right panel) is similar to that seen in the runs in Chapter 2 and Chapter 3: the gas from the minihalo has been moved out from the dark matter halo and formed a dense, cold ribbon of material stretched along the x-axis.

As the total mass in the impinging wind is relatively small, the minihalo is the primary source of gas for the final dense stellar clusters. Figure 4.2 shows the impact of changing this mass, illustrating the final state of runs with minihalo masses ranging between 0.3 to 30 $\times 10^6$ $M_\odot$. In all cases the gas from the minihalo forms dense cold clumps embedded in a ribbon of diffuse gas, stretching away from the dark matter halo. The larger the halo mass, the longer the ribbon. In the larger halos, a very slight metallicity gradient is observed as some of the gas in the center of the halo is not as enriched as the surrounding gas. However, every part of the ribbon is enriched to well above $10^{-3} Z_\odot$, and the majority of the gas is enriched to a nearly constant value of $\approx 10^{-2} Z_\odot$.

Figure 4.3 shows the evolved distribution of stellar clusters. The relative sizes of each cluster corresponds to their final mass, with larger symbols representing larger clusters. As expected, the more massive the initial halo, the more massive the final clusters. In the case of the largest mass minihalo, the outflow is not strong enough to remove all the gas. Instead it leaves behind a rather sizable cluster at the center of the dark matter halo, although even more massive clusters are formed behind it. In all other cases, the outflow effectively removes all of the gas and forms several dense clusters. Since the final cluster sizes are larger in the PM10 model relative to the $M_6 = 3$ run, but 10^7 $M_\odot$ minihalos are still quite common at high-redshift, we use it as our new fiducial model (NFID) and maintain this value in the simulations discussed below.

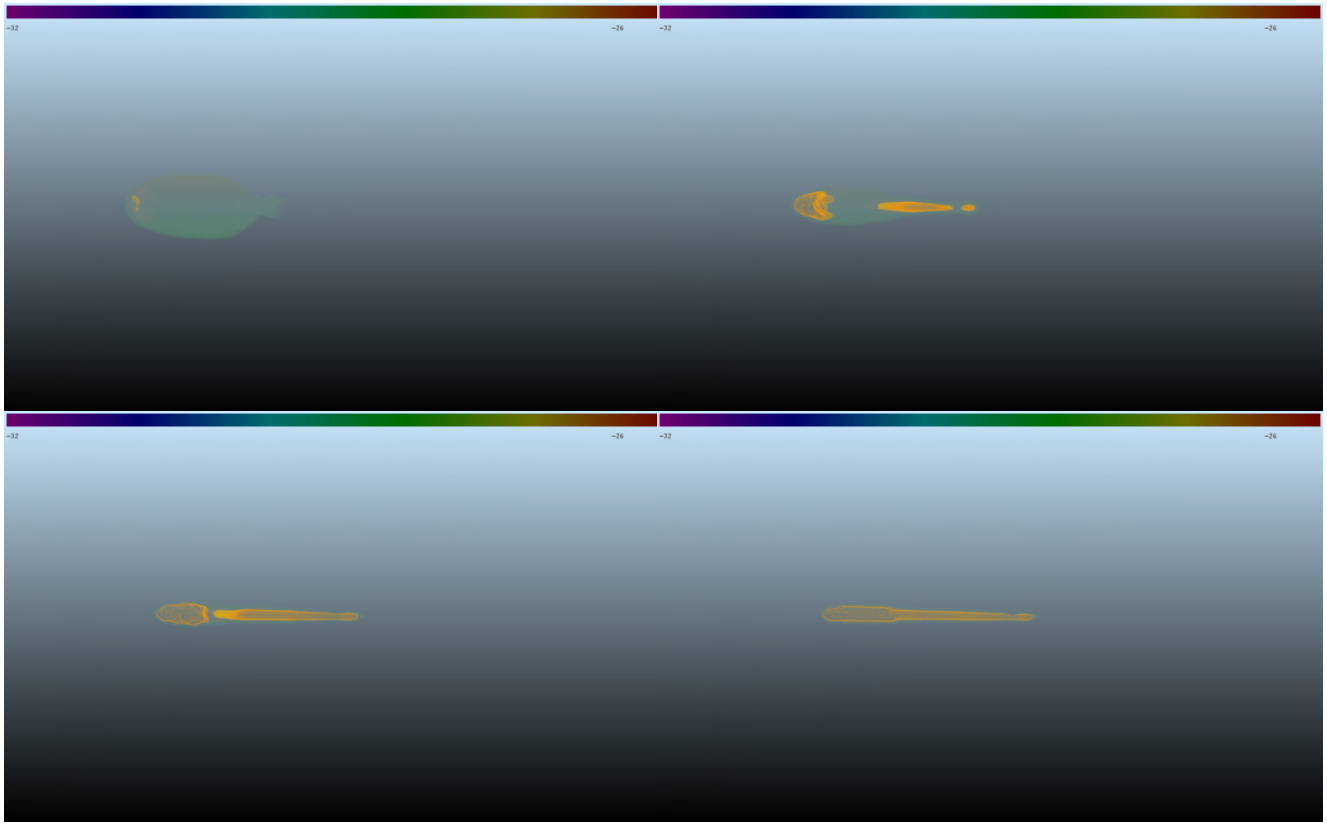

Figure 4.1: Rendered snapshots of the logarithm of the H_2 density for run PM10/NFID. Colors show logarithmic contours of H_2 density from 10^{-32} to 10^{-26} g cm^{-3}. *Top Left:* $t = 12.2$ Myrs, showing the outflow completely surrounding the minihalo and H_2 formation starting at the front of the cloud. *Top Right:* $t = 15.7$ Myrs, showing the minihalo as it is collapsing and during which H_2 is increasing towards the center of the cloud. *Bottom Left:* $t = 19.2$ Myrs, showing both the cloud as it is stretched and the H_2 that is then found throughout the dense ribbon. *Bottom Right:* $t = 22.0$ Myrs, showing the final state of run PM10 and the uniformly cold ribbon of gas.

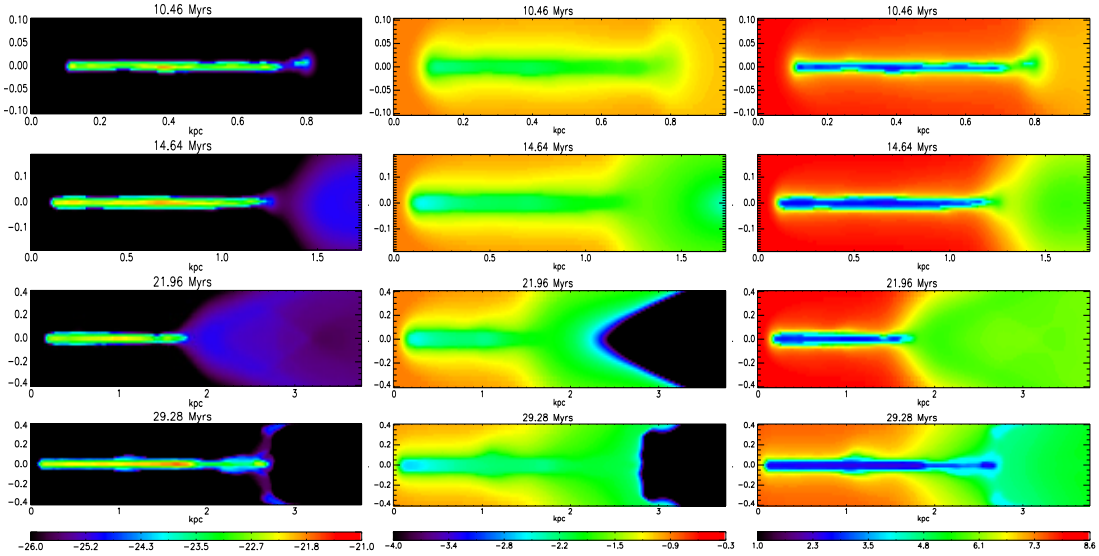

Figure 4.2: Comparison of final outputs from runs with varying halo masses. The first column shows logarithmic density contours from 10^{-26} to 10^{-21} g cm^{-3}, the second column shows logarithmic metallicity contours between 10^{-4} and $10^{-0.3}$ $Z_{\odot}$, and the third column shows logarithmic temperature contours between 10 and $10^{8.6}$ K. The first row shows results from run PM03, the second row shows results from OFID, the third row shows results from run PM10, and the last row shows results from run PM30. In all cases the outcome is similar. The minihalo gas is moved out from the dark matter halo, stretched along the x-axis, and enriched homogeneously.

Effect of Shock Energy

The shock plays three important roles in the evolution of these interactions. First, it accelerates the minihalo gas with enough momentum to move it out of the dark matter halo, second, it provides enough energy to ionize the gas, trigging the non-equilibrium chemical reactions that provide an avenue for H_2 and HD formation and cooling, and finally, the shock brings in the metals that enrich the post-shock star-forming medium.

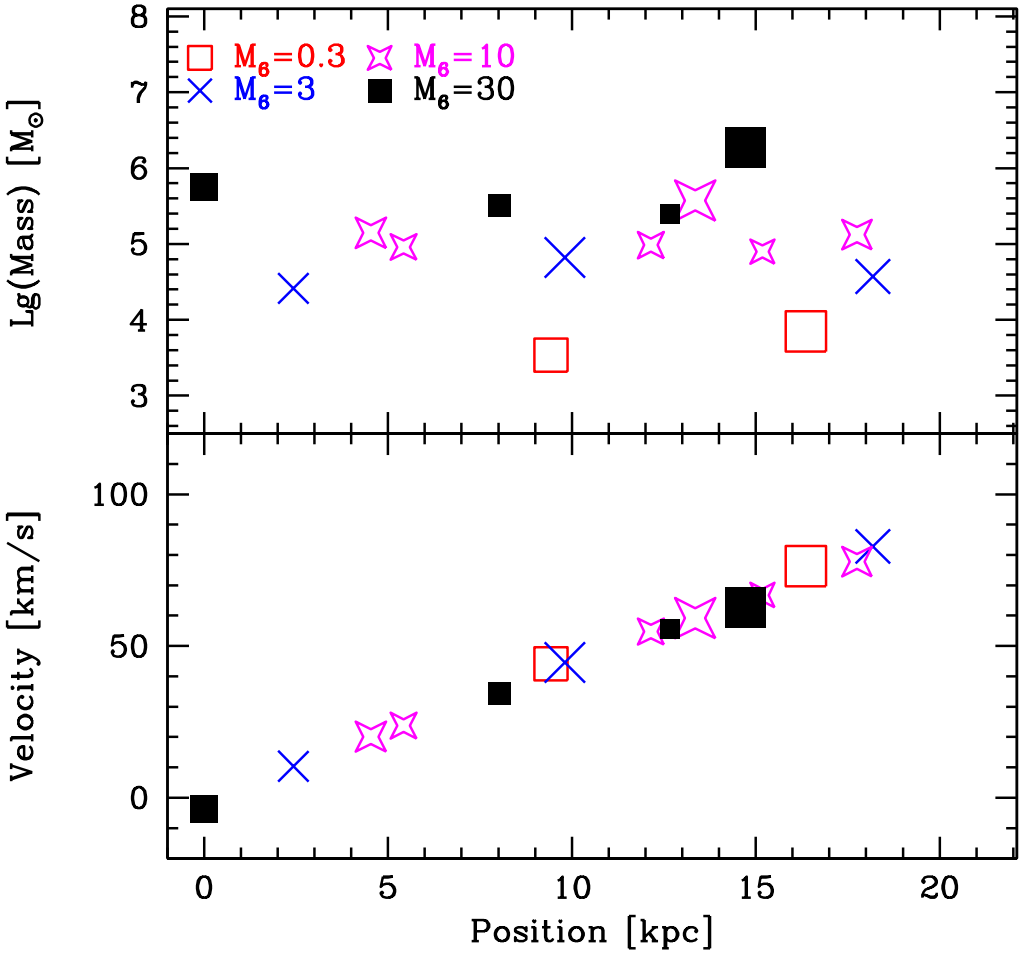

Figure 4.3: Comparison of clusters generated in models with varying halo mass at a time of 200 Myrs after the end of the simulations. The top panel shows the logarithmic mass and the bottom panel shows the velocity of each cluster. The x-axis is the distance of each cluster from the center of their dark matter halos. The (red) unfilled squares show the PM03 model, the (blue) crosses show the OFID model, the (magenta) stars show the NFID/PM10 model, and the (black) filled squares show the PM30 model. The relative size of the points is proportional to the fraction of the total minihalo gas mass contained in each cluster. Only clusters that have masses greater than 5% of the initial baryonic halo mass are shown. The total mass of clusters from each model is 4.1 $\times 10^4$, 4.0 $\times 10^5$, 1.6 $\times 10^6$, and 4.8 $\times 10^6$ $M_\odot$, for PM03, OFID, PM10, and PM30 respectively. Except for the high mass-case, every cluster is found outside of its dark matter halo.

The single most important parameter in determining each of these effects is the energy driving the shock, E_{55}, as this not only sets the shock velocity (Eq. 4.7), but determines the total associated metal mass and abundance (Eq. 4.10).

The fiducial estimate for E_{55} is taken from Scannapieco *et al.* (2004) where they estimate the energy in the outflow of a high-redshift starburst galaxy. First, consider a a young galaxy of total mass $M_g = 10^9$ $M_\odot$ that has a virial temperature greater than 10^4 K and is therefore allowed to cool via atomic hydrogen. If 10% of the gas is converted into stars and 10^{51} ergs of energy is produced by SNe for every 30 $M_\odot$ of stellar material for massive stars (Pop III, Heger & Woosley 2002) then the expected total energy given off is $E_{55} \approx 50 M_9$, where M_9 is the mass of the galaxy in units of 10^9 $M_\odot$. In simulations by Mori *et al.* (2002) the wind efficiency ϵ is found to be ≈ 0.3 for a $2.0 \times 10^8 M_\odot$ starbursting galaxy. Using these numbers, the fiducial value for E_{55} is obtained. To get an idea of how this parameter alters the evolution of the minihalo, we allow this value to range between $1 < E_{55} < 30$.

Figure 4.4 shows the results of altering this key parameter. Each row corresponds to a different value of E_{55}, which increases from top to bottom as 1, 5, 10, 20, and 30, respectively. As the shock energy increases, the minihalo evolution changes dramatically. Instead of stretching the gas into a ribbon as in the fiducial case, $E_{55} = 10$ case, the stronger shocks crush the cloud into a single small, dense cluster. Interestingly, even though these high-energy interactions happen quickly, there is still enough time to mix in the metals from the shock. In all cases the metallicity is $\approx 10^{-2} Z_\odot$, a value that is roughly constant across models in part because the higher energy shock models have higher initial metal abundances. On the other hand, the lower the shock energy, the more the cloud is stretched into a diffuse ribbon in which smaller clusters are embedded.

Over time, much of the surrounding gas merges with the initial cluster, which is similar to the evolution we found in Chapter 2 and Chapter 3. However, this is not true in models with high-energy shocks since no extended ribbon is formed. These differences are apparent in Figure 4.5 which shows the final state of each model. Here we see that the mass in the high energy models is concentrated into a single object, moving outwards at a significant velocity from the dark matter halo. Conversely, for low E_{55} values, the gas condenses to form a number of smaller star clusters that are well separated from each other. At the lowest energy level of $E_{55} = 1$, the shock strips some of the baryonic matter from the dark matter halo but leaves behind a small dense cluster at the center of the halo. Additionally, the metal content of such a weak shock is not sufficient to enrich the resulting cluster to the $\approx 10^{-2} Z_{\odot}$ threshold.

Effect of Minihalo Virialization Redshift

Many of the basic properties of the halo, from the central density of the cloud to the radial density distribution, are strongly dependent on the minihalo virialization redshift (see Eqs. 4.1-4.6). In general, the higher the virialization redshift, the more compact the minihalo, and thus the more resistant it is likely to be to external shocks. To explore the impact of this parameter, we conducted two simulations in which z_c was taken to be 10 (PZC10) and 15 (PZC15) as compared to our fiducial value of 8. The final states of each of these runs is shown in Figure 4.6. It is important to note that the higher redshift simulations act as a more robust prediction of our model for globular cluster formation since by $z \sim 8$ many of these minihalo may have been stripped of their baryons via ionization fronts during reionization.

For all virialization redshifts, most of the mass from the halo is moved into a ribbon of material along the x-axis, but at higher virialization redshifts,

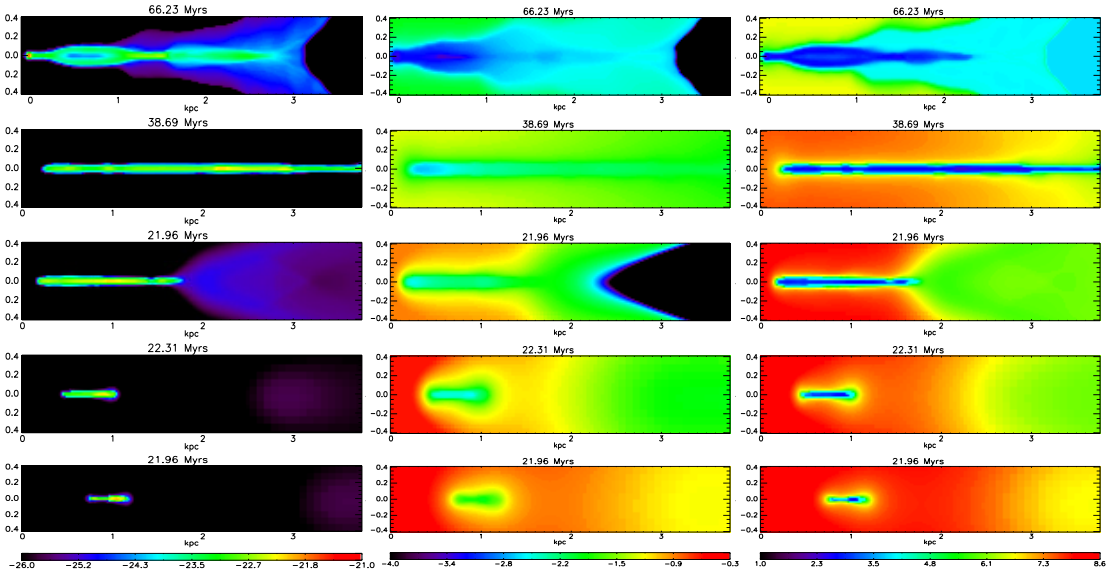

Figure 4.4: Comparison of final outputs from runs with varying outflow energies. From top to bottom each row represents runs with E_{55} = 1, 5, 10, 20, and 30, respectively. As in Figure 4.2 the first column shows logarithmic density contours from 10^{-26} to 10^{-21} g cm^{-3} and the second column shows logarithmic contours of metallicity from 10^{-4} to $10^{-0.3}$ Z$_\odot$, but now the third column shows logarithmic temperature contours between 10 and $10^{8.6}$ K. The length of the ribbon is correlated with the initial shock energy: the smaller the energy, the longer the ribbon.

the cloud is more compact (Eq. 4.1) and the gas in the center of the halo cannot escape as easily as the surrounding gas. Also, as the virialization redshift increases, the physical size of the ribbon increases as does the total the entrained mass. Again, in all cases the clouds have been enriched to approximately 10^{-2} Z$_\odot$ although the centers of the two oldest minihalos (those in runs PZC10 and PZC15) have slightly lower abundances.

Figure 4.7 shows the evolved distribution of these models. At lower virialization redshifts (z$_c$ = 8 and 10) the final distributions are very similar, and the number of clusters formed and the final mass of these clusters match well. At the highest virialization redshift, on the other hand, the distribution is quite

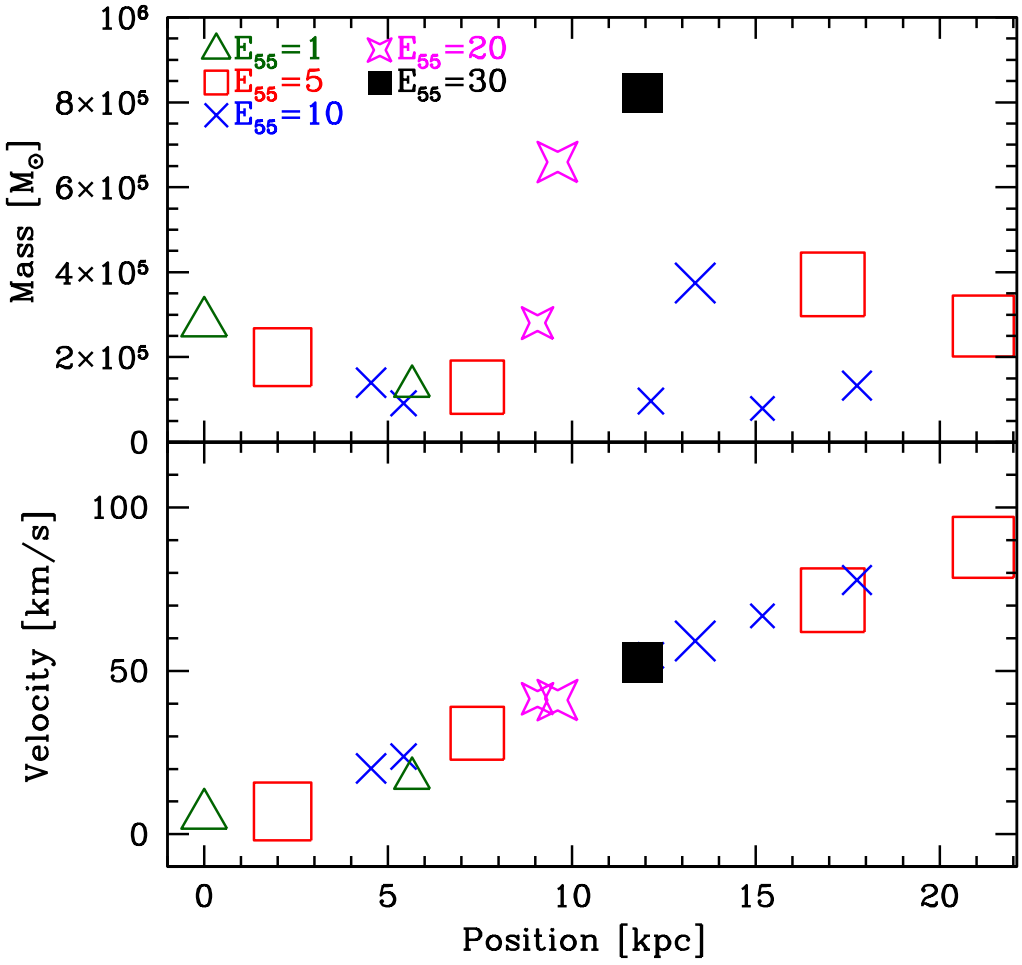

Figure 4.5: Comparison of clusters generated in runs with varying outflow energies. Panels are the same as Figure 4.3, except the y-axis of the top panel is given in linear units rather than logarithmic. The (green) unfilled triangles show the clusters formed from PE1, (red) unfilled squares show the clusters from PE5, the (blue) crosses show the clusters from NFID, the (magenta) stars show the clusters from PE20, and the (black) filled squares show the clusters from PE30. The total mass of the clusters formed is 9.0 $\times 10^6$, 2.3 $\times 10^6$, 1.6 $\times 10^6$, 9.5 $\times 10^5$, and 8.2 $\times 10^5 M_\odot$ in PE1, PE5, NFID, PE20, and PE30 respectively. In general, the larger the outflow energy, the more the initial halo is crushed rather than forming a long stream of gas. This leads to the formation of fewer, larger clusters.

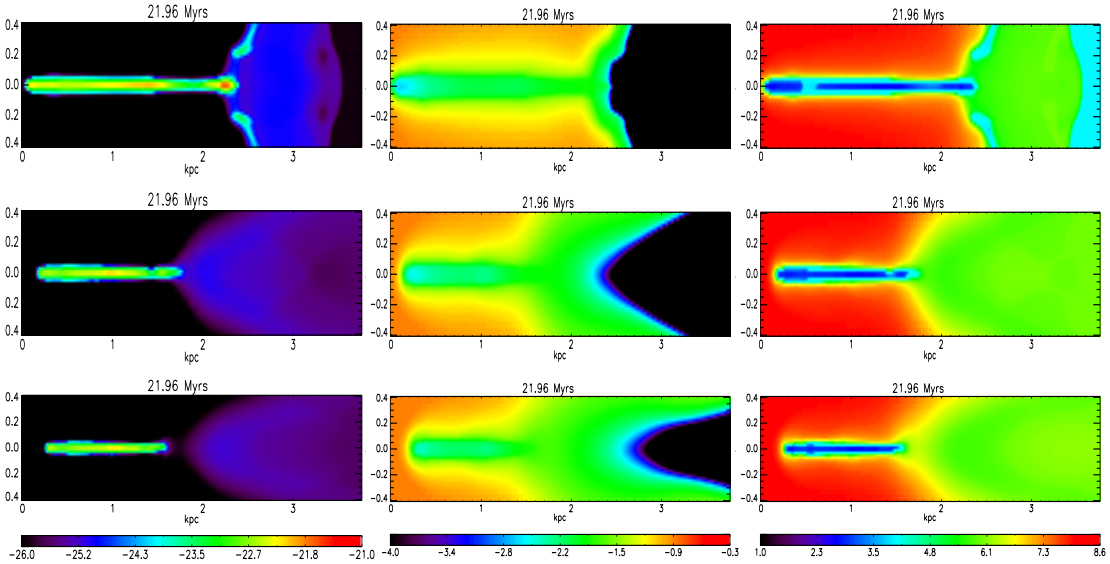

Figure 4.6: Comparison of final outputs from runs with different minihalo virialization redshifts. From left to right the columns show logarithmic contours of density, metallicity, and temperature with limits as in Figure 4.4. The top row shows the final state of run PZC15 ($z_c = 15$), the middle row shows the final state of run NFID ($z_c = 10$), and the bottom row shows the final state of run PZC8 ($z_c = 8$). In highest z_c redshift run, multiple large clusters are formed while in the lower z_c runs, only one primary cluster is formed. In all runs, the metal abundance remains roughly constant and near Z $\approx 10^{-2}$ $Z_\odot$ in the dense portions of the cloud, and the gas at the center of the dark matter halo is slightly deficient in metals.

different as one very large cluster is found nearly 20 kpc from the dark matter halo center. All of the other high redshift clusters are much smaller than those formed from minihalos with later virialization redshifts. This suggests that the formation of a large cluster (M $\approx$ few $\times 10^5$ $M_\odot$) is robust over a large redshift range and may actually occur more easily for minihalos with earlier virialization redshifts.

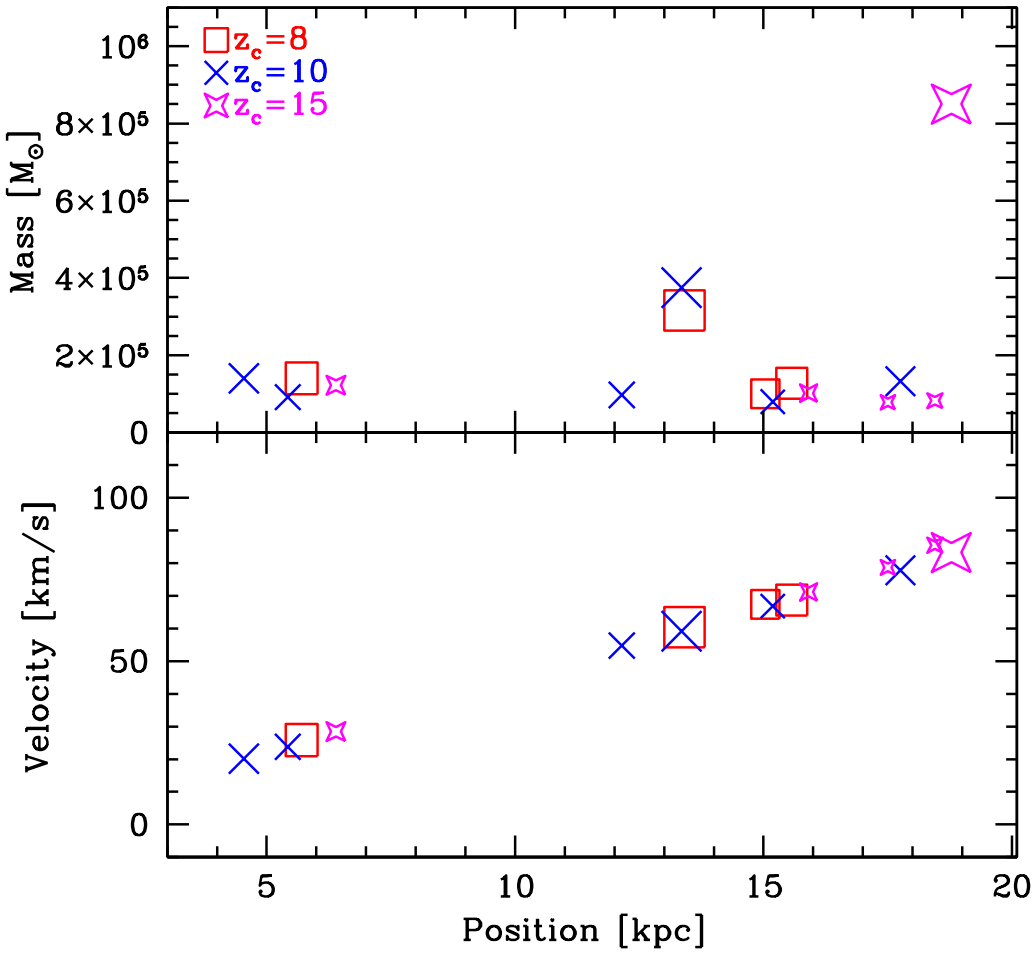

Figure 4.7: Comparison of clusters generated in runs with different virialization redshifts. Panels are the same as Figure 4.5. The (red) unfilled squares show the clusters from PZC8, the (blue) crosses show the clusters from NFID, and the (magenta) stars show the clusters from PZC15. The total mass of clusters is 1.2 $\times 10^6$, 1.6 $\times 10^6$, and 2.3 $\times 10^6$ $M_\odot$ for runs PZC8, NFID, and PZC15 respectively. At lower redshifts the sizes and distribution of clusters is fairly similar, with at least one cluster with mass greater than 2.0 $\times 10^5 M_\odot$ while at high redshift only one large cluster is formed. In all cases the largest clusters are found far from their respective dark matter halos.

Effect of Shock Redshift

Other than E_{55}, the most important parameter in determining the properties of the shock is its redshift, z_s. As the shock redshift is increased the mass in the shock increases (Eq. 4.7) and the metal abundance decreases (Eq. 4.10), which in turn affect all aspects of the interaction. To study the effect of a shock occurring at a higher redshift than our fiducial run, a model was run in which the outflow reached the minihalo at precisely the minihalo virialization redshift ($z_s = z_c = 10$). The final state of this run is contrasted with the fiducial case in Figure 4.8.

The increased mass in the shock in run PZS10 leads to a much more stretched, elongated, and uniform mass distribution than in the NFID run. This elongated distribution makes it easier for the metals carried by the shock to be efficiently mixed into the collapsing cloud, and thus the metal abundance of the cloud in this run is higher than the fiducial model, even though the abundance of the shock is lower. On the other hand, the stretching in run PZS10 is not so severe as to suppress the formation of clusters, such as the one clearly visible at a distance of ≈2.5 kpc from the center of the dark matter halo.

Figure 4.9 compares the final stellar clusters generated by these two models. Even though the shock carries more mass in run PZS10 than in the fiducial case, the outcomes are fairly similar. Both have large clusters found outside the dark matter halo. Although fewer clusters are formed in run PZS10, the total mass in the clusters is slightly higher than in the fiducial model.

Effect of Distance from Starburst Galaxy

In Scannapieco *et al.* (2004) and in Chapter 2 and Chapter 3, the distance between the minihalo and the parent galaxy was taken to be $R_s = 1.5\ M_c^{-1/6}(\xi E_{55})\ \left(\frac{1+z_c}{10}\right)^{-1}$ kpc, a value that was chosen based on the observed

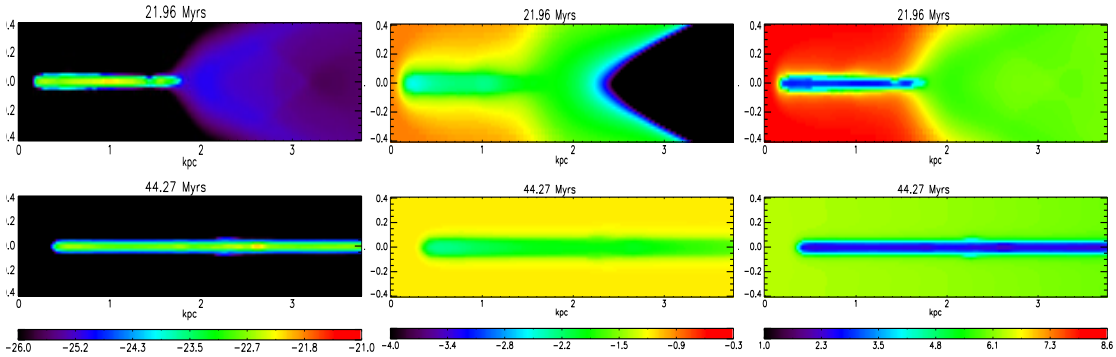

Figure 4.8: Comparison of final outputs from runs NFID (top) and PZS10 (bottom) which have outflow redshifts of $z_s = 8$ and $z_s = 10$, respectively. Panels are the same as Figure 4.4. The density is much more stretched and uniform than the fiducial case. While the metals from the shock have been mixed into the primordial gas, it is significantly more enriched than in the fiducial model. Both models reach the same final temperature.

metallicities of globular clusters. While this estimate gives a fiducial value of 3.6 (physical) kpc, in this study we consider the impact of varying this key parameter over a wide range of distances between $R_s = 2.1$ kpc (PR21) and $R_s = 12$ kpc (PR120).

Figure 4.10 shows the final outcome from each of these models. When the minihalo is close to the source of the outflow, the cloud is quickly crushed into a dense cluster, similar to what occurs in runs with a larger shock energy. In fact, this happens so quickly that there is little time for the metals to be effectively mixed into this cluster and the gas ends with a lower metal abundance than our previous results. However, enough momentum is imparted to the gas to remove it from the dark matter halo.

At intermediate distances (between 3.6 kpc and 6.6 kpc) the outcome is familiar. The cloud is stretched into a ribbon of gas and is expelled from the dark matter halo. The more the distance increases, the more the cloud is

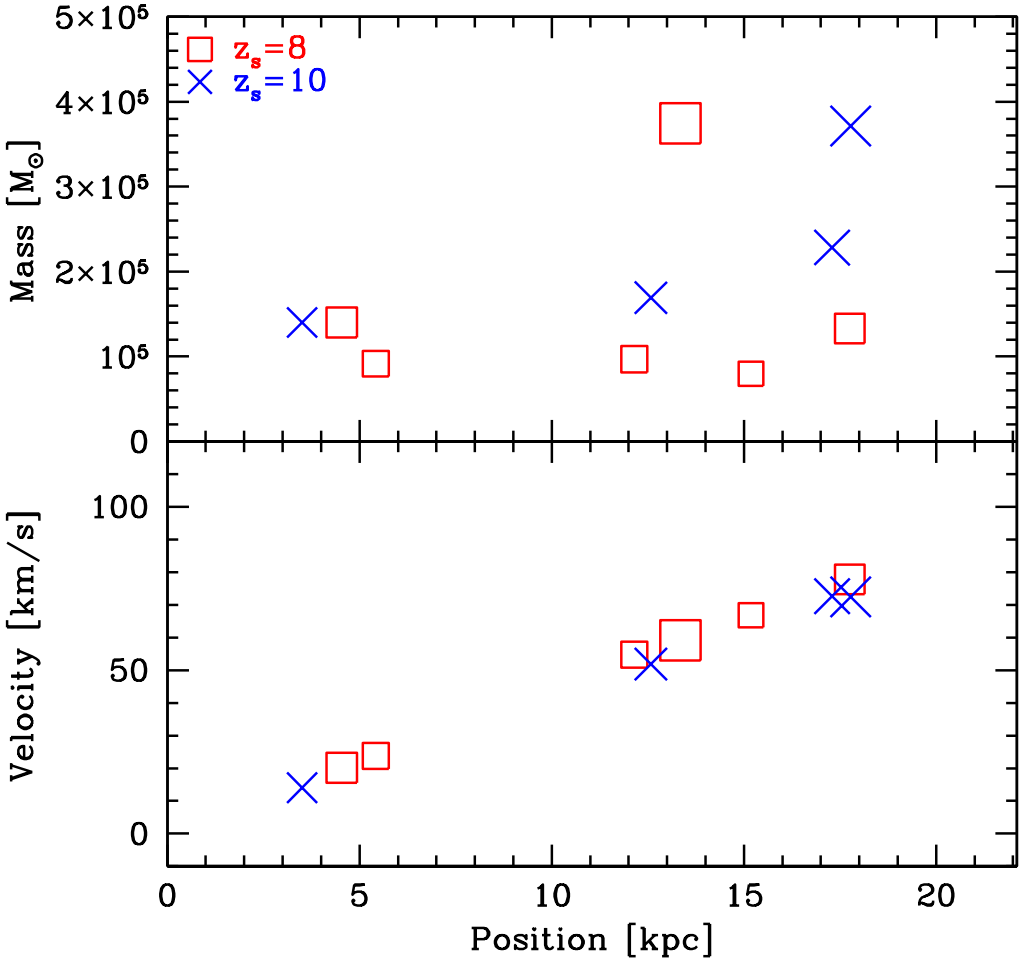

Figure 4.9: Comparison of clusters generated by runs with varying outflow redshifts. The panels are the same as in Figure 4.5. The (red) unfilled squares show the clusters from NFID and the (blue) crosses show the clusters from PZS10. The total mass of clusters for these models is 1.6 $\times 10^6$, and 2.3 $\times 10^6$ $M_\odot$ for NFID and PZC10 respectively. Although the shock lasts longer in the PZS10 case, there is little difference between these two cases. The PZS10 model has fewer, but slightly larger clusters than in the fiducial case and they are found outside of its dark matter halo. The positions and velocities are comparable between these two models.

stretched, and there is always enough time for metals to be mixed in the primordial gas to levels consistent with our previous runs.

Finally, at the largest R_s values, the cluster evolution is radically different than in the other models. The cloud is stretched as before but the resulting cluster does not leave the halo. The abundance of metals in the shock at this distance is already low, much lower than even the final cluster metallicities in many of our other runs, and while some metals are mixed into the cluster, it is very deficient compared to our other models.

Figure 4.11 shows the evolved state for each of these models. The panels are the same as Figure 4.5. The closest halo to the galaxy is transformed into a single cluster with a total mass of $7.0 \times 10^5 M_\odot$. The intermediate distance halos form large clusters with masses of $\approx 3.0 \times 10^5 M_\odot$ and several other smaller clusters with velocities and positions consistent of being free from the dark matter halo. Finally, the farthest halo forms two dense clusters, however the largest cluster is found at the center of the dark matter halo, and only the smaller cluster is free of the halo potential at 5 kpc from its center.

This suggests that there is a preferred distance from the outflow at which enriched clusters form most efficiently. Too close to the outflow and the minihalo is crushed before it is enriched and too far from the outflow and the minihalo in neither enriched nor ejected from its dark matter halo. Therefore it seems that between ≈ 3 and 7 (physical) kpc is a preferable distance from a typical starburst for the formation of compact stellar clusters. The observed distribution of halo globular cluster positions shows a drop-off beyond a galactocentric distance of 40 kpc (Dauphole *et al.* 1996). After evolving these clusters, the typical distance from the galaxy is between 15-30 kpc, which agrees nicely with the observed distances.

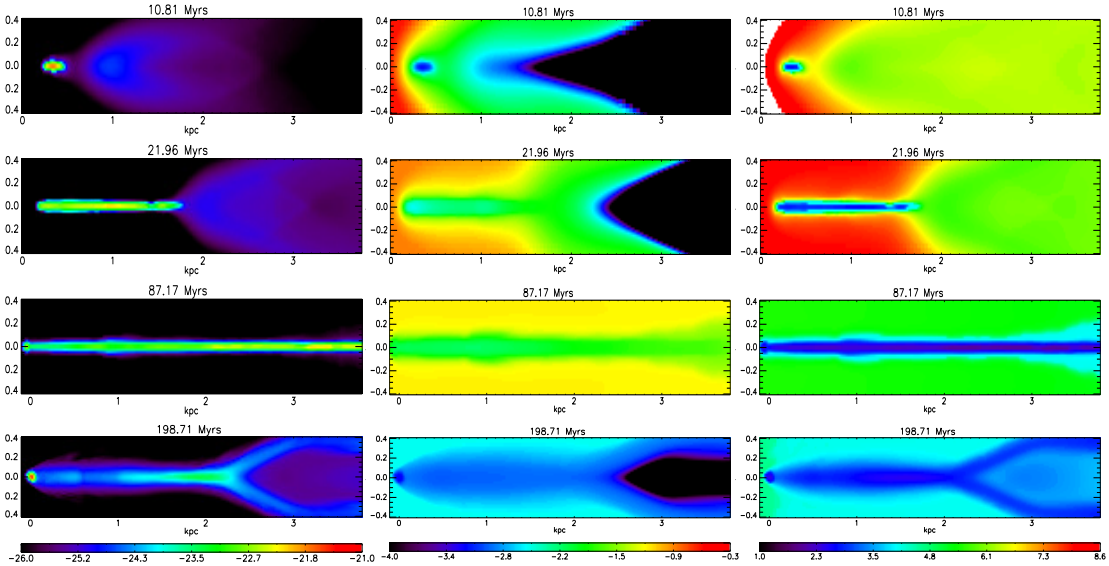

Figure 4.10: Comparison of final outputs from runs with varying distances between the minihalo and the galaxy. The first column shows logarithmic density contours between 10^{-26} and 10^{-21} g cm^{-3}, the second column shows logarithmic metallicity contours between $10^{-4.0}$ and $10^{-0.3}$ Z$_\odot$, and the third column shows logarithmic temperature contours between 10 and $10^{8.6}$ K. The top row shows the result of placing the minihalo at a distance of 2.1 kpc (PR21), the second is the fiducial distance of 3.6 kpc (NFID), the third row is a model with a distance of 6.6 kpc (PR66), and the last row shows the farthest case with a distance of 12.0 kpc (PR120). Beyond the apparent physical differences between each model, the metal abundance is lower than our fiducial model if the halo starts too close or too far from the outflow.

Effect of Halo Spin

Next we explored the effect of net rotation on the evolution of the minihalo. In this case, the gas was given an initial velocity according to

$$\begin{aligned} v_x &= -\alpha v_c \frac{y}{R_c}\cos(\phi), \\ v_y &= \alpha v_c \frac{x\,\cos(\phi) + z\,\sin(\phi)}{R_c}, \\ v_z &= \alpha v_c \frac{y}{R_c}\sin(\phi), \end{aligned} \tag{4.11}$$

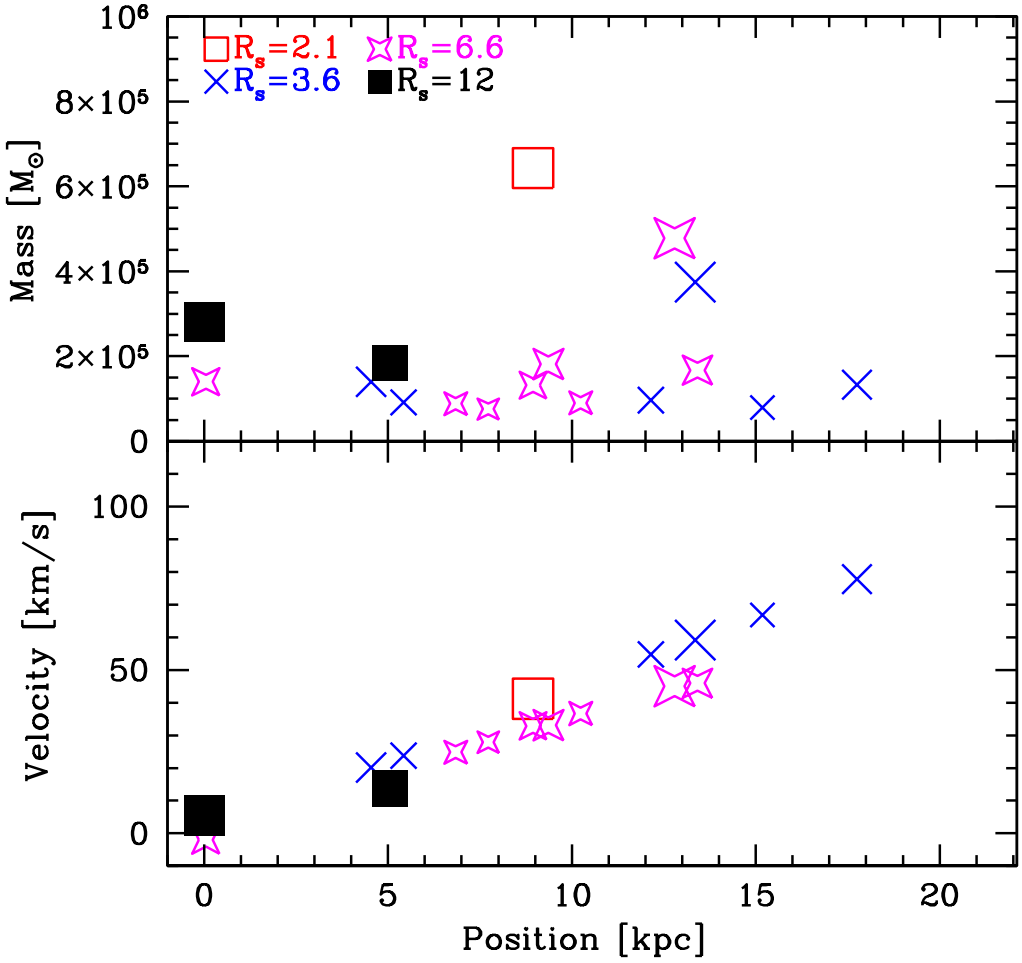

Figure 4.11: Comparison of clusters generated by runs with varying distances between the minihalo and the galaxy. The (red) unfilled squares show the clusters formed in PR21, the (blue) crosses show the clusters formed in NFID, the (magenta) stars show the clusters formed in PR66, and the (black) filled squares show the clusters formed in PR120. The panels are the same as in Figure 4.5. The total mass in each model is 7.0×10^5, 1.6×10^6, 2.1×10^6, and $7.5 \times 10^5 M_\odot$ for PR21, NFID, PR66, and PR120 respectively. While all models create at least one dense cluster far from the center of the halo, at the largest distances from the starbursting galaxy, the outflow is not strong enough to remove all of the gas from the halo. This leaves a cluster at the center of the dark matter halo.

where α is a constant, v_c is the virial velocity of the cloud, R_c is the virial radius, x and y are the positions within R_c, and ϕ is the rotation angle. Here, α is set at 0.05 and we vary ϕ between 0 and 90 degrees so that the halo rotates around the z-axis and x-axis respectively. For this value of α we can calculate the spin parameter of our halos using the form from Bullock *et al.* (2001b),

$$\lambda' = \frac{J}{\sqrt{2} M_{\rm vir} V_{\rm vir} R_{\rm vir}}, \tag{4.12}$$

where J is the angular momentum of the halo with mass $\rm M_{vir}$ contained in a sphere of radius $\rm R_{vir}$ and has a circular velocity of $\rm V_{vir}$. For the halos studied this gives a spin parameter of $\lambda' = 0.023$, which is within 1 σ of the mean value of $\lambda'_0 = 0.035$.

Figure 4.12 compares the simulations at the final time. It is obvious that neither the spin direction nor the magnitude of the spin changes the final distribution. In all cases the cloud is stretched into a ribbon along the x-axis, the primordial gas is enriched to nearly constant value near $10^{-2.0}$ $\rm Z_\odot$, and the cluster is cooled to a few hundred degrees K.

The reason for this insensitivity to λ' is a result of the shock itself. As the shock advances toward the halo it begins to develop vorticity, defined as $\vec{\omega} \equiv \vec{\nabla} \times \vec{v}$, which evolves as $\frac{D\vec{\omega}}{Dt} \approx \frac{1}{\rho^2} \vec{\nabla}\rho \times \vec{\nabla} p$, where v is the velocity, ρ is the density, and p is the pressure. Physically, this baroclinic source term is a measure of the generation of vorticity due to the mismatch between the gradients of pressure and density (Glasner *et al.* 1997). Since the shock is not aligned with the density gradient of the halo, this term is large throughout the simulation and vorticity begins to grow rapidly.

Figure 4.13 shows the z-component of vorticity as the shock heads toward the halo. By the time they meet the magnitude of the vorticity is much greater

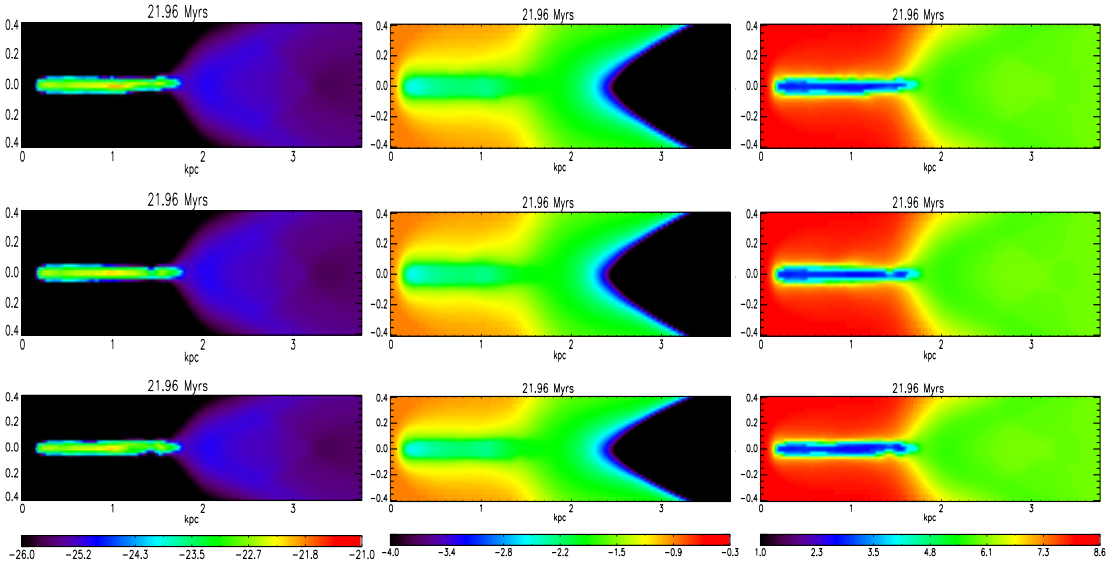

Figure 4.12: Final profiles of the spinning versus non-spinning halos. The top row shows the case in which the spin is about the z-axis (PSPZ). The middle row shows the non-rotating case (NFID) and the bottom row shows the case where the spin is about the x-axis (PSPN). The first column shows the logarithmic density contours, the second column shows the logarithmic metallicity contours, and the third column shows the logarithmic temperature contours. Panel limits are the same as in Figure 4.2. There is very little difference between each of these runs, which suggests that the initial spin of the minihalo does not contribute significantly to its final evolution.

than the spin of the halo. In fact, the vorticity would be much greater than the spin of the halo even if we had chosen an α of 1.0.

Effect of Halo Concentration

As the name suggests, the concentration parameter, c, describes in Eq.4.3 how the density is aggregated toward the center of the halo. Less concentrated halos have lower maximum central densities and shallower density profiles, while more concentrated halos have higher central gas densities and steeper density profiles at large radii. It is defined as

$$c \equiv R_{200}/R_s, \tag{4.13}$$

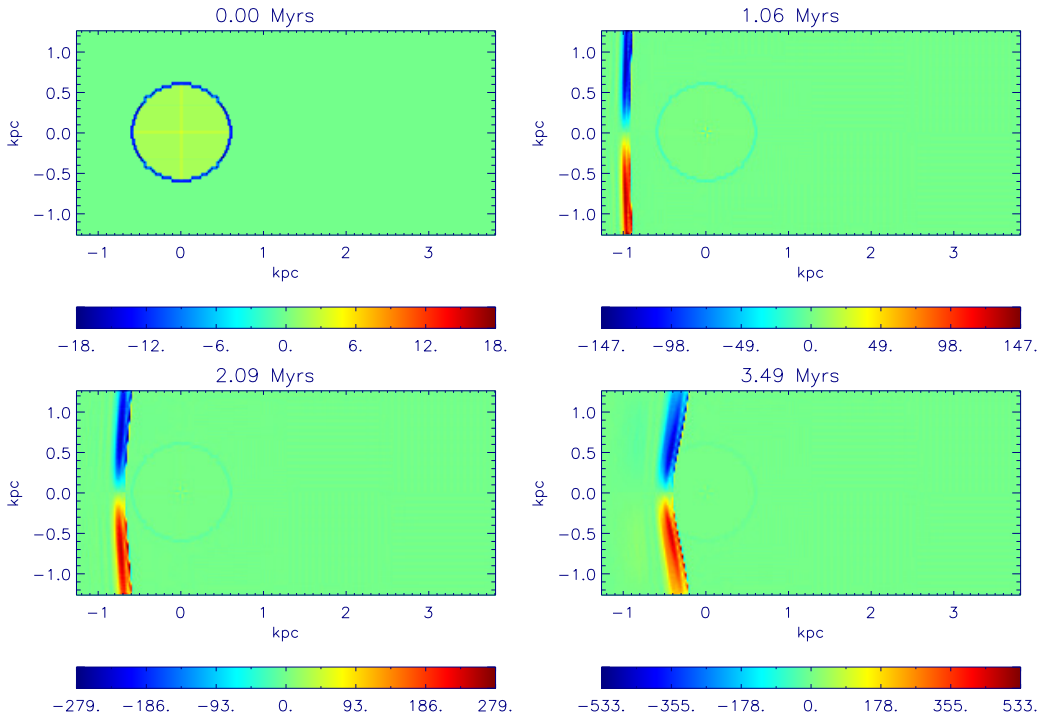

Figure 4.13: Snapshots of the z-component of vorticity at different times before the shock impacts the halo in run PSPZ. The top left panel shows the initial vorticity of the cloud. The top right and both bottom panels show the evolution of vorticity as the shock nears the halo. The scale is in units of km/s/kpc. As the shock nears the minihalo the vorticity increases and by the time it reaches the halo, it is much larger than the spin of the halo.

where R_{200} is the radius that corresponds to a density that is 200 times the critical density (Navarro *et al.* 1997) and R_s is the inner radius of the cloud. Typical values for NFW halos at this redshift are 4.8 (Madau *et al.* 2001). However, Bullock *et al.* (2001a) used high-resolution N-body simulations to study the dark matter halo density distribution and found that for a given mass the range in concentration parameter can be fairly large, 1σ $\Delta(\log c) = 0.18$. We therefore studied interactions with halos that cover this spread in concentration.

Figure 4.14 compares models of the minihalo after altering the concentration parameter. The top, middle, and bottom rows present the results

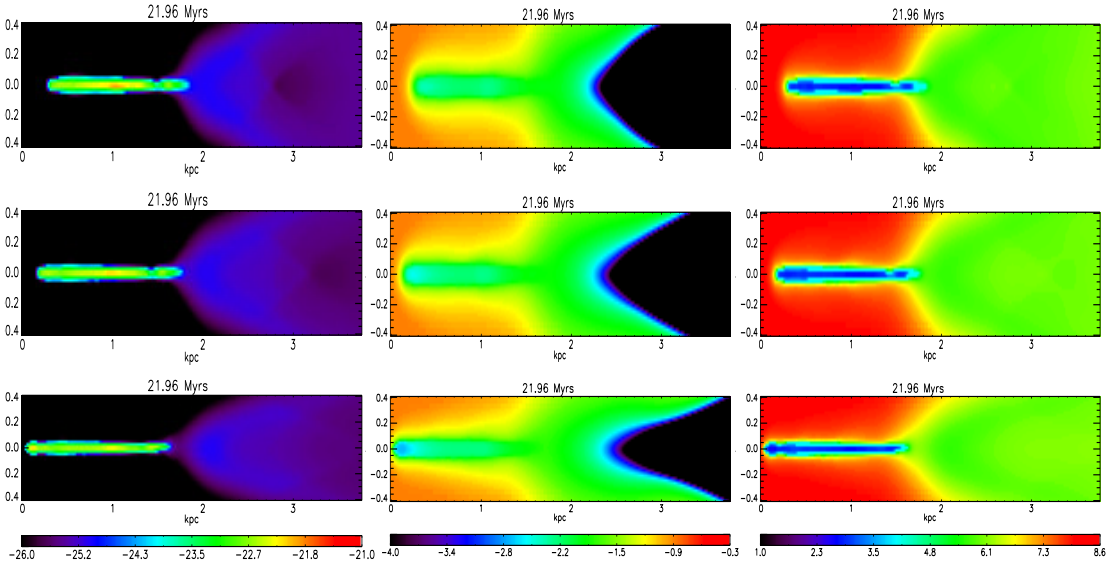

Figure 4.14: Comparison of final outputs from runs with different concentration parameters. The first row shows the $c = 3.2$ case (PC32), the second row shows the fiducial $c = 4.8$ case (NFID), and the third row shows the $c = 7.3$ case (PC72). Columns are the same as Figure 4.2. The more concentrated the halo, the more stretched it becomes and the less it is enriched.

of runs with $c = 3.2$, 4.8, and 7.3 respectively. As the halo becomes more concentrated, the metals have a harder time enriching the center of the halo, and becomes harder for the gas to be pushed out of the halo, which can be seen in the first column where the halo with the lowest concentration is farther away from the center of the halo.

Figure 4.15 shows the long term evolution of these models. Generally there is little difference between these models, which all contain at least one large cluster with a mass few $\times 10^5 M_\odot$. However, since there is more gas at near the edge of the less concentrated halos, the total mass of the ribbon is greater. Finally, in the most concentrated halo there is a portion of the gas that fails to leave the dark matter halo.

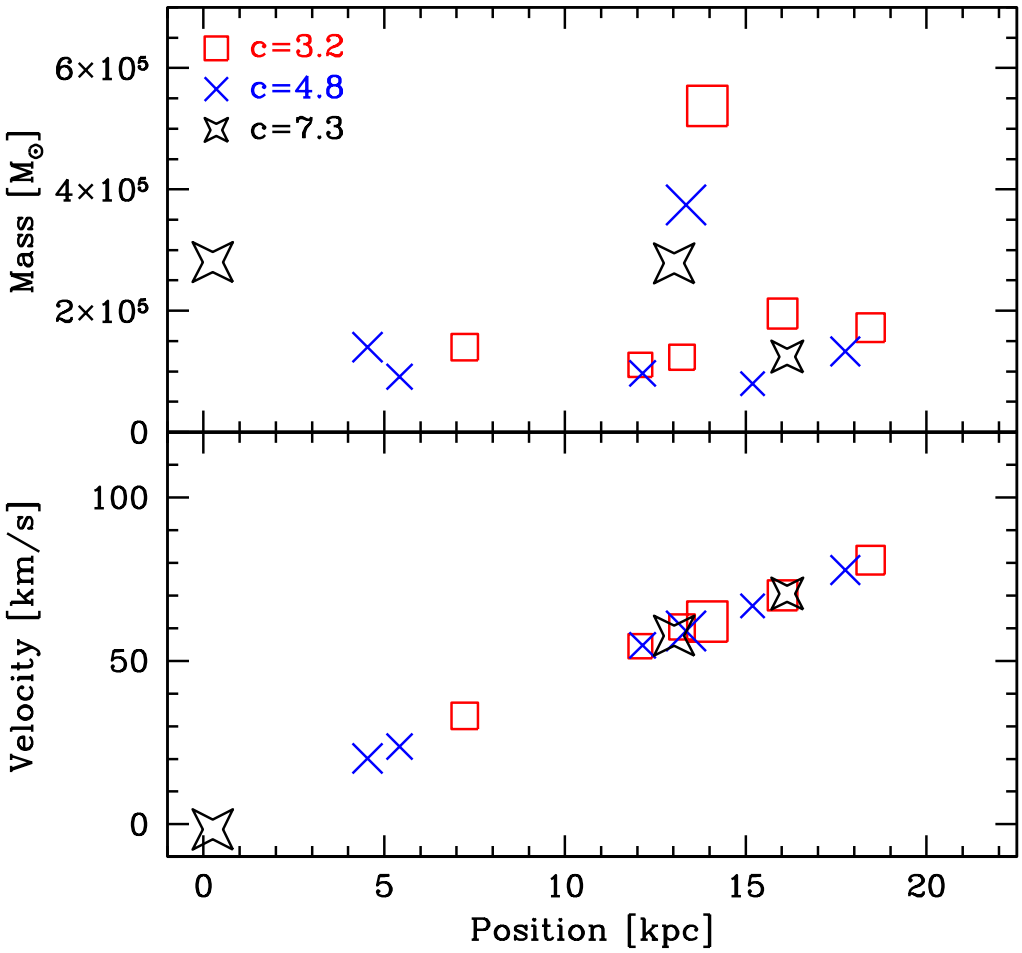

Figure 4.15: Comparison of clusters generated in runs with different halo concentrations. Panels are the same as Figure 4.5. The (red) unfilled squares show clusters from the least concentrated halo (PC32), the (blue) crosses show the clusters from the fiducial cluster (NFID), and the (black) stars show the clusters from the most concentrated halo (PC73). The total mass of clusters in each model is 1.8 $\times 10^6$, 1.6 $\times 10^6$, and 1.5 $\times 10^6 M_\odot$ for PC32, NFID, and PC73 respectively. The outflow has a hard time removing the gas from the most highly concentrated halo, and in this run a cluster is formed within the dark matter potential well. On the other hand, all the gas is ejected from the least concentrated halo, which forms the most massive cluster of any of the three runs.

Summary

Table 4.2 shows the final outcomes from all of our runs, including the total mass of clusters formed, and the basic properties of the largest cluster. My findings can be summarized as follows:

1. *The mass of the initial minihalo is closely correlated with the final mass of the compact clusters,* such that the more massive the initial halo, the more massive the total distribution of clusters. However, as the halo gets more massive, not all the gas is removed from the halo, and a sizable cluster forms at the center of the dark matter potential. In all cases the gas is enriched to nearly identical metal abundances, and only the center of the most massive minihalo is slightly less enriched.

2. *The total energy in the outflow primarily affects the degree to which the final distribution is stretched.* At low energies, the gas is shaped into a long ribbon of material that is enriched at a lower level than the fiducial model. As the energy increases, the ribbon becomes smaller until the halo is completely crushed, forming a single dense cluster with a similar metallicity as in the fiducial case.

3. *The collapse redshift of the minihalo directly affects the number and distribution of collapsed clusters.* Halos that collapse early each produce a massive cluster that is found far from the dark matter halo. Halos that collapse later form a large number of lower mass clusters. Generally the clusters' metal abundances are independent of minihalo collapse redshift, but the earlier redshift runs yield clusters with slightly metal-deficient cores.

4. *If the redshift of the shock is increased, it entrains more mass, moves slower, and stretches the minihalo gas more efficiently.* At lower redshifts, the shock crushes the cloud more efficiently, and a more compact ribbon is formed. At higher redshifts, the cloud is enriched slightly more than the lower redshift cloud, however both have an average abundance of $\approx 10^{-2}$ $Z_{\odot}$.

5. *The distance between the starburst galaxy and the minihalo has a dramatic impact on all properties of the final distribution of clusters.* At small separations the minihalo is quickly crushed and is deficient in metals. At slightly larger distances, metals are found at levels similar to our fiducial model, and the cloud is stretched into a ribbon of material, which becomes longer in runs with larger distances. At very large distances the cloud is disrupted but the outflow is too weak to move much of the gas out from the dark matter halo. Because the shock itself is metal-poor, the final cluster is also metal-poor.

6. *The initial spin of the halo has no discernible impact on the evolution of the minihalo.* This is because the vorticity generated during the shock minihalo interaction dwarfs that of the minihalo by orders of magnitude. All cases studied were identical to the case without spin.

7. *The concentration of the halo has a strong effect on the positions of the collapsed stellar clusters.* The more concentrated the minihalo, the harder it is for the outflow to remove the gas from the dark matter potential, and in the most concentrated case we studied, some halo gas remains in the dark matter halo. In all cases the gas is enriched to nearly identical levels with only the most concentrated gas at the center of the halo being

Table 4.2: Summary of model outcomes. M_{halo} is the initial gas mass of the minihalo in units of 10^6 $M_\odot$, $M_{clusters}$ is the total mass found in clusters in units of 10^6 $M_\odot$, M_{large} is the mass of the largest cluster formed in units of 10^6 $M_\odot$, $Z_{cluster}$ is the metallicity of the largest cluster, $V_{cluster}$ is the velocity of the cluster after 200 Myrs of evolution in units of km s^{-1}, and $D_{cluster}$ is the distance of the largest cluster from the center of its dark matter halo in units of (physical) kpc. An asterisk denotes that the data presented is for the first cluster found outside the DM halo.

Name	M_{halo} 10^6 $M_\odot$	$M_{clusters}$ 10^6 $M_\odot$	M_{large} 10^6 $M_\odot$	$Z_{cluster}$ $Z_\odot$	$V_{cluster}$ km s^{-1}	$D_{cluster}$ kpc	Notes
OFID	0.45	0.40	0.07	$10^{-2.0}$	45	9.8	
PM10/NFID	1.5	1.6	0.38	$10^{-2.0}$	59	13	
PM03	0.05	0.01	0.01	$10^{-2.0}$	76	16	
PM30	4.5	4.8	1.9	$10^{-2.0}$	63	15	
PE1	1.5	0.9	2.8	$10^{-3.0}$	17	5.0	*
PE5	1.5	2.3	0.37	$10^{-2.5}$	72	17	
PE20	1.5	0.9	0.66	$10^{-2.2}$	41	9.6	
PE30	1.5	0.8	0.82	$10^{-2.0}$	53	12	
PZC8	1.5	1.2	0.32	$10^{-2.0}$	60	13	
PZC15	1.5	2.2	0.96	$10^{-2.0}$	130	29	
PZS10	1.5	2.3	0.37	$10^{-1.5}$	72	18	
PR21	1.5	0.7	0.64	$10^{-3.0}$	41	8.9	
PR66	1.5	2.1	0.48	$10^{-2.0}$	45	13	
PR120	1.5	0.75	0.19	$10^{-3.0}$	14	5.0	*
PC32	1.5	1.8	0.54	$10^{-2.0}$	62	14	
PC73	1.5	1.5	0.28	$10^{-2.0}$	58	13	*

slightly metal deficient. However, dense clusters are also always formed outside of the dark matter potential.

4.3 Observational Signatures

The suite of simulations described above shows that over an extremely wide range of parameters, the ultimate consequence of the interaction between a galactic outflow and a primordial minihalo is the rapid formation of dense clusters containing up to a few $10^6 M_\odot$ of stars. While such high-redshift clusters are not directly observable with current telescopes, their rapid bursts of star formation and consequent low mass-to-light ratios present a opportunity for

study with the next generation of instruments. At the same time, their compact nature and formation in low-density environments makes it likely that many of them may have survived to the present, allowing for indirect connections with current stellar populations. Here we explore both of these connections.

Direct Observations

To calculate the direct observability of the clusters formed in our simulations, we first constructed an estimate of the number of stars formed as a function and time and position. As there is no explicit prescription for star formation included in our simulations, we instead built up the star-formation history by post-processing our outputs, carrying out the following steps:

1. First we calculated the total stellar mass in a series of 175 evenly-spaced bins, adding together the mass in cells that exceeded a density threshold of $\rho_{\rm th} = 1.0 \times 10^{-23}$ g cm^{-3}. Note that as the mass collapses dramatically onto the x axis, its final density is limited by the resolution in the y and z directions. Thus the threshold is less than the density of the collapsed cloud in nature, and it was determined by examining the late stages of our fiducial model and finding the apparent edge of the ribbon of material. In this way the collapsed mass was computed for every simulation output, such that we computed the masses and position of the stars as a function of time throughout the simulation. It should be noted that the masses quoted below are assume that the star formation efficiency is 100 percent, and therefore the quoted stellar mass and stellar flux are an upper limits.

2. Next, we used the positions and velocities to correlate the stellar distribution at each output with the distribution at the previous output. Starting with with the final output, and working back through the files in

this way, we calculated the mass of new stars formed as a function of time and determined the positions of these stars at the final output time.

3. Finally, we calculated the stellar fraction as a function of age for each of the mass bins at the final output time.

Using this information, we could then estimate the emitted flux for an arbitrary set of narrow or wide band filters. At redshifts $z \geq 8$ the *James Webb Space Telescope (JWST)* will be the best telescope to see these objects in wide band filters. From the ground, the best method of detection is to search for redshifted Lyman alpha (Lyα) emission using near-infrared capabilities of next generation, 30-40 meter class telescopes such as the *Giant Magellan Telescope (GMT)*, the *Thirty Meter Telescope (TMT)*, and the *European Extremely Large Telescope (E-ELT)*.

To determine the broad-band fluxes of our stellar clusters, we used the population-synthesis code bc03 (Bruzual & Charlot 2003) to compute the luminosity per solar mass of a stellar population as a function of frequency and age, and convolved this with the stellar history of each bin, and related this to the flux at an observed frequency ν_0 as

$$F_{\nu_0} = \frac{(1+z)}{4\pi d_l^2(z)} \int dt \frac{dL_\nu}{dM_*}\left(\frac{\nu_0}{1+z}, t\right) \frac{dM_*}{dt}(t) \quad \text{ergs cm}^{-2}\ \text{Hz}^{-1}\ \text{s}^{-1}, \tag{4.14}$$

where z is the shock redshift, $d_l(z)$ is the luminosity distance, $\nu_0/(1+z)$ is the rest-frame frequency, c and $dL\nu/dM_*(\nu_0/(1+z), t)$ is the luminosity per frequency per solar mass of a population of stars with an age t, and $dM_*/dt(t)$ is the star formation history in a given bin.

Similarly, we estimate the Lyman alpha flux from our simulations as

$$F_\alpha = \frac{1}{4\pi d_l^2(z)} \int dt \frac{dL_\alpha}{dM_*}(t) \frac{dM_*}{dt}(t), \tag{4.15}$$

where $dL_\alpha/dM_\star(t) = c_L(1 - f_{\rm esc})Q(H)M_*$, is the the Lyman alpha luminosity per solar mass of a population of stars with an age t (*e.g.* Scannapieco *et al.* 2003), with $c_L \equiv 1.04 \times 10^{-11}$ ergs, $f_{\rm esc}$ is the escape fraction of ionizing photons and is taken to be 0.2, $Q(H)$ is the hydrogen ionizing photon rate in units of number per second per solar mass and is taken from the stellar population synthesis code STARBURST99 (Leitherer *et al.* 1999). Finally, in both the broad and narrow band cases we normalized the flux by the spacing of each bin to get the flux per (physical) kpc.

Figure 4.16 shows the resulting fluxes for three different *JWST* bands (F115W, F150W, and F200W) and the Lyman alpha flux from a selection of simulations spanning a wide range of parameter space. Again we note that the fluxes in this figure are computed assuming that all the gas collapsed above $\rho_{\rm th} = 1.0 \times 10^{-23}$ g cm^{-3} is converted into stars, and so these fluxes should be scaled by an unknown star formation effciency factor which is ≤ 1. Likewise the angular given in this figure assume that that stellar clusters are being viewed edge on, such that angular separation is maximal. Table 4.3 summarizes the observable properties of the stellar clusters generated in all of our models including the total fluxes in the *JWST* bands and Lyα and the physical and maximal angular scales. Note that the physical and angular scales given are for the extended emission expected at the end of each simulation and not from the final globular cluster.

From the values in this figure and table we see that, unfortunately even the wide band filters of *JWST* are not expected to have the required sensitivity to detect these objects. Observations with *JWST* wide band filters will have typical sensitivities of 10-20 nJy for a 10-σ detection at 10,000 seconds of integration time (Stiavelli *et al.* 2008), which is roughly an order of magnitude

higher than the typical fluxes of ≈ 1 nJy (see Figure 4.16) expected from our objects.

On the other hand, the narrow band Lyα fluxes are over an order of magnitude *brighter* than those expected to be obtained with the next generation of ground-based telescopes. The proposed *Near Infrared Multi-object Spectrograph (NIRMOS)* on the *GMT* for example, will be able to detect such sources down to a flux limit of 1.0×10^{-20} ergs/s/cm^{-2}, given 25 hours of integration time (McCarthy 2008; GMT Science Case). Similarly, the *InfraRed Imaging Spectrometer (IRIS)* on the *TMT* will detect Lyα sources at z = 7.7 with fluxes of 1.0×10^{-18} ergs/s/cm^{-2} with signal-to-noise (S/N) of 15 in only 1 hour of observation time (Wright & Barton 2009; TMT Instrumentation and Performance Handbook). Finally, *OPTIMOS-EVE (Optical-Near-Infrared Multi-object Spectrograph)* for the *E-ELT* will detect sources with fluxes of 10^{-19} erg/s/cm^{-2} with S/N of 8 in 40 hours of integration time (Hammer *et al.* 2010). This means that most of our models are bright enough to be detected.

Beyond being bright in Lyα, the unusual, elongated morphology of the stellar distributions formed in outflow-minihalo interactions makes them ideal for study with next generation of ground-based instruments. With expected angular resolutions of $0.1 - 0.3$ arcsec (McCarthy 2008; Wright & Barton 2009; Hammer *et al.* 2010), next generation narrow band images will not only be able to detect the presence of the stars, but show that their distribution is highly-elongated in the direction of the impinging outflow, as illustrated in Figure 4.17. Furthermore, as the starburst galaxies triggering star-formation should have typical solar masses $\gtrsim 10^8 M_\odot$, these will be easily detectable with broad-band *JWST* measurements. Thus, the detection of a group of elongated Lyα emitters which whose axes point directly at a larger broad-band detected

Table 4.3: Summary of simulated model fluxes. F115W is the total flux from the F115W *JWST* band in units of nJy, Ly_α is the total Lyman α flux in units of ergs/s/cm^2, and the third and fourth columns are the maximum angular and physical spatial scales respectively.

Model	F115W	Ly_α	arcsec (")	kpc
OFID	0.25	9.2e-19	0.27	1.3
NFID	1.02	2.8e-18	0.28	1.4
PM03	0.02	2.3e-20	0.14	0.7
PM30	2.7	3.0e-18	0.55	2.7
PE5	1.3	1.2e-18	0.65	3.2
PE20	0.54	6.1e-19	0.16	0.76
PE30	0.40	4.6e-19	0.08	0.39
PZC8	0.53	5.4e-19	0.24	1.2
PZC15	2.1	2.3e-18	0.46	2.3
PZS10	0.89	8.9e-19	0.68	2.9
PR21	0.35	4.0e-19	0.05	0.25
PR66	0.47	2.3e-19	0.54	2.7
PC32	0.99	8.5e-19	0.27	1.3
PC72	0.68	7.2e-19	0.30	1.5

starbursting galaxy will provide a unique signature that unambiguously points to the formation of compact stellar clusters by high-redshift galaxy outflows.

Other Hydrogen Lines

In the previous section, we estimated the observational signature for a selection of simulations in a variety of JWST NIRCam filters as well as Lyα line flux. In this section, we further this study by including estimates of H_α and H_β, two additional hydrogen lines that are expected to be bright as these clusters form. We follow the same procedure in estimating H_α and H_β as for Lyα and evaluate the luminosity per mass of each new line according to,

$$dL_{line}/dM_\star(t) = c_x Q(H) M_*, \tag{4.16}$$

where Q(H) is the number of ionizing photons per unit solar mass, calculated using STARBURST99, at a time t and c_x is 1.21×10^{-12} ergs and 4.47×10^{-13}

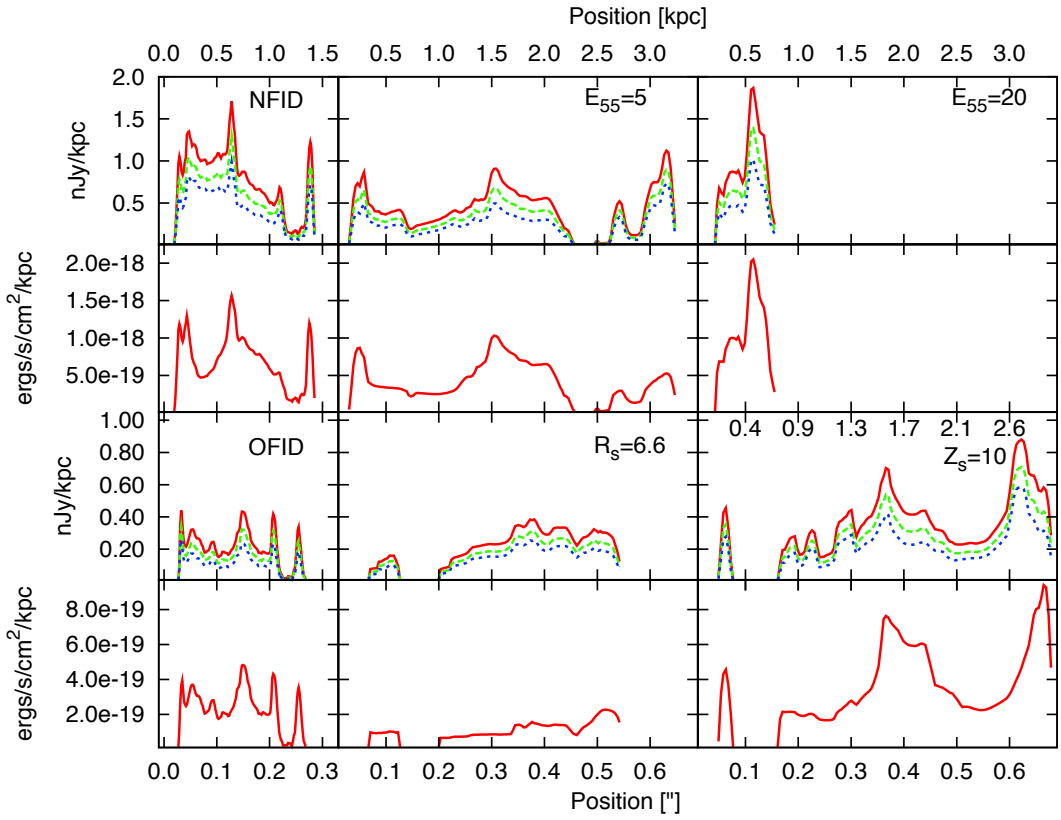

Figure 4.16: Simulated fluxes from selected models, scaled to 100% star formation efficiency. The top two rows show the simulated fluxes for runs NFID, PE5, and PE20 (from left to right), while the bottom two rows shows the simulated fluxes for runs OFID, PR66, and PZS10. The first and third rows show the expected fluxes in *JWST* wide band NIRCam filters. The (red) solid lines are fluxes in the F115W band, the (dashed) green lines are in the F150W band, and the (dotted) blue lines are in the F200W band, all measured in nJy per kpc. The second and fourth rows show the expected Lyα intensities and are measured in ergs/s/cm^2/kpc. The top x-axis is the physical spatial scale measured in kpc of each model while the bottom x-axis is the angular scale measured in arcseconds. The y-axis is identical across a given row.

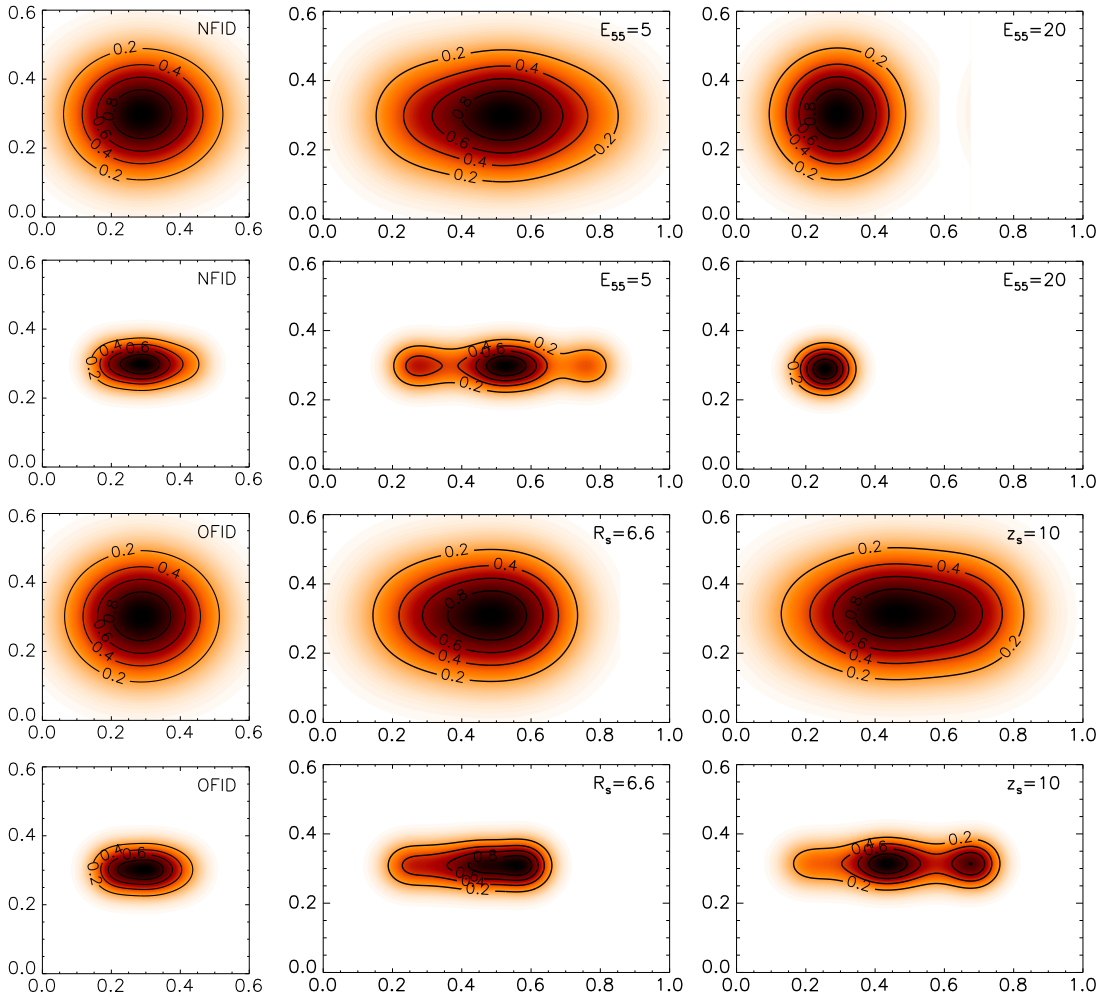

Figure 4.17: Simulated narrow-band images from selected models. The top two rows show simulated images for runs NFID, PE5, and PE20 (from left to right), while the bottom two rows shows the simulated images for runs OFID, PR66, and PZS10. The first and third rows show forming clusters as observed edge-on with 0.25 arcsecond resolution, and the second and fourth rows show clusters as observed edge-on with 0.1 arcsecond resolution. In each panel the x and y axes are in units of arcsec, and the contours are labeled according to flux per unit area relative to the maximum flux per unit area in the image.

ergs for H_α and H_β respectively (Schaerer 2002). In contrast to Lyα, we assume that all the emission from these lines escape from the forming stellar clusters.

Figure 4.18 shows these updated line intensities. The first and third row of this figure remains unchanged from Figure 4.16 while the second and third rows are updated to include the expected line intensities from H_α (solid green lines) and H_β (solid blue lines). The reference wavelength for H_α is 6562 Å and is redshifted to 5.9 μm, which puts it into the wavelength range of the Mid-Infrared Instrument (MIRI) on *JWST*. Unfortunately, the sensitivity ($\sim 10^{-18}$ ergs/s/cm^2 at this wavelength) is too high for reasonable exposure times. The reference wavelength for H_β is slightly shorter 4861 Å which corresponds to an observed wavelength of 4.4 μm and, like Lyα, falls within the NIRSpec wavelength range. However, the sensitivity ($\sim 3\times10^{-19}$ ergs/s/cm^2 at this wavelength) is also too high to reasonably capture the H_β emission from these objects.

Therefore, our original conclusions remain the same for the ability to observe these high redshift clusters. And although the emission of H_α and H_β is fairly bright in these objects, they fall below the detectability limits of the instruments on *JWST*. The ability of the proposed large ground-based Lyα imaging remains the best possibility for direct observation.

4.4 Conclusions

In the last chapter of our minihalo/galaxy outflow study, we look at the robustness of our initial results by performing a parameter study over our model parameters and estimate the observability of these stellar clusters. We find that in almost all cases considered the results compare very well with those presented in previous chapters. In general, the minihalo gas is transformed into a ribbon of material with at least one embedded dense stellar cluster. In addition, most of these clusters are found outside of their parent dark matter halo.

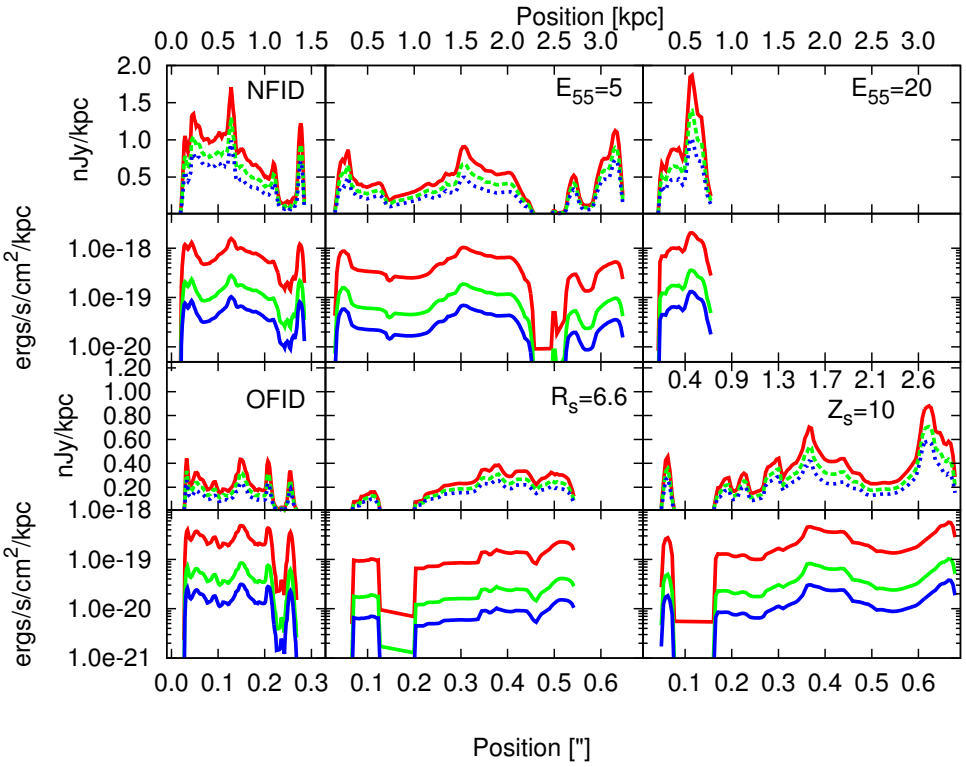

Figure 4.18: Simulated fluxes from selected models, scaled to 100% star formation efficiency. The top two rows show the simulated fluxes for runs NFID, PE5, and PE20 (from left to right), while the bottom two rows shows the simulated fluxes for runs OFID, PR66, and PZS10. The first and third rows show the expected fluxes in *JWST* wide band NIRCam filters. The (red) solid lines are fluxes in the F115W band, the (dashed) green lines are in the F150W band, and the (dotted) blue lines are in the F200W band, all measured in nJy per kpc. The second and fourth rows show the expected Lyα intensities as the solid red lines, H_α as the solid green lines, and H_β as the solid blue lines and are measured in ergs/s/cm^2/kpc. The top x-axis is the physical spatial scale measured in kpc of each model while the bottom x-axis is the angular scale measured in arcseconds. The y-axis is identical across a given row and is now given logarithmically to differentiate between the given line intensities.

Furthermore, we estimate the expected star formation as these dense clusters form. Using simple stellar population synthesis models we estimate the expected broad-band fluxes in a series of *JWST* filters as well as the Ly-α line intensity. While the next generation of ground-based Ly-α imaging looks very promising, the sensitivity of the *JWST* bands is too low for the cases considered.

In general, the primordial minihalo/galaxy outflow interaction produces a series of compact, dense stellar clusters that are free from their dark matter halo. It is to be expected that some of the star formed during this interaction will survive to the present day. In the next chapter, we will discuss a possible low-redshift analogues for these clusters.

Chapter 5

Source of Halo Globular Clusters?

In Chapters 2-4, we showed that a general outcome between primordial minihalos and galaxy outflows is a population of small, dense stellar clusters embedded within a ribbon of material. In fact the clusters in our simulations are very dense (n $\sim 10^2$ cm^{-3}) and expected to become gravitationally bound to larger structures that form over cosmological time. The vast majority of these clusters are also free from their parent dark matter halos. Over a large range of parameter space, these clusters will be found in low-density environments in which disruption processes are minimal. Thus it is likely that a substantial fraction of the clusters generated by outflow-minihalo interactions may persist even to the present day. A natural low-redshift counterpart of these compact, high-redshift clusters may be the population of halo globular clusters.

How globular clusters are formed has been an open question since their discovery. The typical age of a globular cluster is between 10-13 Gyrs (Krauss & Chaboyer 2003), which demands a cosmological origin. Observations of globular clusters have found a bimodal color distribution that suggests two subpopulations (Zepf & Ashman 1993). The relatively metal rich population with $\left[\frac{Fe}{H}\right] \approx -0.5$ are associated with the thick disk or bulge of galaxies and are thought to have formed as a consequence of galaxy interactions during the build-up of their parent galaxy (Shapiro *et al.* 2010; and see Brodie & Strader 2006 for a review). On the other hand, the metal-poor population with $\left[\frac{Fe}{H}\right] \approx -1.6$ are associated with galaxy halos and are thought to form in the early universe through an unknown mechanism.

Formation scenarios for such clusters are typically split into two groups: 'pre-enrichment' and 'self-enrichment' schemes. In the pre-enrichment picture,

the primordial gas is homogeneously enriched via supernovae in such a way that does not disrupt the cloud (*e.g.* Beasely *et al.* 2003; Bromm & Clarke 2002; Elmegreen & Efremov 1997; Marcolini *et al.* 2009). However, little is known about this previous generation of stars, how it was able to enrich the gas so quickly, and why it played only a secondary role in the formation of globular clusters. In the self-enrichment picture, the primordial gas is enriched by a supernova contained within the halo hosting the forming globular cluster (*e.g.* Boley *et al.* 2009; Brown *et al.* 1995; Recchi *et al.* 2005; Smith 2010). This has the problem of not being able to mix the metals into the cluster rapidly enough, as well as usually leads to the the supernova unbinding the cluster (Peng & Weisheit 1991; Whalen *et al.* 2008b). Finally, Cen (2001) set aside the question of enrichment completely and used a simple model to suggest that ionization fronts can act as an external force to collapse these clouds. However, many others (*e.g.* Haiman *et al.* 2001; Illiev *et al.* 2005; Shapiro *et al.* 2004) showed that instead of forming a dense cluster, the ionization front completely boils away the minihalo. As shown in our simulations, interactions between galaxy outflows and minihalos share the best aspects of all these scenarios: bringing in metals only moments before vigorous star formation commences, depositing the metals without unbinding the proto-globular cluster, and triggering collapse without evaporating the cloud.

Observationally, there are three important properties of halo globular clusters that make this connection a promising one. First, globular cluster masses are distributed as a Gaussian with a mean value of $10^5 M_\odot$ and a dispersion of 0.5 dex (*e.g.* Armandroff 1989). Here, the lower mass cut-off in this population is likely to be due to a variety of destruction processes including mechanical evaporation (*e.g.* Spitzer & Thuan 1972) and shocking as the cluster

moves through the disk of the galaxy (*e.g.* Ostriker *et al.* 1972), but the high-mass cut-off appears to be a property of the initial population. Except for the models with the smallest minihalo masses, all of our models produce at least one dense cluster with a mass between 10^5 and a few times 10^6 $M_\odot$. Furthermore minihalos have an intrinsic maximum mass of $\approx 10^7\,M_\odot$ which corresponds to the $T \approx 10^4$ K limit where atomic hydrogen/helium cooling becomes inefficient, and thus the maximum sizes of compact clusters in our study are likely to place a rough upper bound on the masses of stellar clusters that can be formed by this mechanism in nature.

A second important property connecting our high-redshift clusters with the present-day population of halo globular clusters is the abundances of stars both within a given cluster and between different halo globular clusters. The metallicity distribution between clusters is well defined by a Gaussian distribution with a mean value $\left[\frac{Fe}{H}\right] \approx -1.6$ and with a dispersion of 0.3 dex (Zinn 1985; Ashman & Bird 1993). Most individual clusters have a dispersion of less than 0.1 dex (see Suntzeff 1993 and references within), although it is worth noting that some of the clusters that show larger scatter may be due to subsequent star formation and enrichment due to evolved stars (*e.g.* Piotto *et al.* 2007; D'Ercole *et al.* 2008; Bekki 2011).

In our simulations, the metals from the incoming outflows are well mixed into the primordial gas from the minihalo through the turbulent processes that are inherent to this interaction. Over a wide range of parameters, the metal-free gas is enriched to a nearly constant value of $Z \approx 10^{-2}$ $Z_\odot$, which approximately matches the observations. Only a small subset of models is found where the metal abundance is below this value. In cases where the halo is very close to the galaxy, the minihalo is crushed before an appreciable abundance of metals is

transported into the primordial gas. If the halo is too far away from the galaxy then there is ample time for metals to move into the cloud, but the shock is too deficient to enrich to the fiducial level. In most models there is some slight difference in the metal abundance especially for the gas originally found near the center of the dark matter halo. Otherwise, it seems that metal enrichment in these situations is fairly uniform and robust around a value of $\approx 10^{-2}$ $Z_{\odot}$.

Note that our sub-grid turbulence model keeps track of the velocity, $\sqrt{2K}$, and eddy turnover scale, L, of buoyancy-driven and shear-driven turbulence, and assumes that below these lengths scales the flow will behave as fully developed turbulence. In this case, as studied in detail in Pan *et al.* (2010), the mixing of metals is driven by a cascade process similar to that of the velocity field. Using direct numerical simulations, Pan *et al.* (2010) showed that over a large range of Mach numbers which span the values in our in shock minihalo interactions, metals are mixed in on a time scale which is close to the time scale for energy decay, and that the dependence of this mixing time on the length scale at which pollutants are injected is also consistent with this cascade picture.

Thirdly, the observation that globular clusters do not reside within dark matter halos provides a strong constraint on their formation. Such observations show that tidal forces are actively stripping more stars from globular clusters (Irwin & Hatzidimitriou 1993; Grillmair *et al.* 1995) than would be expected if housed within dark matter halos (Moore 1996; Conroy *et al.* 2011). This too is a robust prediction of our model, and in only in a small subset is there any gas left in the dark matter halo. In fact, only in runs with the largest halo mass, the largest concentration, and at the largest separations between minihalo and the starburst galaxy was gas retained by the minihalo, and in all these cases at least one other cluster was formed that was unbound from the halo. Thus outflow

minihalo interactions are a mechanism that primarily, but not exclusively produces dark-matter free clusters. Presumably these rare clusters would still be found with their dark matter halos if they have not been stripped away by some other means or buried within the center of large, low-redshift galaxies.

Globular cluster formation has also been studied using simulations of the hierarchical buildup of a Milky Way sized galaxy. Kravtsov *et al.* (2005) carried out one such a simulation and found that proto-globular clusters are produced in giant molecular clouds within the disk of the galaxy. While this model reproduced many of the properties expected of halo globular clusters, it relied on subsequent violent mergers to move these clusters to the galaxy halo. Muratov & Gnedin (2010) looked at a similar mechanism that reproduces the observed metallicity distributions found in globular clusters. Griffen *et al.* (2010) examined a halo from the Aquarius simulation for sites of globular cluster formation, and adopted a simple model in which the cluster sites are determined solely on their temperature. Cluster formation is ended when the host galaxy is completely reionized. They were able to reproduce the expected number of present day clusters, their positions, and formation ages. However, since their simulation used only dark matter particles, no mention was made of how the baryonic matter is removed from the dark matter halo or how the metallicity of the resulting cluster arises. On the other hand, the minihalo-galaxy interactions studied here are both a natural consequence of hierarchical galaxy formation, and they reproduce the masses, metallicities, and dark matter content of halo globular clusters directly in our simulations.

Chapter 6

Conclusions

The early universe was permeated by primordial minihalos that provided the building blocks for larger structures. However, since they were not massive enough to form stars efficiently on their own, these minihalos largely remain as passive objects until until acted on by an outside influence. This means that first galaxies formed in somewhat larger dark-matter halos, in which atomic cooling is efficient, formed stars, some of which went supernovae, and funned a fraction of the resulting energy into massive galaxy-sized outflows. For minihalos in orbit around these early galaxies, such outflows may have triggered a radical transformation.

Previous work has used ionization fronts to create these conditions (Cen 2001), however, 3D hydrodynamic simulations show that for either a stellar or quasar source, instead of creating clouds of H_2, the cloud is completely photo-evaporated (Iliev *et al.* 2005; Shapiro *et al.* 2006). However galactic outflows are another option for triggering star formation. Shocks not only provide the conditions for non-equilibrium chemistry without completely destroying the cloud, but also serve as a source of metals.

In Chapter 2, we implement a nonequilibrium chemistry and cooling package within FLASH to properly model the minihalo/galaxy outflow interaction. This network traces collisional ionization and recombination of hydrogen and helium as well as the formation of two primary coolants in the absence of metals: H_2 and HD. I have also included the impact of a dissociating background on these rates and implemented routines that control the cooling of gas in the presence atomic and molecular line cooling.

The shock fulfills two important roles. First, it ionizes the neutral gas found in the minihalo, which recombines and begins to form H_2 and HD, through nonequillbrium processes. These coolants allow the cloud to cool to much lower temperatures, triggering star formation. Secondly, the shock imparts momentum into the gas and accelerates it above the escape velocity. This creates a cloud of dense, cold molecular gas that is free from dark matter halos which are identified as proto-halo globular clusters.

In Chapter 3, we looked at the effect metals have on this cosmological interaction. The suggestion that this type of interaction can provide a formation scenario for halo globular clusters hinges on whether or not the metals from the galaxy outflow can be efficiently mixed into the primordial gas. To model this properly, we have implemented a sub-grid turbulence model that tracks the mixing between the outflow and minihalo gas. In addition, we have included metal-line cooling into our overall cooling function.

We found that for our fiducial model we reproduce most of the final features found in our initial study. Most of the minihalo gas has been removed from the parent dark matter halo and is found as a ribbon of material with several dense embedded stellar clumps. We also find that most of the minihalo gas is enriched to uniform levels throughout the ribbon, consistent with that found in observations of halo globular clusters. Thus, the shock fulfills another important role in providing a reservoir of metals with in which to enrich the minihalo gas.

Taken together, the results from these two studies suggest that the minihalo/galaxy outflow interaction is a promising mechanism for the formation of proto-halo globular clusters. In Chapter 4 we complete this picture and perform a large, medium-resolution parameter study, quantifying the impact of

minihalo mass, minihalo formation redshift, outflow energy, outflow redshift, distance, minihalo concentration, and spin. For a wide range of parameters, the results are extremely similar. The baryonic matter is expelled from the dark matter halo and formed into at least one dense, cold cluster that is homogeneously enriched with metals. In fact only under extreme circumstances, such as a large separation between the halo and the galaxy, very low energy outflows, or very high minihalo concentration, is gas retained by the minihalo, and even in these cases at least one other compact, unbound cluster is formed.

Furthermore, our parameter study strengthens the idea that the longest lived stars formed by these processes will be observable today as members of halo globular clusters. Like the clusters in our simulations, such globular clusters are observed over a substantial mass range, and their upper mass limit can be directly associated with the maximum minihalo mass, above which atomic cooling becomes efficient. Over a wide range of energies, redshifts, and distances, outflows are able to accomplish three important jobs necessary to form realistic halo globular clusters: imparting the momentum required to move the pristine gas from the dark matter halo, starting the non-equilibrium chemistry and cooling required for collapse, and providing a source of metals. Turbulence then mixes these metals into the primordial gas nearly homogeneously.

Additionally, we can estimate the number of primordial minihalos that should exist in a region that will evolve into a galaxy system like the Milky Way. This region is filled with $\sim$ 1000 minihalos, at a z_c=15 and nearly 3000 by z_c = 10 which can be turned into clusters with stellar masses of $> 10^5$ $M_\odot$. By assuming the above cosmological parameters (with a primordial power spectrum from Eisenstein & Hu 1999; $\sigma_8 = 0.87$) and if we assume that 20% of the gas in the minihalo is converted to stars and 50% of the remaining gas is ejected, the

region will have $\sim$ 1000 at z_c=15 and nearly 3000 at $z_c = 10$. These are estimated using the progenitor model from Lacey & Cole (1993) and assuming a final mass and formation redshift of 2×10^{12} $M_\odot$and $z_f = 2$. Even assuming the mean cosmological background gives $\sim$ 500 and $\sim$ 2000 minihalos at $z_c = 15$ and 10, respectively (Press & Schechter 1974).

Only a small percentage of the minihalos formed are expected to undergo the interaction described. However, a general result of our investigation is that in a single interaction multiple proto-globular clusters are formed. Of the $\sim$ 150 known globular clusters around the Milky Way roughly 50 percent are from the halo globular cluster population (Mackey & Gilmore 2004). Therefore, this interaction does not need to be particularly efficient to explain the population of halo globular clusters that we see today.

While the direct detection of outflow-minihalo interactions is beyond current capabilities, it will be well within the reach of the telescopes currently being planned. Post-processing our simulations we show that the outflow-driving galaxies are likely to be detectable in broad-band *JWST* images, but the clusters themselves are likely to be just beyond their expected detection limits. On the other hand, narrow-bound imaging of redshifted Lyman alpha emission from these forming clusters will be well within the capabilities of large ground-based telescopes like the *GMT*, *TMT*, and *E-ELT*. Such Lyα emitters will appear as bright, extended in a single direction, and pointed directly at larger broad-band detectable starbursts. This unique signature makes them perfect targets for the next generation of telescopes and an exciting observational probe of an extraordinary mode of high-redshift star formation.

Chapter 7

Other Work

Once primordial gas is enriched with an amount of metals, chemistry and cooling avenues for the gas changes dramatically. In particular, the number of molecules that are possible increase from a small handful (*e.g.* H_2) to many hundreds (*e.g.* CO, OH, etc). Therefore, objects are enriched with metals can cool to lower temperatures and form denser structures and may lead to additional star formation. In particular, low metallicity dwarf galaxies (see Tolstoy *et al.* 2009 for a review) are the intuitive object to study the link between high redshift primordial star formation and present day, highly enriched objects.

Dwarf galaxies represent a unique laboratory to study star formation. The specific star formation in dwarf galaxies are just as intense as that seen in larger spiral galaxies without the expected dynamical causes (*e.g.* spiral arms and bars) (*e.g.* Vanzi *et al.* 2009). The nature of star formation within these galaxies is poorly understood, although mergers and tidal interactions are possible mechanisms (*e.g.* Cumming *et al.* 2008; James *et al.* 2010). In addition, the metallicity of these galaxies is lower relative to larger star forming galaxies that may provide insights to star formation during earlier formation epochs (Meier *et al.* 2002).

NGC 5253 represents a prime example of such a galaxy. It is a companion galaxy to M83 and is nearby at a distance of 3.8 Mpc (Gibson *et al.* 2000). Recent observations have uncovered multiple "super-star clusters". Which are very bright with $L_{IR} \sim 10^9 L_\odot$ (*e.g.* Gorijian, Turner, & Beck 2001) and $M_V \sim$ -10 to -11 (Meurer *et al.* 1995; Gorjian 1996). In addition, radio observations of CO(2-1) emission coincident with a dust lane and with properties consistent with inflow (Meier *et al.* 2002).

However, the nature of the starburst and how large a part the infall plays remains an open question.

A natural extension of the work described in Chapters 2-6 to model this type of interaction. By using a "low"-redshift chemistry network, we will model the chemical makeup of a cold stream as it falls toward the center of a dwarf galaxy. Additionally, we will model the expected CO emission and compare with radio observations.

7.1 Chemistry

The gas phase chemistry of enriched gas can be quite complex with up to thousands of individual reactions between hundreds of species comprising a handful of elements (*e.g.* Le Teuff *et al.* ; Semenov *et al.* 2010). While such large networks are important for the study of the interstellar medium (ISM), they are impractical when coupled with large hydrodynamical simulations due to their long computation time. We therefore use a substantially smaller network that tracks and evolves the atomic and molecular species most important in the thermodynamics of our system.

Implementation

We have implemented the chemical network presented in Glover *et al.* (2010; hereafter G10). This network tracks the evolution of atomic hydrogen (H, H^+, H^-), atomic helium (He, He^+), atomic carbon (C, C^+, C^-), atomic oxygen (O, O^+, O^-), molecular hydrogen (H_2, H_2^+, H_3^+), molecular carbon (C_2), molecular oxygen (O_2, O_2^+), as well as molecules containing combinations of these elements (OH, OH^+, CO, CO^+, CH, CH^+, CH_2, CH_2^+,CH_3^+, HCO^+, HOC^+, H_2O, H_2O^+, H_3O^+) and, finally, electrons (e^-). In total there are 32 species among 218 separate reactions.

In addition to gas phase collision reactions, this network includes the effect of an ambient ultraviolet (UV) radiation field and cosmic rays. The photochemical rates assume a standard interstellar radiation field from Draine (1978) which has a field strength of $G_0 = 1.7$ in Habing (1968) units. We introduce a coefficient, $\mathrm{J}_{21} \equiv G/G_0$ that allows me to alter this background field, assuming that the field scales linearly with G_0. For example, a $\mathrm{J}_{21} = 0$ removes the background field while a value of $\mathrm{J}_{21} = 1.0$ is the standard Habing field. In this manner, the background UV field can be changed and used as a free parameter. Similarly, we use the parameter ξ_H to alter the background cosmic ray ionization rate. Finally, many of these rates are dependent on the on the visual extinction between the ionizing source and position of the gas. For simplicity we treat this extinction as another free variable throughout the simulation volume.

The binding and ionization energies of each species is important for the overall energy budget of the gas. We therefore assign each species with a energy,

$$E_v \equiv B.E. - I.E, \tag{7.1}$$

which is simply the ionization potential subtracted from the binding energy. These values are summarized in Table 7.1.

The method of solving these equations is the same as in Chapter 2. A Kaps-Rentrop (or Rosenbrock) method is used to advance the species abundances forward in time. In addition to the internal solver subcycling, based on the relative difference between third and fourth order solutions, we also subcycle the chemistry solver based on the fractional species change. This allows use to run the chemistry solver at the hydrodynamic time step rather than a chemical time step.

Table 7.1: Summary of species data. The first column gives the species name, the second column is the ionization potential, third is the dissociation energy, fourth is E_v, and the last column is the ratio of specific heats γ. All energies are given in units of eV. Those species denoted with a single asterisk do not have published dissociation energies. Finally, HOC^+does not have any published ionization or dissociation energies, however, we assume they are the same as HCO^+, which we denote with the double asterisk.

Species	I.P (eV)	D.E (eV)	E_v (eV)	γ	
H	0.00	0.00	0.00	1.66	
H^+	13.60	0.00	-13.60	1.66	
H^-	0.00	0.77	0.77	1.66	
He	0.00	0.00	0.00	1.66	
He^+	24.60	0.00	-24.60	1.66	
C	0.00	0.00	0.00	1.66	
C^+	11.27	0.00	-11.27	1.66	
C^-	0.00	1.26	1.26	1.66	
O	0.00	0.00	0.00	1.66	
O^+	13.60	0.00	-13.60	1.66	
O^-	0.00	1.46	1.46	1.66	
H_2	0.00	4.48	4.48	1.40	
H_2^+	15.43	4.48	-10.95	1.40	
H_3^+	16.30	6.30	-10.00	1.31	
C_2	0.00	6.21	6.21	1.40	
O_2	0.00	5.12	5.12	1.40	
O_2^+	12.06	6.66	-5.40	1.40	
OH	0.00	4.39	4.39	1.40	
OH^+	13.00	5.10	-7.90	1.40	
CO	0.00	11.90	11.90	1.40	
CO^+	14.01	8.34	-5.67	1.40	
CH	0.00	3.47	3.47	1.40	
CH^+	10.64	0.00	-10.64	1.40	*
CH_2	0.00	4.00	4.00	1.31	
CH_2^+	10.40	4.00	-6.40	1.31	
CH_3^+	9.83	0.00	-9.83	1.31	*
HCO^+	9.88	0.00	-9.88	1.31	*
HOC^+	9.88	0.00	-9.88	1.31	**
H_2O	0.00	0.00	0.00	1.31	
H_2O^+	12.61	5.11	-7.50	1.31	
H_3O^+	0.00	0.00	0.00	1.31	*
e^-	0.00	0.00	0.00	1.66	

As the species evolve, the temperature of the gas changes due to the possible recombinations, ionizations, and dissociations experienced by the atomic and molecular species. In addition, the cooling from molecular species becomes important as they begin to form. Since both the reaction and cooling rates are temperature dependent, it is very important for both of these processes to remain coupled. Therefore, once a chemical subcycle is performed, the cooling routines are immediately called. This ensures the stability of both the chemistry and cooling routines.

Chemistry Test

To ensure that we are solving these coupled equations correctly, we use a procedure similar to that presented in Chapter 2 and in G10. In order to have a commensurate dataset to compare against, we use reaction rates given in the UMIST RATE06 database (Woodall *et al.* 2007). We restrict our attention to two body interactions in the absence of a background UV dissociating field and a cosmic ray field. Out of the 4604 reactions in RATE06 134 reactions were used that match the reactions given in G10.

We complete this complementary network by adding rates that appear in G10 and not in RATE06. In total, this gives a total of 144 reactions. In particular we add reactions for the positive-negative ion recombination of O^- and H^+ (Rxn 108), the formation of H_3O^+ from H_2 and H^+ (Rxn 141), the formation of H_2^+ from H^- and H^+ (Rxn 15), the formation of H_2^+ from H and H^+ (Rxn 4), the charge exchange reaction between H_2 and H^+ (Rxn 7), ion molecule reactions between H_3O^+ and H (Rxn 55), between O^+ and H_2 (Rxn 69), and between CO and He^+ (Rxn 105) and finally, the electron attachment of HCO^+ (Rxn 130).

Next, we compare the reaction rates presented in G10 to those in RATE06. First, we follow G10 and alter some of the rates used in that network to match those found in RATE06. Specifically, we change the dissociation of H_2 by H (Rxn 9) and of H_2 by H_2 (Rxn 10), the radiative recombination of H^+ (Rxn 12) and He^+ (Rxn 17), the formation of CO by CH and O (Rnx 38), the formation of O_2 by OH and O (Rxn 47), the formation of H_3^+ by H_2^+ and H_2 (Rxn 54), the dissociation of CO by He^+ (Rxn 104), the dissociative recombination of H_3^+ (Rxn 110-112), the dissociative recombination of H_2^+ (Rxn 120-122), and the dissociative recombination of H_3O^+ (Rxn 123-126).

To compare with the network in FLASH, we run a series of simple tests. We use the open source chemistry code *Astrochem* to run the RATE06 reaction network. Each model is computed as a single zone model where the density and temperature are kept constant. Models were run with the hydrogen number densities ranging between 10^{-2} to 10^6 cm^{-3} and temperatures ranging between 10^2 to 10^4 K. Each model is run for a total of 10^8 years. In each FLASH model, we start each model with a small initial time step ($\sim 10^5$ s) and allowed to increase to the hydrodynamic time step. The abundances of each species relative to hydrogen is: $n_{\rm He} = 0.08$, $n_{\rm C^+}= 8.2\times\ 10^{-5}$, $n_{\rm O^+} = 1.5\times\ 10^{-5}$, $n_{\rm H^+} = 0.99$, and $n_{\rm H} = 0.01$.

Figure 7.1 shows a the comparison between the derived chemistry network evolved with *Astrochem* and the FLASH network where the temperature is constant at 100 K and a hydrogen number density of $n_{\rm H} = 10^{-2}$ cm^{-3}. Each panel shows the abundances of a set of species through time. It is important to note that while the abundances change over many orders of magnitude through the evolution time, our FLASH values matches very well with the *Astrochem* network. At the temperature considered here, the ionized

species very quickly begin to recombine into their neutral state. However, even during this quick period a substantial amount of molecular species are created. At early times there is a slight discrepancy between FLASH and *Astrochem* that is simply due to slight differences in the initial conditions but quickly converge and by late times are almost indistinguishable.

7.2 Cooling

Radiative cooling in a gas with atomic and molecular species and with metals is quite complex. At temperatures $>10^4$ K the majority of the cooling comes from atomic hydrogen and helium, with bremmstrahlung radiation becoming important at temperatures above $>10^7$K. Below 10^4K, many cooling channels become important, primarily from atomic metal lines from carbon and oxygen, as well as molecular line cooling from H_2, CO, H_2O, and OH. In particular, carbon monoxide (CO) is important at temperatures below 200 K where molecular hydrogen (H_2) becomes inefficient (Smith *et al.* 2008).

Therefore, the total cooling function becomes,

$$\Lambda_{\rm Total} = \Lambda_{\rm H,He} + \Lambda_{\rm Molecule} + \Lambda_{\rm Metals} - \Lambda_{\rm Heating}, \tag{7.2}$$

where the total cooling function is simply the summation of the cooling rate from each cooling channel minus some terms relating to the heating of the gas. The introduction of carbon and oxygen into the chemistry network allows for the creation of many molecules that are very important for the thermal evolution of the gas. As we have expanded the chemistry network, we also expand the cooling routine to include these important coolants. Much of the cooling presented here follows from Glover *et al.* (2010), which we summarize here.

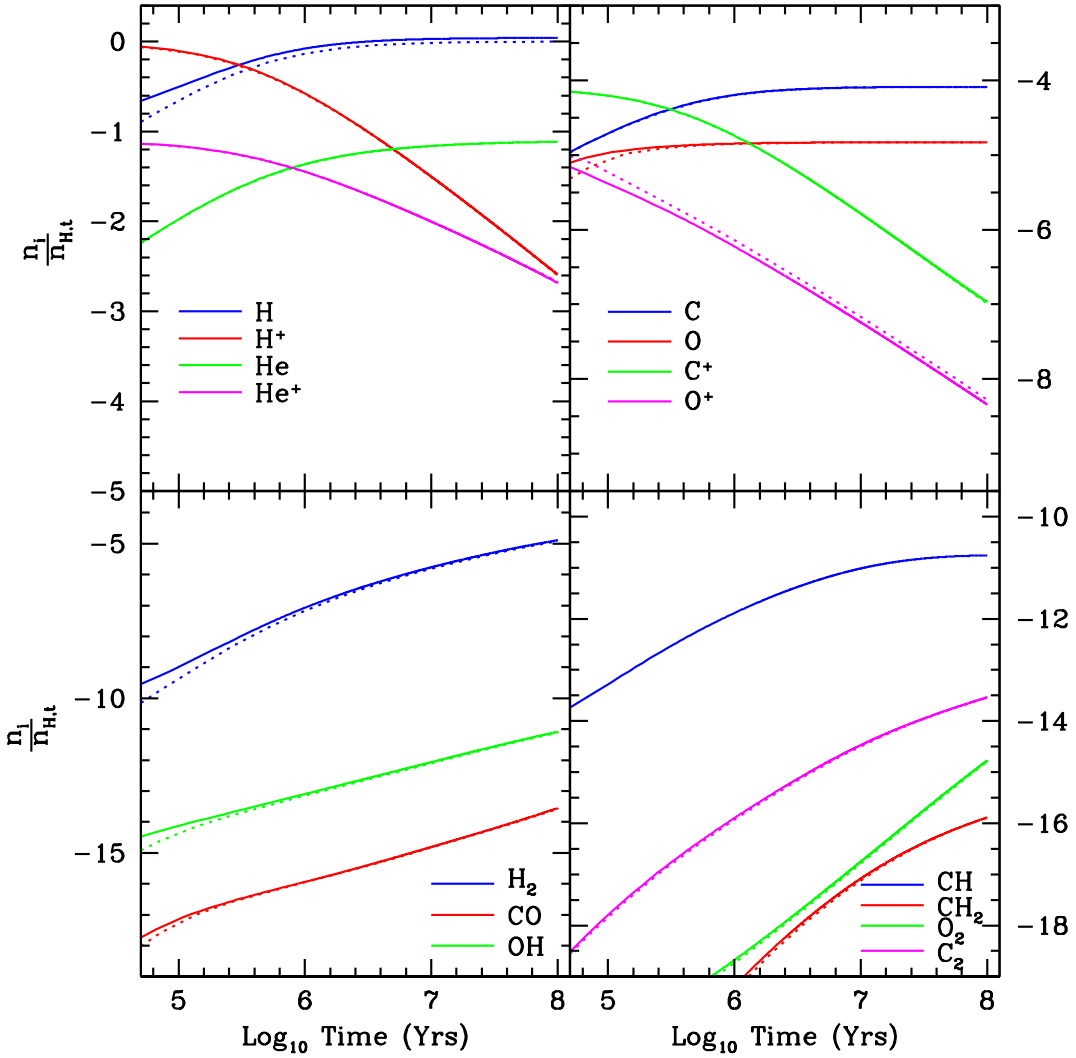

Figure 7.1: Comparison of chemical abundances between *Astrochem* and FLASH. In each panel the solid lines are the abundances from FLASH while the dashed lines are from *Astrochem*. The y-axis of each panel is the logarithm of time in units of years and the number density of the given species divided by the total number density of hydrogen. *Top Right:* The red lines show H^+, the blue lines show H, the magenta lines show He^+, and the green lines show He. *Top Left:* The red lines show O, the blue lines show C, the magenta lines show O^+, and the green lines show C^+. *Bottom Right:* The red lines show H_2, the blue lines show CO, and the green lines show OH. *Bottom Left:* The red lines show CH, the blue lines show CH_2, the green lines show O_2, and the magenta lines show C_2. In general, the solid and dashed lines overlap each other and become very hard to differentiate between them.

Atomic Line Cooling

The treatment of the high temperature hydrogen and helium cooling remains unchanged from CH1. The cooling rate is calculated using CLOUDY (Ferland *et al.* 1998) assuming only collisional ionization in the Case B limit.

Metal-Line Cooling

At temperatures below 10^4 K, cooling from metal lines comes primarily from neutral oxygen and carbon and from ionized carbon. To account for this cooling, we use the tabulated results from Weirsma *et al.* (2008). This cooling function assumes local thermodynamic equilibrium and assumes standard solar ratios. The total cooling is then scaled by the local metallicity. Finally, the radiative cooling rates are defined over a wide temperature range, from 10^2 to 10^9 K. The cooling rate at a given temperature is found through a simple table lookup.

Molecular Cooling

H_2 cooling

Much of the H_2 cooling rates are taken from Glover *et al.* (2008) and remain unchanged from CH1. Each cooling rate has the form:

$$\Lambda_{i,j} = n_i n_j \lambda_{i,j}, \tag{7.3}$$

where $\Lambda_{i,j}$ is the energy loss per volume due to species i and j, n_i and n_j are the number densities of each species, and $\lambda_{i,j}$ is the cooling rate in ergs cm^{-3} s^{-1}. Cooling rates for the collisional excitation between H_2 and H, H_2 , H^+ , and e^- and between H_2^+ and H or e^- , are taken from Glover *et al.* (2008).

CO and H_2O cooling

We follow G10 in implementing CO and H_2O cooling. Here they use the tabulated rotational cooling functions from Neufeld & Kaufman (1993) and

Neufeld, Lepp, & Melnick (1995). As above, the cooling rate is defined as a rate coefficient L, with units of erg cm^3 s^{-1} and defined such that the cooling rate per unit volume per unit time is defined as Λ=$Ln(H_2)n(M)$, where $n(H_2)$ is the number density of H_2 and $n(M)$ is the number density of the other coolant species.

The cooling rate coefficient is given as a function of the H_2 number density, the kinetic temperature, and parameter that relates the species number density to the local velocity field $\widetilde{N}(m)$, defined as:

$$\widetilde{N}(m) = \frac{n(m)}{|\nabla \cdot \mathrm{v}|}. \tag{7.4}$$

The cooling rate coefficient is computed as a four-parameter analytic fit with the form:

$$\frac{1}{L} = \frac{1}{L_0} + \frac{n(\mathrm{H_2})}{L_{\mathrm{LTE}}} + \frac{1}{L_0}\left(\frac{n(\mathrm{H_2})}{n_{1/2}}\right)^{\alpha}\left(1 - \frac{n_{1/2}L_0}{L_{\mathrm{LTE}}}\right). \tag{7.5}$$

Here L_0 represents the cooling in the low density limit, L_{LTE} is the cooling rate when the rotational level populations are in local thermodynamic equilibrium, and $n_{1/2}$ is the H_2 number density when $L = 0.5L_0$. L_0 is a function of temperature only while the other three parameters (L_{LTE}, $n_{1/2}$, and α) are functions of temperature and the effective column density per unit velocity as defined in Eqn. 7.4.

Rotational cooling for H_2O the cooling rate coefficient is tabulated between 10 K $< T <$ 4000 K and for column densities between 10 $< log_{10}(\widetilde{N}(\mathrm{H_2O})) <$ 19, where $\widetilde{N}(\mathrm{H_2O})$ in units of cm^{-2} per km s^{-1}. We assume a constant ortho-para ratio of 3:1 as Neufeld *et al.* (1995) who define cooling parameters for both states of H_2O. Similarly, the rotation cooling of CO is defined for temperatures between 10 K $< T <$ 2000 K and for column densities between $14.5 < log_{10}(\widetilde{N}(\mathrm{CO})) < 19$.

While there is nothing to prevent the gas in our simulations from going below 10 K, we introduce an artificial temperature floor at 10 K and turn off any radiative cooling at these temperatures. To properly model gas to temperatures below this value, one would be required to not only extend the results from Neufeld *et al.* (1993; 1995) but also include other physical processes, such as the CO freeze-out (*e.g.* Lee *et al.* 2004) or, if included in the chemical network, the decrease in dust temperature as the extinction increases (*e.g.* Goldsmith 2001).

For gas with temperatures above the tabulated values, we simply adopt cooling rates that correspond to the highest tabulated temperature. If the column density is within the tabulated range, then we linearly interpolate along column density to determine our cooling rate. Although at such high temperatures, it is expected that these coolants are quickly dissociated. With the floor on temperature, going below the tabulated cooling is of little concern.

A similar process is used when exceeding the tabulated column density. If we are denser than tabulated, use the highest values given for the cooling rate and, if possible, interpolate along temperature. If sparser than tabulated we use the lowest tabulated values. At very high densities, this procedure may overestimate the expected cooling. At lower densities however, the cooling rates naturally approach the optically thin limit and it is unlikely to introduce much error in our simulations.

Finally, in their calculation of the cooling functions, Neufeld *et al.* (1993; 1995) assume that only collisions between the target coolant and H_2 are important. However, as pointed out by G10, if the gas is not completely molecular then the collisions between atomic hydrogen or electrons are important. To account for this effect, we replace n_{H_2} in Eqn. 7.5 and in the total cooling rate, with an effective number density, n_{eff}. For CO rotational cooling

the effective number density is:

$$n_{\rm eff,CO,rot} = n_{\rm H_2} + \sqrt{2}\left(\frac{\sigma_{\rm H}}{\sigma_{\rm H_2}}\right) n_{\rm H} + \left(\frac{1.3 \times 10^{-8}\ {\rm cm^3\ s^{-1}}}{\sigma_{\rm H_2} v_e}\right) n_{\rm e}, \qquad (7.6)$$

where $n_{\rm H_2}$, $n_{\rm H}$, and $n_{\rm e}$ are the number densities of H_2, hydrogen, and electrons respectively, $\sigma_{\rm H} = 2.3\times\ 10^{-15}$ cm^2, $\sigma_{\rm H_2} = 3.3\times10^{-16}({\rm T}/1000{\rm K})^{-1/4}$ cm^2, and v_e=$1.03\times10^4\ \sqrt{T({\rm K})}$ cm s^{-1}. For H_2O rotational cooling the effective number density is

$$n_{\rm eff,H_2O,rot} = n_{\rm H_2} + 10 n_H + \left(\frac{k_e}{k_{\rm H_2}}\right) n_e, \qquad (7.7)$$

where k_e = dex[-8.020 + 15.740/$T^{1/6}$ - 47.137/$T^{1/3}$ + 76.648/$T^{1/2}$ - 60.191/$T^{2/3}$] and $k_{\rm H_2} = 7.4\times10^{-12}\ T^{1/2}$ cm^3 s^{-1}. These equations are taken from Meijerink & Spaans (2005) while the formula for k_e is taken from Faure, Gorfinkiel & Tennyson (2004).

Vibrational cooling from CO and H_2O , which is important at high temperatures and densities, is also presented in Neufeld *et al.* (1993). These authors provide a simpler two parameter fit of the form:

$$\frac{1}{L} = \frac{1}{L_0} + \frac{n_{\rm H_2}}{L_{LTE}}. \qquad (7.8)$$

Analytical functions are provided for L_0 for CO and H_2O as well as tabulated values for L_{LTE}. Vibrational cooling rates for both coolants are tabulated for temperatures 100 K $< T <$ 4,000 K and for column densities of $13 < log_{10}(\widetilde{N}) <$ 20. As above, $n_{\rm H_2}$ is replaced with updated values from Meijerink & Spaans (2005). For CO vibrational cooling, the effective number density is

$$n_{\rm eff,CO,vib} = n_{\rm H_2} + 50 n_{\rm H} + \left(\frac{L_{\rm CO,e}}{L_{\rm CO,0}}\right) n_{\rm e}, \qquad (7.9)$$

where

$$L_{\rm CO,e} = 1.03 \times 10^{-10} \left(\frac{T}{300}\right)^{0.938} \exp\left(\frac{-3080}{T}\right), \qquad (7.10)$$

and

$$L_{\rm CO,0} = 1.14 \times 10^{-14} {\rm exp}\left(\frac{-68.0}{T^{1/3}}\right) {\rm exp}\left(\frac{-3080}{T}\right). \quad (7.11)$$

Similarly for H_2O vibrational cooling, the effective number density is

$$n_{\rm eff,H_2O,vib} = n_{\rm H_2} + 10 n_{\rm H} + \left(\frac{L_{\rm H_2O,e}}{L_{\rm H_2O,0}}\right) n_{\rm e}, \quad (7.12)$$

where

$$L_{\rm H_2O,e} = 2.6 \times 10^{-6} T^{-1/2} {\rm exp}\left(\frac{-2325}{T}\right), \quad (7.13)$$

and

$$L_{\rm H_2O,0} = 0.64 \times 10^{-14} {\rm exp}\left(\frac{-47.5}{T^{1/3}}\right) {\rm exp}\left(\frac{-2325}{T}\right), \quad (7.14)$$

where in each of these equations, $n_{\rm H_2}$, $n_{\rm H}$, and $n_{\rm e}$ are the number densities of H_2, hydrogen, and electrons respectively and T is the gas temperature in K. For temperatures and effective column densities outside of the tabulated range, we calculate cooling rates as we do for the rotational case.

OH cooling

To model the cooling from OH we use the tabulated results from Omukai *et al.* (2010). These authors computed the OH cooling rate in the same manner as Neufeld *et al.* (1993; 1994) and presents values to fit Eqn. 7.5. The rate is valid in a temperature range between 30 K $< T <$ 600 K and for effective column densities of $10 < log_{10}(\widetilde{N}({\rm OH})) < 18$. For temperatures and densities outside this range, we calculate the appropriate cooling as above.

Heating Rates

To complete our treatment of the thermal evolution of the gas, we include the heating processes modeled in G10. In particular we include heating from the

photoelectric effect, H_2 UV pumping, and cosmic ray ionization. We also include a rate that takes into account the photoionization of hydrogen. When hydrogen is collisionally ionized, energy is taken from the gas to overcome the binding energy of the atom and lowering the internal energy of the gas. However, if the atom is photoionized, it does not alter the internal energy. We model this as a heating term with the form:

$$\Gamma_{\mathrm{H}^+} = \Delta Y_{\mathrm{H}^+} \varepsilon_{\mathrm{H}} \frac{k_{\mathrm{H}+\gamma\rightarrow\mathrm{H}^+}}{\Sigma_i^n k_i + k_{\mathrm{H}+\gamma\rightarrow\mathrm{H}^+}}, \tag{7.15}$$

where ΔY_{H^+} is the difference of $\mathrm{H}^+$is a time step, ε_{H} is the binding energy of hydrogen, $k_{\mathrm{H}+\gamma\rightarrow\mathrm{H}^+}$ is the rate at which hydrogen is photoionized, and $\Sigma_i^n k_i$ is the summation of all the collisional ionization rates that form H^+. Similar equations can be written for other atomic species, such as helium and carbon, however, hydrogen is the dominant heating term when compared to these other species.

Cooling Tests

Work continues on both the chemistry and cooling routines. While much of the groundwork has been done, we are looking into methods of testing and verifying both the chemistry network and cooling terms. Once these tests are complete, the large scale simulations will be conducted to study the effect of an infalling stream onto a dwarf galaxy.

Chapter 8

The Future

In the preceding chapters, I hoped to convince the reader that a great amount of work has been done to study the minihalo-galaxy outflow interactions. However, as any good scientist knows, research into one topic undoubtedly opens up new avenues of inquiry. This is certainly true for the work presented here. In the sections that follow, I will present a list of future research topics.

8.1 Effect of Cosmic Rays on Minihalos

At high-redshifts, the formation of coolants is very important. Of particular importance is molecular hydrogen, H_2 since it is the most abundant and very effective. In the absence of grains, the formation of H_2 requires a low level of ionization to provide a free electron catalyst. A variety of mechanisms exists that can create this level of ionization, for example, a background UV radiation field. But while UV photons can efficiently ionize hydrogen, they can just as easily dissociate any molecules formed. Cosmic rays, on the other hand, provide another avenue of ionizing particles that, under certain conditions, leads to appreciable molecule formation.

This opens up the possibility of cosmic ray induced molecule formation in high-redshift minihalos. The source of these early cosmic rays is unknown, however many sources have been suggested, such as decaying primordial black holes and very early supernova. To model this process, I will extend the primordial chemistry network to capture molecule formation as a function of cosmic-ray background, in addition to the UV background already implemented. This will allow me to study how the structure of a minihalo evolves in a wide variety of environments.

However, if the minihalo is cooled enough to collapse, it may have a dramatic impact on the study of the early Universe. For example, the resulting star formation will enrich the surviving minihalo gas as well as the intergalactic medium with metals. Furthermore, if a fairly large black hole is formed, it may explain observations of high-redshift ($z \sim 6$) quasars. Simulations of these objects usually require some source of "seed" black holes that merge together to form the $\sim 10^9$ $M_\odot$ black hole required. Cosmic ray induced molecule formation in minihalo could provide the source of these seeds (Li *et al.* 2007).

8.2 Star Formation and Stellar Feedback in Dense High-Redshift Clusters

Throughout this dissertation, I have assumed that the dense clumps of gas formed during the interaction between a galaxy outflow and primordial minihalo create an abundance of stars. In Chapter 4, I approximated the observable signatures of these stars based on estimated mass above a density threshold. While this was sufficient to show that these objects may be visible to future large telescopes, it does not take into account the hydrodynamical feedback from these stars. Therefore, a future research goal is to study the impact that these first stars had on the dense clump of gas.

There are several physical processes that need to modeled for this study: a chemical evolution model that tracks the formation and destruction of important coolants, a model for star formation, and a turbulence model to study the stellar feedback and subsequent mixing.

As has already been shown, the molecular makeup of the primordial gas is very important as molecules provides the primary coolants. Additionally, metals from the galaxy outflow and from stellar feedback, provide additional cooling paths. Therefore, a chemistry and cooling routine that accounts for formation and cooling from a variety of molecules is important. The low redshift

chemistry package developed for the study of NGC 5253 above makes the perfect choice to model this scenario.

Enrichment of the cluster gas will be studied as stellar feedback returns material back into its environment. Thus, a turbulence model is required to model the mixing between the stellar outflows and the surrounding gas. Fortunately, such a model has already been written and used with success in modeling the mixing between the galaxy outflow and the minihalo gas. This model evolves both the turbulent kinetic energy (K) and the eddy length scale (L), which in turn are used to calculate the turbulence viscosity (see Chapter 3 for details). The three primary fluid instabilities, Richtmyer-Meshkov, Kelvin-Helmholtz, and Rayleigh-Taylor, are well captured using this model and shows great promise in modeling the mixing between the gas and stellar outflows.

Finally, a model for stars and star formation will be developed. The FLASH hydrocode has the ability to create and evolve particles, which can be used to model stars (*e.g.* Federrath *et al.* 2010). The stars impact the surrounding medium in a couple of ways. Large stars will first ionize and destroy any molecules in the surrounding gas, and then enrich the gas through stellar winds and supernova. By tracking the ages of each of these 'stars' it is possible to realistically enrich the surrounding gas over the star's lifetime. Finally, metal enrichment from supernova will also be modeled. Therefore, much work will go into developing a module that incorporates all of these features.

There are two primary goals of this project. First is the study of star formation and feedback within dense, high-redshift clouds and their subsequent evolution. While they already have many of the expected properties of present-day halo globular clusters, much can be learned as they continue to evolve. Globular clusters are some of the oldest luminous objects in the

Universe. While the metallicity of a given cluster is fairly well homogenous, many recent observations have shown multiple main sequence populations, indicative of multiple rounds of star formation.

The first generation of stars will have a dramatic effect on the remaining cluster gas. Stellar winds and supernova will eject some of the gas from the cluster before it can be incorporated into the next generation of stars. The remaining gas will be enriched via the same mechanisms that will alter the make up of the second generation. I will study how much of the gas remains bound to the cluster and how enriched the remaining gas becomes.

The second goal will be to study the distribution of the surviving stars. Recent studies have focused on the fraction of stars from each bout of star formation, suggesting that most of the first generation of stars are either destroyed or removed from the cluster at early times (D'Ercole *et al.* 2008). A study of nearly 2000 stars in 19 Milky Way globular clusters showed that, on average, one-third of the current stellar population is from the first generation of stars (Carretta *et al.* 2009). These stars also showed distinct chemical abundances that require some degree of self-enrichment in these clusters (Caloi *et al.* 2011).

With the implementation of the above mentioned physics modules, I will study this initial burst of star formation and subsequent evolution of the remaining cluster gas. As the leftover gas is enriched from the first stars, I will study the makeup of further generations of stars.

8.3 Final Thoughts

In the preceding sections, I have laid out several avenues for future research. While these are interesting projects on their own, one may make the argument that the physics modules that have been developed are even more important.

With these tools in place a great many subjects and projects are available to study. These tools will continue to be improved upon and used to gain insights into many astrophysical events.

[1] Abel, T., Anninos, P., Zhang, Y., & Norman, M.L. 1997, New Astronomy, 2, 181

[2] Abel, T., Bryan, G. L., & Norman, M.L. 2002, Science, 295, 93

[3] Adelberger, K. L., Shapley, A. E., Steidel, C. C., Pettini, M., Erb, D. K., & Reddy, N. A. 2005, ApJ, 629, 636

[4] Adelberger, K. L., Steidel, C. C., Shapley, A. E., & Pettini, M. 2003, ApJ, 584, 45

[5] Ahn, K., Shapiro, P. R., Iliev, I.T., Mellema, G., & Pen, U. 2009, ApJ, 695, 1430

[6] Armandroff, T. C. 1989, AJ, 97, 375

[7] Ashman, K. M., & Bird, C. M. 1993, A.J, 106, 2281

[8] Bader, G., & Deuflhard, P 1983, Numer. Math. 41, 373

[9] Barkana R., & Loeb A. 1999, ApJ, 523, 54

[10] Beasley, M. A., Kawata, D., Pearce, F. R., Forbes, D. A., & Gibson, B. K. 2003, ApJ, 596, L187

[11] Bekki, K. 2010, MNRAS, in press (arXiv1011.5956)

[12] Bekki, K, 2011 MNRAS, 412, 2241

[13] Boley, A. C., Lake, G., Read, J., & Teyssier, R. 2009, ApJ, 706, L192

[14] Bond J. R., Szalay A. S., & Silk J. 1988, ApJ, 324, 627

[15] Bower R. G., Benson, A. J., Malbon, R., Helly, J. C., Frenk, C. S., Baugh, C. M., Cole, S., & Lacey, C. G. 2006, MNRAS, 370, 645

[16] Bower R.G., *et al.* 2006, MNRAS, 370, 645

[17] Brodie, J.P., & Strader, J. 2006, ARA&A, 44, 193

[18] Bromm, V., & Clarke, C. J. 2002, ApJ, 566, L1

[19] Bromm, V., Coppi, P.S., & Larson, R. 2002, ApJ, 564, 23

[20] Bromm, V., & Larson, R.B. 2004, ARA&A, 42, 79

[21] Brown, J. H., Burkert, A., & Truran, J. W. 1995, ApJ, 440, 666

[22] Brown, G.L., & Roshko, A. 1974, J. Fluid Mech, 64, 775

[23] Bruzual, G., & Charlot, S. 2003, MNRAS, 344, 1000

[24] Bullock, J.S., Kolatt, T.S., Sigad, Y., Somerville, R.S., Kravtsov, A.V., Klypin, A.A., Primack, J.R., & Dekel, A. 2001, MNRAS, 321, 559

[25] Bullock, J. S., Dekel, A., Kolatt, T.S., Kravtsov, A.V., Klypin, A.A., Porciani, C., & Primack, J. R. 2001, ApJ, 555, 240

[26] Caloi, V., & D'Antona, F. 2011, MNRAS, 417, 228

[27] Carraro, C., Ng, Y.K., & Portinari, L. 1998, MNRAS, 296, 1045

[28] Carretta, E., *et al.* . 2009, A&A, 505, 117

[29] Cen, R. 2001, ApJ, 560, 592

[30] Chiravalle, V. P. 2006, Laser and Particle Beams, 24, 381

[31] Chung, A., Yun, M.S., Naraynana, G., Heyer, M., & Erickson, N.R. 2011, ApJ, 732, L15

[32] Ciardi, B., & Ferrara, A. 2005, Space Sci. Rev., 116, 625

[33] Ciardi, B., Ferrara, A., & Abel, T. 2000, ApJ, 533, 594

[34] Cole, S., Lacey, C. G., Baugh, C. M., & Frenk, C. S. 2000, MNRAS, 319, 168

[35] Colella, P., & Glaz, H.M. 1985, JCoPh, 59, 264

[36] Colella, P., & Woodward P. 1984, JCoPh, 54, 174

[37] Conroy, C., Leob, A., & Spergel, D. 2011, ApJ, 741, 72

[38] Cowie, L., Songaila, A., & Hu E. 1996, ApJ, 112, 3

[39] Cumming, R. J., Fathi, K., Östlin, G., Marquart, T., Màquez, I., Masegosa, J., Bergvall, N., & Amram, P. 2008, A&A, 479, 725

[40] Dalgarno, A., & McCray, R. A. 1972, ARA&A, 10, 375

[41] Dauphole, B., Geffert, M., Colin, J., Ducourant, C., Odenkirchen, M., & Tucholke, H.J. 1996, A&A, 313, 119

[42] Deharveng, L., Peña, M., Caplan, J., & Costero, R. 2000, MNRAS, 311, 329

[43] D'Ercole, A., Vesperini, E., D'Antona, F., McMillan, S. L. W., & Recchi, S. 2008, MNRAS, 391, 825

[44] Dimonte, G., & Tipton, R. 2006, Phys of Fluids, 18, 085101 (DT06)

[45] Draine, B.T. 1978, ApJS, 36, 595

[46] Eisenstein, D. J., & Hu, W. 1999, ApJ, 511, 5

[47] Eke, V., Navarro, J., & Frenk, C. 1998, ApJ, 503, 569

[48] Elmegreen, B. G., 2010, in IAU Symp. 226, Star Clusters Basic Galactic Building Blocks Throughout Time and Space, ed. R. de Grijs & J. Lepine, Cambridge, 3

[49] Elmegreen, B. G., & Efremov, Y. N. 1997, ApJ, 480, 235

[50] Fall, S.M., & Rees, M.J. 1985, ApJ, 298, 18

[51] Faure, A., Gorfinkiel, J. D., & Tennyson, J. 2004, MNRAS, 347, 323

[52] Federralth, C., Banerjee, R., Clark, P.C., & Klessen, R. S. 2010, ApJ, 713, 269

[53] Ferland, G.J., Korista, K.T., Verner, D.A., Ferguson, J.W., Kingdon, J.B., & Verner, E.M. 1998, PASP, 110, 761

[54] Ferrara, A. 1998, ApJ, 499, L17

[55] Firmani, C., & Avila-Reese, V. 2010, ApJ, 723, 755

[56] Fragile, C.P., Murray, S.D., & Anninos, P. 2004, ApJ, 604, 74

[57] Franx, M., Illingworth, G. D., Kelson, D. D., van Dokkum, P. G., & Tran, K.-V. 1997, ApJ, 486, L75

[58] Friel, E.D., & Boesgaard, A.M. 1992, ApJ, 387, 170

[59] Fryxell, B., Müller, E., & Arnett, D. 1990, in Proc. 5th Workshop on Nuclear Astrophys. ed. W. Hillebrandt & E. Müller (Garching: MPI für Astrophysik), 100

[60] Fryxell, B., Olson, K., Ricker, P., Timmes, F.X., Zingale, M., Lamb, D.Q., MacNeice, P., Rosner, R., Truran, J., Tufo, H. 2000, ApJS, 131, 273

[61] Fryxell, B., Müller, E., & Arnett. B. 1989, nuas.conf, 100

[62] Fujita, A., Martin, C. L., Mac Low, M.-M., & Abel, T. 2003, ApJ, 599, 50

[63] Galli, D., & Palla, F. 1998, A&A, 335, 403

[64] Gardner, J. P. *et al.* 2006, Space Sci. Rev., 123, 485

[65] Giant Magellan Telescope Organization. 2006, Giant Magellan Telescope Science Case, *http://www.gmto.org/sciencecase*

[66] Gibson, B. K *et al.* . 2000, ApJ, 529, 723

[67] Glasner, A., Livne, E., & Meerson, B. 1997, Phys. Rev. Lett., 78, 2112

[68] Glover, S.C.O., & Abel, T. 2008, MNRAS, 388, 4 (GA08)

[69] Glover, S. C. O., & Abel, T. 2008, MNRAS, 388, 1627

[70] Glover, S.C.O. 2009, private communication (G09)

[71] Glover, S.C.O., Savin, D.W. 2009, MNRAS, 393, 991

[72] Glover, S.C.O., Federrath, C., Mac Low, M. M., & Klessen, R. S. 2010, MNRAS, 404, 2

[73] Gnedin, O. Y., & Ostriker, J. P. 1997, ApJ, 474, 223

[74] Goldsmith, P. F. 2001, ApJ, 557, 736

[75] Gonzalo Diáz, C., Ryan-Weber, E. V., Cooke, J., Pettini, M., & Madau, P. 2011, MNRAS, 418, 820

[76] Gorjian, V. 1996, ApJ, 112, 5

[77] Gorjian, V., Turner, J. L., & Beck, S. C. 2001, ApJ, 554, L29

[78] Gray, W. J., & Scannapieco, E. 2010, ApJ, 718, 417

[79] Gray, W. J., & Scannapieco, E. 2011, ApJ, 733, 88

[80] Gray, W. J., & Scannapieco, E. 2011, ApJ, 742, 100

[81] Griffen, B. F., Drinkwater, M. J., Thomas, P.A., Helly, J.C., & Pimbblet, K. A. 2010, MNRAS, 405, 375

[82] Grillmair, C.J., Freeman, K.C., Irwin, M., & Quinn, P.J. 1995, AJ, 109, 2553

[83] Habing, H. J. 1968, Bull. Astr. Inst. Netherlands, 19, 421

[84] Haiman, Z., Able, T., & Madau, P. 2001, ApJ, 551, 599

[85] Haiman, Z., Abel, T., & Rees, M. J. 2000, ApJ, 534, 11

[86] Haiman, Z., Rees, M., & Loeb, A. 1997, ApJ, 476, 458 (erratum 484, 985)

[87] Hammer, F., Kaper, L., & Dalton, G. 2010, Msngr, 140, 36

[88] Heckman, T. M., Lehnert, M. D., Strickland, D. K., & Armus, L. 2000, ApJ, 129, 493

[89] Heger, A., & Woosley, S.E. 2002, ApJ, 567, 532

[90] Henry, R.B.C., & Worthey, G. 1999, PASP, 111, 919

[91] Iliev, I. T., Shapiro, P. R., & Raga, A. C. 2005, MNRAS, 361, 405

[92] Irwin, M., & Hatzidimitriou, D. 1993, ASPC, 48, 322

[93] James, B. L., Tsamis, Y. G., & Barlow, M. J. 2010, MNRAS, 401, 759

[94] Jordán, A. *et al.* 2005, ApJ, 634, 1002

[95] Kang, H., Shapiro, P.R., Fall, M., & Rees, M.J. 1990, ApJ, 363, 488

[96] Kaps, P., & Rentrop, P. 1979, Numer. Math., 33, 55

[97] Kauffmann, G., White, S. D. M., & Guiderdoni, B. 1993, MNRAS, 264, 201

[98] Keller, S. T., Mackey, D., & Da Costa, G. S. 2011, arXiv, 1109:4414v1

[99] Klamer, I. J., Ekers, R. D., Sadler, E. M., & Hunstead, R. W. 2004, ApJ, 612:L97-L100

[100] Klein, R., McKee, C.F., & Colella, P. 1994, ApJ, 420, 213

[101] Kravtsov, A. V., & Gnedin, O. Y. 2005, ApJ, 623, 650

[102] Lacey, C., & Cole, S. 1993, MNRAS, 262, 627

[103] Larsen, S. S., Brodie, J. P., Huchra, J. P., Forbes, D. A., & Grillmair, C. J. 2001, AJ, 121, 2974

[104] Lee, J.E., Bergin, E. A., & Evans, N. J. 2004, ApJ, 617, 360

[105] Lehnert, M. D., & Heckman, T. M. 1996, ApJ, 462, 651

[106] Lehnert, M. D., Heckman, T. M., & Weaver, K. A. 1999, ApJ, 523, 575

[107] Leitherer, L., *et al.* 1999, ApJS, 123, 3

[108] Le Teuff, Y.H., Millar, T. J., & Markwick, A.J. 2010, A&AS, 146, 157

[109] Li, Y., & Burstein, D. 2003, ApJ, 598, L103

[110] Li, Y., Hernquist, L., Robertson, B., Cox, T. J., Hopkins, P. F., Springel, V., Gao, L., Di Matteo, T., *et al.* 2007, ApJ, 665, 187

[111] Lipovka, A., Nunez-Lopez, R., & Avila-Reese, V. 2005, MNRAS, 361, 850

[112] Mackey, A.D., & Gilmore, G. F. 2004, MNRAS, 355, 504

[113] Mac Low, M., & Shull, J.M. 1986, ApJ, 302, 585

[114] McCarthy, P. 2008, Presentation made to the Astronomical Society of Australia

[115] Madau, P., Ferrara, A., & Rees, M. 2001, ApJ, 555, 92

[116] Marcolini, A., Gibson, B. K., Karakas, A. I., & Sánchez-Blázquez, P. 2009, MNRAS, 395, 719

[117] Martin, C. L. 1998, ApJ, 506, 222

[118] Martin, C. L. 1999, ApJ, 513, 156

[119] Martin, C. L. 2006, ApJ, 647, 222

[120] Meier, D. S., Turner, J. L., & Beck, S. C. 2002, ApJ, 124, 877

[121] Meijerink, R., & Spaans, M. 2005, A&A, 436, 397

[122] Meurer, G. R., Heckman, T. M., Leitherer, C., Kinney, A., Robert, C., & Garnett, D. R. 1995, ApJ, 110, 6

[123] Moore, B. 1995, ApJ, 461, L13

[124] Mori, M., Ferrara, A., & Madau, P. 2002, ApJ, 571, 40

[125] Muratov, A. L., & Gnedin, O. Y. 2010, ApJ, 718, 1266

[126] Nakasato, N., Mori, M., & Nomoto, K. 2000, ApJ, 535, 776

[127] Navarro, J.F., Frenk, C.S, & White, S.D.M. 1997, ApJ, 490, 493

[128] Neistein, E., van den Bosch, F. C., & Dekel, A. 2006, MNRAS, 372, 933

[129] Neufeld, D. A., Kaufman, M. J. 1993, ApJ, 418, 263

[130] Neufeld, D. A., Lepp, S., & Melnick, G. J. 1995, ApJS, 100, 132

[131] Olszewski, E.W., Schommer, R.A., Suntzeff, N.B., & Harris, H.C. 1991, ApJ, 101, 515

[132] Omukai, K., Hosokawa, T., & Yoshida, N. 2010, ApJ, 722, 1793

[133] O'Shea, B.W., & Norman, M.L. 2007, ApJ, 654, 66

[134] Osterbrock, D.G., Astrophysics of Gaseous Nebulae and Active Galactic Nuclei. University Science Books. 1989.

[135] Ostriker, J. P., Spitzer, L., & Chevalier, R. A. 1972, ApJ, 176, L51

[136] Palla, F., Salpeter, E.E., & Stahler, S.W. 1983, ApJ, 271, 632

[137] Palla, F., & Zinnecker, H. 1988, in IAU Symp. 126, The Harlow Shapley Symposium on Globular Cluster Systems in Galaxies, ed. J. E. Grindlay & A. G. D. Philip (Doredrecht: Reidel), 697

[138] Pan, L., & Scalo, J. 2007, ApJ, 654, L29

[139] Pan, L., & Scannapieco, E. 2010, ApJ, 721, 1765

[140] Papamoschou, D., & Roshko, A. 1988, J Fluid Mech, 197, 453

[141] Pavlovski, G., Smith, M. D., & Mac Low, M. M. 2002, MNRAS, 2002, 337, 477

[142] Peng, W., & Weisheit, J. C. 1991, PASP, 103, 891

[143] Pettini, M., Kellogg, M., Steidel, C. C., Dickinson, M., Adelberger, K. L., & Giavalisco, M. 1998, ApJ, 508, 539

[144] Pettini, M., *et al.* . 2001, ApJ, 554, 981

[145] Piotto, G., *et al.* . 2007, ApJ, 661, 53

[146] Prieto, J. P., Infante, L., & Jimenez, R. 2009, arXiv:0809.276v2

[147] Press, W. H., & Schechter, P. 1974, ApJ, 187, 425

[148] Recchi, S., & Danziger, I. J. 2005, A&A, 436, 145

[149] Ricker, P. M. 2008, ApJS, 176, 293

[150] Rupke, D. S., Veilleux, S, & Sanders, D. B. 2005, ApJS,160,115

[151] Reddy, B.E., Tomkin, J., Lambert, D.L., & Prieto C.A. 2003, MNRAS, 340, 304

[152] Scalo, J., & Elmegreen, B.G. 2004, ARAA, 42, 275

[153] Scannapieco, E ., & Brüggen, M. 2008, ApJ, 686, 927 (SB08)

[154] Scannapieco, E ., & Brüggen, M. 2010, MNRAS, 405, 1634

[155] Scannapieco, E., Ferrara, A., & Madau, P. 2002, ApJ, 574, 590

[156] Scannapieco, E., Schneider, R., & Ferrara, A. 2003, ApJ, 589, 35

[157] Scannapieco, E., Weisheit, J., & Harlow, F. 2004, ApJ, 615, 29

[158] Schaerer, D. 2002, A&A, 382, 28

[159] Semenov, D., *et al.* . 2010, A&A, 522, A42

[160] Shapiro, K. L., Genzel, R., & Förster Schreiber, N. M. 2010, MNRAS, 403, L36

[161] Shapiro, P. R., Iliev, I. T., & Raga, A. C. 2004, MNRAS, 348, 753

[162] Shapiro, P. R., Iliev, I. T., Alvarex, M. A., & Scannapieco, E. 2006, ApJ, 648, 992

[163] Shapiro, P.R., & Kang, H. 1987, ApJ, 318, 32

[164] Shapiro, P. R., Raga A. C., & Mellema G. 1997, in Petitjean P., Charlot S., eds, Proc. 13th IAP Astrophys. Colloq., Structure and Evolution of the Inter- galactic Medium from QSO Absorption Line Systems. Inst. Astrophys. Paris, Paris, p. 41

[165] Shapiro, P. R., Raga A. C., & Mellema G. 1998, Mem. Soc. Astron. Ital., 69, 463

[166] Slessor, M.D., Zhuang, M., & Dimotakis, P.E. 2000, J. Fluid Mech, 414, 35

[167] Semenov, D., Hersant, F., Wakelam, V., Dutrey, A., Chapillon, E., *et al.* . 2010, A&A, 522, 42

[168] Smith, B., Sigurdsson, S., & Abel, A. 2008, MNRAS, 385, 1443

[169] Smith, G. H. 2010, PASP, 122, 896

[170] Sokasian, A., Yoshida, N., Abel, T., Hernquist, L., & Springel, V. 2004, MNRAS, 350, 47

[171] Soteriou M.C., & Ghoniem, A.F. 1995, Phys. Fluids, 7, 2036

[172] Spergel, D. N. *et al.* 2007, ApJ, 170, 377

[173] Spitzer, L., & Thuan, T. X. 1972, ApJ, 175, 31

[174] Stacy, A., Greif, T. H., & Bromm, V. 2010, MNRAS, 403, 45

[175] Strader, J., Brodie, J. P., Cenarro, A. J., Beasley, M. A., & Forbes, D. A. 2005, AJ, 130, 1315

[176] Stiavelli, M., *et al.* . 2008, "JWST Primer", Version 2.0, (Baltimore: STScI)

[177] Suntzeff, N., Mateo, M., Terndrup, D. M., Olszweski, E. W., Geisler, D., & Weller, W. 1993, ApJ, 418, 208

[178] Timmes, F.X. 1999, ApJ, 124, 241

[179] Thacker R. J., Scannapieco E., & Davis M. 2002, ApJ, 202, 581

[180] Tolstoy, E., Hill, V., & Tosi, M. 2009, ARAA, 47, 371

[181] Thuan, T.X., Izotov, Y.I., & Lipovetsky, V.A. 1995, ApJ, 445, 108

[182] Turner, J. L., & Beck, S. C. 2004, ApJ, 602, L85

[183] Turner, J. L., Beck, S. C., & Ho, P.T. 2000, ApJ, 532, L109

[184] Turk, M. J., Abel, T., & O'Shea, B. 2009, Science, 325, 601

[185] Twarog, B.A., Ashman, K.M., & Anthony-Twarog, B.J. 1997, ApJ, 114, 2556

[186] Uehara, H. & Inutsuka, Shu-ichiro 2000, ApJ, 531, L91

[187] Vanzi, L., Combes, F., Rubio, M., & Kunth, D. 2009, A&A, 496, 667

[188] van Breugel, W., Filippenko, A.V., Heckman, T.,Miley, G. 1985, ApJ, 293, 83

[189] Veilleux, S., Cecil, G., & Bland-Hawthorn, J. 2005, ARA&A, 43, 769

[190] Weirsma, R. P. C., Schaye, J., & Smith, B.D. 2009, MNRAS, 393, 9

[191] Weirsma, R., Schaye, J., & Smith, B. 2008, MNRAS, 393, 99

[192] Whalen, D., O'Shea, B.W., Smidt, J., & Norman, M.L. 2008a, ApJ, 679, 925

[193] Whalen, D., van Veelen, B., O'Shea, B.W., & Norman, M.L. 2008b, ApJ, 682, 49

[194] White, S. D. M., & Frenk, C. S. 1991, ApJ, 379, 52

[195] White, S. D. M., & Rees, M. J. 1978, MNRAS, 183, 341

[196] Wiita, Paul J. 2004, Ap&SS, 293, 235

[197] Wilman, R. J., Gerssen, J., Bower, R. G., Morris, S. L., Bacon, R., de Zeeum, P. T., Davies, R. L. 2005, Nature, 436, 227

[198] Woodall, J., Agúndez., M., Markwick-Kemper, A.J., & Millar, T. J. 2007, A&A, 466, 3

[199] Woosley, S.E., & Weaver, T.A. 1995, ApJS, 101, 181

[200] Wright, N. 2006, PASP, 118, 1711

[201] Wright, S., & Barton, B. 2009, "IRIS Sensitivities, Simulations and Astrometry Update", TMT.INS.PRE.09.037

[202] Xie, T., Allen, M., & Langer, W.D. 1995, ApJ, 440, 674

[203] Zepf, S. E., & Ashman, K. M. 1993, MNRAS, 264, 611

[204] Zinn, R. 1985, ApJ, 293, 424